# Study and selection of scintillating crystals for the bolometric search for neutrinoless double beta decay

Anastasiia Zolotarova

NNT : 2018SACLS293

# Study and selection of scintillating crystals for the bolometric search for neutrinoless double beta decay

Thèse de doctorat de l'Université Paris-Saclay
préparée à l'Université Paris-Sud

École doctorale n° n°576 : particules hadrons énergie et noyau : instrumentation, image, cosmos et simulation (Pheniics)
Spécialité de doctorat: physique de particules

Thèse présentée et soutenue à Saint-Aubin, 24/09/2018, par

**Anastasiia Zolotarova**

Composition du Jury :

| | |
|---|---|
| Jules Gascon<br>Professeur, IPNL | Président |
| Alessandra Tonazzo<br>Professeure, Université Paris Diderot (APC) | Rapporteur |
| Aldo Ianni<br>Chercheur, INFN (LNGS) | Rapporteur |
| Fabio Bellini<br>Professeur associe, Sapienza Università di Roma (INFN) | Examinateur |
| Volodymyr Tretyak<br>Professeur associe, KINR (LPD) | Examinateur |
| Stefanos Marnieros<br>Chargé de recherche, CNRS (CSNSM) | Examinateur |
| Claudia Nones<br>Chercheur, CEA-Saclay (DPhP) | Directeur de thèse |

Thèse de doctorat

université PARIS-SACLAY | ÉCOLE DOCTORALE PHENIICS

**Titre :** Etude et sélection de cristaux scintillants pour la recherche de la double désintégration bêta sans neutrino avec des bolomètres scintillants

**Mots clés :** physique de neutrino, double désintégration beta, bolomètres cryogénie

**Résumé :** L'observation de la désintégration double bêta sans émission de neutrino (0ν2β) fournirait des informations essentielles sur la nature du neutrino et son échelle de masse absolue. Ce processus consiste en la transformation simultanée de deux protons en deux neutrons avec l'émission de deux électrons et aucun neutrino. Cette transition n'est possible que si les neutrinos sont égaux aux antineutrinos (nature Majorana du neutrino). Les recherches pour une désintégration à ce point rare représentent un défi technique complexe, car les expériences de prochaine génération visent des sensibilités de l'ordre de $10^{27}$-$10^{28}$ ans afin d'avoir un potentiel de découverte élevé. Cette thèse est focalisée sur les projets LUMINEU et CUPID-Mo, développant la technique des bolomètres scintillants pour la recherche de désintégration 0ν2β avec le radio-isotope $^{100}$Mo. Les bolomètres sont des détecteurs cryogéniques mesurant l'énergie des particules déposées via un changement de température dans l'absorbeur. Si des cristaux scintillants sont utilisés comme absorbeurs, les signaux lumineux peuvent être enregistrés avec un bolomètre auxiliaire, sensible à l'énergie totale déposée par les photons de scintillation. Une telle configuration permet de séparer les particules α des γ/β, en rejetant le fond le plus difficile. La technologie des bolomètres scintillants est décrite en détail comme une option pour une future expérience cryogénique à l'échelle d'une tonne, appelée CUPID, qui peut couvrir complètement la région de masses de neutrinos dans la hiérarchie inversée.

**Title :**Study and selection of scintillating crystals for the bolometric search for neutrinoless double beta decay

**Keywords :** neutrino physics, neutrinoless double beta decay, bolometers, cryogenics

**Abstract :** Neutrinoless double beta (0ν2β) decay is a process of great interest for neutrino physics: its observation would provide essential information on neutrino nature and its absolute mass scale. This process consists of the simultaneous transformation of two protons into two neutrons with the emission of two electrons and no neutrino, implying the violation of the total lepton number. Such transition is possible only if neutrinos are equal to antineutrinos (Majorana particles). The searches for such a rare decay are becoming a complicated technical challenge, as next generation of 0ν2β experiments aim at sensitivities of the order of half-life at $10^{27}$-$10^{28}$ yr. This thesis is focused on LUMINEU and CUPID-Mo projects, developing the scintillating bolometers technique for 0ν2β decay search with $^{100}$Mo with $Li_2MoO_4$ crystals. Bolometers are cryogenic detectors measuring the deposited particle energy as a change of temperature in the absorber. The use of scintillating crystals allows to perform discrimination of α particles from γ/β ones due to different light output of these two particle types, rejecting the most challenging background. The scintillating bolometers technology is described in details as an option for a future ton-scale cryogenic experiment, named CUPID, which can completely cover the inverted hierarchy region of neutrino masses.

**Université Paris-Saclay**
Espace Technologique / Immeuble Discovery
Route de l'Orme aux Merisiers RD 128 / 91190 Saint-Aubin, France

"*If we knew what we were doing, it wouldn't be called research.*"

Albert Einstein

PARIS-SACLAY

# *Abstract*

Paris-Saclay
Particules, Hadrons, Energie et Noyau: Instrumentation, Imagerie, Cosmos et Simulation (PHENIICS)

Doctor of Philosophy

**Study and selection of scintillating crystals for the bolometric search for neutrinoless double beta decay**

by Anastasiia Zolotarova

The neutrino, an extremely elusive particle, raises a lot of questions in modern particle physics. Neutrino oscillations observations have proved that neutrino is massive, but most of its properties are not studied yet. The neutrinoless double beta ($0\nu2\beta$) decay observation would provide essential information on neutrino nature and its absolute mass scale. This process consists of the simultaneous transformation of two protons into two neutrons with the emission of two electrons and no neutrino, implying the violation of the total lepton number. Such transition is possible only if neutrinos are equal to antineutrinos (Majorana nature of neutrino). Experimental limits on the $0\nu2\beta$ half-life are $T_{1/2}>10^{24}$-$10^{26}$ yr and the searches for such a rare decay are becoming a complicated technical challenge, as next generation experiments aim at sensitivities of the order of $10^{27}$-$10^{28}$ yr in order to have a high discovery potential. This thesis is focused on LUMINEU and CUPID-Mo projects, developing the scintillating bolometers technique for $0\nu2\beta$ decay search with $^{100}$Mo. Bolometers are cryogenic detectors measuring the deposited particle energy as a change of temperature in the absorber. If scintillating crystals are used as absorbers, light signals can be registered with an auxiliary bolometer, sensitive to the total energy deposited by the scintillation photons. Such configuration allows to perform discrimination of $\alpha$ particles from $\gamma/\beta$ ones, rejecting the most challenging background. The scintillating bolometers technology is described in details as an option for a future ton-scale cryogenic experiment, named CUPID, which can completely cover the inverted hierarchy region of neutrino masses. Detectors based on $Li_2MoO_4$ and $ZnMoO_4$ crystals coupled to germanium light detectors were investigated in the framework of LUMINEU R&D. The direct comparison of the two compounds, described in this thesis, has allowed us to choose the crystal type for the next phase of the experiment, which will investigate a much bigger amount of $^{100}$Mo. CUPID-Mo is a demonstrator with 20 enriched $Li_2{}^{100}MoO_4$ crystals (2.34 kg of $^{100}$Mo), aiming to confirm the reproducibility and performance of scintillating bolometers for

neutrinoless double beta decay searches with $^{100}$Mo. The preparation of the detectors, assembly and installation in the cryogenic set-up is deeply described being a crucial part of the presented activity. Data-taking has already started with the aim to measure for at least six month with a background level of $\sim 10^{-3}$ counts/keV/kg/yr. This experiment will establish the best limit on neutrinoless double beta decay of $^{100}$Mo and the most precise measurement of the two neutrino double beta decay mode, which is allowed by the Standard Model. Other CUPID R&D, like CUPID-0 demonstrator, are also described in this manuscript. CUPID-0 is searching for neutrinoless double beta decay of $^{82}$Se with 26 Zn$^{82}$Se scintillating bolometers (5.28 kg of $^{82}$Se). Data taking is ongoing and the demonstrator has reached the remarkable background level at $3.6^{+1.9}_{-1.4} \times 10^{-3}$ counts/keV/kg/yr. In conclusions these demonstrator experiments are providing promising technology for double beta decay searches and can be considered as viable options for the future ton-scale CUPID experiment.

**Etude et sélection de cristaux scintillants pour la recherche de la double désintégration bêta sans neutrino avec des bolométres scintillants**

Cette thèse a été réalisée dans le contexte de la physique des neutrinos. Le premier chapitre de ce manuscrit contient une brève revue historique des recherches en physique des neutrinos et un résumé de leurs propriétés connues à ce jour. Le phénomène d'oscillations de neutrinos montre qu'une extension du Modèle Standard (les neutrinos ne sont pas massifs dans le Modèle Standard) ou l'élaboration d'une nouvelle théorie complète des interactions fondamentales est nécessaire. La détermination des masses des neutrinos est une question phare de la physique moderne. Il est encore plus important de confirmer leur nature: si le neutrino est une particule de Majorana (c'est-à-dire sa propre antiparticule), cela violerait la conservation du nombre leptonique; et, pour expliquer la faible masse des neutrinos, le mécanisme de see-saw, contenant les termes de masse de Majorana, peut être introduit comme une extension du Modèle Standard. Les propriétés des neutrinos pourraient donner des indices sur les caractéristiques essentielles de la matière, telles que l'asymétrie matière-antimatière, ou la matière noire, conduisant ainsi à une compréhension complète des mécanismes de notre Univers. La mesure des masses des neutrinos est un objectif ambitieux, pour lequel plusieurs méthodes indirectes ont été développées. L'un des moyens les plus prometteurs pour déterminer l'échelle de masse absolue des neutrinos est la recherche de la double désintégration bêta sans émission de neutrino ($0\nu2\beta$). La recherche de la désintégration $0\nu2\beta$ est le sujet principal de cette thèse.

La théorie correspondante et les approches expérimentales utilisées pour la recherche de cette transition sont décrites dans le chapitre 2. Son observation fournirait des informations essentielles sur la nature du neutrino et son échelle de masse absolue. Ce processus consiste en la transformation simultanée de deux protons en deux neutrons avec émission de deux électrons et pas de neutrino, impliquant la violation du nombre leptonique total. Son observation confirmerait la nature des neutrinos en tant que particules de Majorana (la désintégration $0\nu2\beta$ ne peut se produire que si les neutrinos sont égaux aux antineutrinos). Théoriquement, cette désintégration est autorisée pour 35 noyaux, mais seuls quelques-uns conviennent aux recherches expérimentales de désintégration $0\nu2\beta$. Les limites actuelles sur le temps de demi-vie de cette transition sont de $T_{1/2}>10^{24}$-$10^{26}$ ans et les recherches d'une désintégration à ce point rare représentent un défi technique complexe. Les futures expériences de nouvelle génération visent des sensibilités de l'ordre de $10^{27}$-$10^{28}$ ans afin d'avoir un fort potentiel de découverte. Pour atteindre un tel niveau, une rupture technologique sur la méthode de détection utilisée actuellement est nécessaire. Une attention particulière est accordée à la réduction du bruit de fond dans la région d'intérêt.

La technologie des bolomètres à scintillation est décrite au chapitre

3. Les bolomètres sont des détecteurs cryogéniques dans lesquels l'énergie déposée par les particules peut être mesurée comme un changement de température dans l'absorbeur, grâce à l'utilisation de capteurs thermiques spéciaux capables de convertir les fluctuations de température en signal électrique. Les capteurs utilisés dans ce travail sont des thermistances en germanium: NTD (Neutron Transmutation Doped). Si des cristaux scintillants sont utilisés comme absorbeurs, les signaux lumineux peuvent être enregistrés par un bolomètre auxiliaire, sensible à l'énergie totale déposée par les photons issus de la scintillation. Une telle configuration permet la discrimination entre les particules $\alpha$ et les $\gamma/\beta$, permettant donc de rejeter le bruit de fond le plus problématique. Selon l'absorbeur choisi, ces détecteurs peuvent être utilisés dans diverses applications: recherche de matière noire, désintégration $0\nu2\beta$, diffusion des neutrinos, détection de neutrons. Les bolomètres, utilisés dans des conditions appropriées, peuvent atteindre une résolution en énergie de 0.1% (largeur à mi-hauteur). En choisissant l'absorbeur et le capteur thermique adéquats, différentes régions d'énergie peuvent être explorées.

Les recherches de désintégration $0\nu2\beta$ avec des bolomètres nécessitent des installations cryogéniques spécifiques, capables de fonctionner avec de grandes masses de détecteurs. L'utilisation de réfrigérateurs à dilution (DR) permet de refroidir les échantillons et de maintenir des conditions stables à une température comprise entre 10 et 20 mK. Ces installations sont complexes et nécessitent une bonne connaissance de la cryogénie et des systèmes de manipulation du vide. Plusieurs cryostats, utilisés pour les mesures effectuées dans ce travail, sont décrits dans l'annexe A.

Le $^{100}$Mo est l'un des isotopes les plus prometteurs pour les recherches de désintégration $0\nu2\beta$. Il présente une énergie de transition élevée (3034 keV), supérieure à l'énergie de la radioactivité $\gamma$ naturelle (2615 keV). Une telle énergie permet d'obtenir un très faible bruit de fond dans la région d'intérêt. Il est possible d'enrichir en grandes quantités cet isotope (par centrifugation gazeuse). De plus les prédictions théoriques quant aux caractéristiques du $^{100}$Mo sont favorables: sa demi-vie de désintégration $0\nu2\beta$ devrait être l'une des plus basses parmi tous les isotopes autorisant la désintégration $0\nu2\beta$ étudiés expérimentalement. Le chapitre 4 est consacré à l'étude des bolomètres scintillants à base de cristaux de $Li_2MoO_4$ et de $ZnMoO_4$ couplés à des détecteurs de lumière au germanium dans le cadre du projet de R&D LUMINEU. Une comparaison directe de ces deux composés a été réalisée lors d'une mesure en laboratoire souterrain. Cette mesure nous a permis de choisir le $Li_2MoO_4$ pour la prochaine phase de l'expérience, qui permettra d'étudier une quantité beaucoup plus grande de $^{100}$Mo. Pour confirmer la reproductibilité des performances élevées des détecteurs, une mesure en laboratoire souterrain avec quatre cristaux de $Li_2{}^{100}MoO_4$ a été réalisée. Les bolomètres scintillants composé de $Li_2{}^{1}00MoO_4$ ont montré une résolution en énergie de 5 à 6 keV, le rejet

à au moins $9\sigma$ des particules $\alpha$ au voisinage de la décroissance $0\nu2\beta$ du $^{100}$Mo (3034 keV) et moins de 10 $\mu$Bq/kg d'activité du $^{228}$Th et du $^{226}$Ra. Avec une exposition de 0.04 kg×an, acquise dans cette série, la demi-vie de décroissance $2\nu2\beta$ du $^{100}$Mo a été mesurée avec une précision, la meilleure à ce jour, de $T_{1/2} = 6.92 \pm 0.06$ (stat.) $\pm$ 0.36 (syst.) $\times 10^{18}$ ans. Avec un faible temps d'exposition de 0.11 kg×an, on a pu fixer une limite sur la demi-vie de désintégration du Mo en $0\nu2\beta$ : $T_{1/2} \geq 0.7 \times 10^{23}$ ans. La R&D LUMINEU s'est achevée avec succès grâce aux résultats de la technologie des bolomètres scintillants. Le protocole de croissance des cristaux a été développé et a eu pour résultat des cristaux radio-purs de haute qualité, reproductibles à l'échelle industrielle. Une procédure de production, d'assemblage et de tests des détecteurs de lumière au germanium à haute performance a été également mise en place. Le protocole de production de cristaux enrichis en $^{100}$Mo de haute pureté (enrichissement à 96 %) a été établi. Quelques cristaux de $Li_2{}^{100}MoO_4$ ont été produits et testés en tant que bolomètres, montrant des performances et une reproductibilité excellentes.

L'expérience CUPID (CUORE Upgrade with Particle Identification) est une expérience proposée à l'échelle de la tonne avec des bolomètres cryogéniques, visant à atteindre une sensibilité qui permettrait d'exploiter complètement la région de la hiérarchie de masse inversée des neutrinos. CUPID sera basé sur l'infrastructure de l'expérience CUORE (Cryogenic Underground Observatory for Rare Events). Cette expérience de recherche de la désintégration $0\nu2\beta$ avec des bolomètres de $TeO_2$, installée au laboratoire souterrain du Gran Sasso, est la première installation bolométrique d'une tonne. CUPID vise à améliorer le niveau du bruit de fond et les performances du détecteur. CUPID-Mo phase I est un démonstrateur à 20 cristaux de $Li_2{}^{100}MoO_4$ (2.34 kg de $^{100}$Mo) enrichis, visant à confirmer la reproductibilité et les performances des bolomètres à scintillation développés par LUMINEU pour les recherches sur la désintégration $0\nu2\beta$ avec l'isotope $^{100}$Mo, installé au laboratoire souterrain de Modane. L'assemblage et l'installation des détecteurs, ainsi que l'estimation de la sensibilité, sont décrits dans le chapitre 5. La préparation des détecteurs, l'assemblage et l'installation dans le cryostat, qui représentent une partie importante de l'activité présentée, sont décrits en détails. L'acquisition des données pour une durée de six mois est en cours avec un niveau de bruit de fond de $10^{-3}$ coup/keV/kg/an. Cette expérience établira la meilleure limite sur la désintégration double bêta sans neutrino du $^{100}$Mo et la mesure la plus précise du mode de désintégration double bêta avec neutrino, autorisée par le Modèle Standard. Les bolomètres scintillants au $Li_2{}^{100}MoO_4$ ont été choisis comme technologie principale pour l'expérience CUPID. Il a donc été décidé de commencer la seconde phase de l'expérience CUPID-Mo en développant un nouveau démonstrateur ayant une structure similaire à celle de CUORE avec les cristaux de $Li_2{}^{100}MoO_4$. Cette phase prévoit 28 cristaux cubiques (45×45×45 mm), 26 enrichis et 2 naturels.

Une telle géométrie permet une utilisation plus efficace de l'espace dans le cryostat et s'adapte au design de CUORE avec quelques modifications mineures (ajout de détecteurs de lumière dans les nouvelles tours). L'expérience acquise grâce aux résultats de la phase I et II de CUPID-Mo sera le point de départ pour CUPID. Sa configuration est en cours de discussion. En utilisant des bolomètres scintillants avec des cristaux de $Li_2{}^{100}MoO_4$, le cryostat de CUORE pourra accueillir environ 300 kg de $^{100}$Mo. La sensibilité à la masse effective de Majorana estimée pour une exposition de $10^3$ kg×an (i.e. après 3 années de prise de données) est de 20 à 30 meV, ce qui permet de couvrir complètement la hiérarchie de masse inversée. Une telle expérience cryogénique sera très compétitive par rapport à d'autres expériences à l'échelle de la tonne grâce à une résolution en énergie élevée et à une puissante réjection du bruit de fond.

Un autre prototype en développement pour CUPID, CUPID-0, est décrit au chapitre 6. CUPID-0 recherche la double désintégration bêta sans neutrinos du $^{82}$Se avec 26 bolomètres scintillants enrichis en $Zn^{82}Se$ (5.28 kg de $^{82}$Se). Le Q de réaction du $^{82}$Se est de 2998 keV, ce qui est supérieur au maximum de la radioactivité $\gamma$. Le bruit de fond $\alpha$ peut être supprimé grâce à la discrimination des particules par le scintillateur. L'abondance naturelle du $^{82}$Se est de 8.73 %, l'enrichissement se fait par centrifugation. En utilisant la discrimination des événements $\alpha$ grâce à la forme des signaux de lumière de scintillation, et au veto sur un retard des coïncidences, le démonstrateur a atteint un niveau de bruit de fond remarquable de $3.6^{+1.9}_{-1.4}\times10^{-3}$ coups/keV/kg/an. La limite obtenue sur la demi-vie de la désintégration $0\nu2\beta$ du $^{82}$Se est de $T^{1/2} = 2.4\times10^{24}$ ans pour une exposition du $^{82}$Se de 1,83 kg×an. Actuellement, c'est la meilleure limite sur la demi-vie de désintégration $0\nu2\beta$ du $^{82}$Se. La prise de données est en cours pour atteindre une exposition de 10 kg×an pour le ZnSe.

Le chapitre 7 décrit les activités de R&D liées aux recherches bolométriques pour la physique des neutrinos, menées dans le cadre de cette thèse. Ces activités comprenaient la caractérisation des senseurs thermiques et des tests de nouveaux composés cristallins sous forme de bolomètres. Ces activités sont importantes pour le développement d'une expérience viable à grande échelle, car elles permettent de développer la technologie, d'étudier des nouveaux senseurs aux propriétés potentiellement meilleures et de fournir de nouveaux bolomètres pour diverses applications. L'une des activités était liée à la caractérisation des thermistances à semi-conducteurs. Les thermistances NTD au Ge sont des capteurs bien connus, faciles à utiliser et qui correspondent bien aux exigences des expériences bolométriques de recherche de désintégration $0\nu2\beta$, en termes de radio-pureté et de performances. La production en série de capteurs NTD est nécessaire pour la construction d'une expérience bolométrique à grande échelle avec un grand nombre de détecteurs. Les premiers tests sur les NTD, produits dans le cadre de LUMINEU, ont donné des résultats prometteurs : la performance des échantillons

testés est similaire à celle des NTD "de référence", actuellement utilisés dans les recherches de désintégration $0\nu2\beta$. Si l'homogénéité des échantillons est confirmée, les capteurs thermiques testés pourront être utilisés lors de futures mesures avec détecteurs bolométriques. Une autre activité de R&D menée durant cette thèse est liée à l'étude de la diffusion cohérente élastique de neutrinos sur noyau (CENNS), qui éveille un intérêt particulier en physique des neutrinos depuis sa découverte récente. Une étude précise de ce processus nécessite différentes sources de neutrinos. L'expérience de R&D BASKET vise à étudier des CENNS avec des bolomètres de $Li_2WO_4$. En plus de la haute résolution en énergie, commune à tous les détecteurs bolométriques, les cristaux de $Li_2WO_4$ peuvent fournir une identification neutronique efficace grâce à leur teneur naturelle en $^6$Li (7.59 %). La discrimination des particules pour la réjection de bruit de fond peut être effectuée à la fois à l'aide des détecteurs de lumière (lumière de scintillation pour la discrimination $\alpha$) ou par l'analyse de la forme des signaux lumineux. Dans le cadre du projet BASKET, le premier test d'un cristal de $Li_2WO_4$ utilisé comme bolomètre a été réalisé. Ce détecteur a montré une bonne performance et une haute résolution en énergie avec un capteur NTD. La réjection des événements de capture neutronique sur $^6$Li (réaction $^6$Li(n, $\alpha$)t) a été réalisée à la fois avec la lumière et la forme des signaux.

Ce travail de thèse consiste en une étude expérimentale en physique des neutrinos grâce aux techniques bolométriques. Il a inclu la préparation, l'assemblage et l'installation de détecteurs, la maintenance du dispositif expérimental cryogénique et l'analyse de données obtenues grâce à des bolomètres scintillants. Plusieurs mesures de R&D avec d'excellents résultats ont été effectuées. Deux démonstrateurs, visant à démontrer l'existence de la réaction de double désintégration bêta sans neutrino, sont en cours de construction et en cours de traitement. L'objectif principal de l'activité de doctorat a été atteint: une technologie éprouvée de bolomètres scintillants destinée aux recherches sur la double désintégration bêta sans neutrino a été mise au point. La technologie des bolomètres à scintillation $Li_2^{100}MoO_4$ constitue une base de référence pour l'expérience CUPID. L'expérience décrite dans ce manuscrit sera prise en compte lors de la préparation d'une expérience cryogénique à l'échelle de la prochaine génération pour la double désintégration bêta.

# *Acknowledgements*

Foremost, I would like to express my sincere gratitude to my advisor Claudia Nones for the continuous support of my Ph.D study and research, for her patience, motivation, enthusiasm, and immense knowledge. Her guidance helped me in all the time of research and writing of this thesis. I could not have imagined having a better advisor and mentor for my Ph.D study.

I am also grateful to Andrea Giuliani for his guidance, I was studying a lot from him, working in his group is a pleasure.

I would like to express my great appreciation to Denys Poda, who was teaching and helping me a lot, having enough patience for me through these years.

I am happy to have made this way together with Valentina Novati and hope that our ways will cross again.

I am grateful to all of those with whom I have had the pleasure to work during this and other related projects: Emiliano Olivieri, Stefanos Marnieros, Bernard Paul, Pierre de Marsillac, Loius Dumolin, Maurice Chapellier, Stefano Pirro, Luca Patavina, Michele Mancuso, Volodymir Tretyak, Vladislav Kobychev and many other people, that I have met during these three years.

I want to thank Fedor Danevich for this opportunity and for the experience, that I received during my studies in LPD department.

Claudia Rusconi, my clean room teacher, the weeks underground with you were a pleasure.

Thanks to my family for constant care and support. Last, but not least, I want to thank a person who became my husband during the PhD and always helped me to get through anything.

# Contents

# Chapter 1

# Neutrino physics

## 1.1 History of neutrino

Neutrino is a fundamental particle which was predicted in 1930 by Pauli in a famous letter addressed to the participants of a nuclear conference. This hypothesis became a basis for a beta decay theory, which was developed in 1933 by Fermi [1]. Neutrino was presented as an explanation of continuous $\beta$-spectrum with a maximum at 1/3 of decay energy value, in contrast to $\alpha$ or $\gamma$ decays, where monochromatic peaks appear in the spectrum. The solution was a model of a three-body decay, where one of the emitted particles could not be observed by a detector. Due to conservation laws, this particle was predicted to have zero charge and spin 1/2. In such case $\beta$ decay is represented as follows:

$$N(A, Z) \rightarrow N(A, Z + 1) + e^{-} + \bar{\nu} \tag{1.1}$$

$$N(A, Z) \rightarrow N(A, Z - 1) + e^{+} + \nu \tag{1.2}$$

At that time only few elementary particles were described and detected in experiments: electrons, positrons, protons and neutrons. So neutrino can be called one of the oldest elementary particles. In 1937 [2] E. Majorana proposed a theory of truly neutral particles with spin equal to 1/2 (which today are called Majorana particles). It is still an open problem if the neutrino is a truly neutral Majorana particle or a Dirac particle which possesses a lepton number.

The cross-section of neutrino interaction with nuclei was estimated by Bethe and Peierls in 1934 [3]. This value was so small that neutrino was thought to be an "undetectable particle" for a long time, but already in 1946 Pontecorvo proposed the radiochemical method of neutrino detection [4]. It is based on an interaction of a neutrino with $^{37}$Cl:

$$\nu_e + {}^{37}Cl \rightarrow e^{-} + {}^{37}Ar \tag{1.3}$$

Sun and reactors were suggested to be used as intense neutrino sources. The first experimental confirmation of antineutrino existence was provided only in 1956 by Cowan and Reines [5]. In their experiment, a nuclear reactor was used as a source of antineutrinos with a flux of $5{\times}10^{13}$ antineutrinos/sec/cm$^2$. In the first phase, the detector volume

was filled with water and the inverse beta decay reaction on the proton was considered as the signature of neutrino existence:

$$\overline{\nu_e} + p \rightarrow n + e^+ \tag{1.4}$$

The $\gamma$ rays from electron-positron annihilation in delayed coincidence with $\gamma$ ray emission by neutron capture on nucleus give a strong evidence of such a reaction. The tanks with liquid scintillator, surrounding the water containers, were used for gamma rays detection. The first phase did not give an outcome with a strict conclusion on neutrino existence. After an upgrade, the second phase of the experiment was performed with cadmium chloride solution in the tank to tag the neutrons more efficiently through reaction:

$$n + {}^{108}Cd \rightarrow {}^{109m}Cd \rightarrow {}^{109}Cd + \gamma \tag{1.5}$$

The measured cross section for the reaction was $6.3{\times}10^{-44}$ cm$^2$ with a prediction of about $6{\times}10^{-44}$ cm$^2$. The experimental confirmation of neutrino existence strongly stimulated the progress on the development of theories including neutrino interactions.

In 1957 a theory of the massless two-component neutrino was developed by Landau [6], Lee and Yang [7] and Salam [8]. In this framework, the neutrino is defined as the left-handed particle and the antineutrino is the right-handed particle. Under the inversion of the coordinate system, the state of the left-handed particle is transformed into the state of the right-handed particle. In the two-component theory in which the neutrino is a particle with definite helicity (projection of the spin on the direction of momentum) parity is violated maximally.

The same year Pontecorvo suggested that neutrinos have small masses and the total lepton number can be violated. Neutrino oscillation possibility was described, considering the similar process of $K^0$-$\bar{K}^0$ oscillations [9].

In 1958 the helicity of the neutrino was determined by Goldhaber, Grodzins and Sunyar in an experiment from the measurement of the circular polarization of $\gamma$ -quanta in a chain of reactions with $^{152}$Eu [10].

In 1962 the Brookhaven neutrino experiment, the first experiment with high-energy accelerator neutrinos, have established that neutrinos, which take part in weak interaction together with electrons and with the muons, are different particles. They were called electron neutrino $\nu_e$ and muon neutrino $\nu_\mu$ [11].

The solar neutrinos were detected for the first time using Pontecorvo method through $^{37}$Cl reaction (see Eq. 1.3). The observed rate of neutrinos was 2–3 times smaller than the rate, predicted by the Standard Solar Model (SSM) [12]. This issue was called solar neutrino problem. The attempts to explain this discrepancy at first were related to Sun model: if temperature and pressure in the Sun core would be lower than what was calculated, the neutrino flux would be less intense. However, with helioseismological observations, it was confirmed that interior Sun

temperatures are in agreement with SSM. Moreover, the neutrino energy spectrum from the sun demonstrated that to produce neutrinos of observed energies the high temperature of the Sun core is required. The solar neutrino problem raised many theories of neutrino physics and pushed forward the development of new neutrino observatories.

The discovery of a new class of the weak interaction, which is called neutral currents (NC), was announced in 1973. Data were obtained in the experiment with high energy accelerator neutrinos at CERN [13].

In 1988 the existence of the solar neutrino problem was confirmed with the Kamiokande observatory [14]. In this experiment, the neutrino flux from the solar $^8B$ reaction was determined through the detection of the recoil electrons in the scattering process of neutrino and electron.

The same year L. Lederman, M. Schwartz, and J. Steinberger were awarded the Nobel Prize for "the discovery of the muon neutrino leading to classification of particles in families", underlining the importance of neutrino questions in particle physics.

In the GALLEX [15] and SAGE [16] experiments solar electron neutrinos were detected by the radiochemical method in the process

$$\nu_e + ^{71}Ga \rightarrow e^- + ^{71}Ge \tag{1.6}$$

The flux of solar neutrinos measured in these experiments was about two times smaller than the one predicted by the SM, providing another confirmation of the solar neutrino problem. The new results were promoting the development of new physics with neutrino as well as rising interest to the theory of neutrino oscillations.

For the confirmation of the transition of different neutrino flavors, a bigger scale of detectors with low background was required. The Kamiokande experiment was upgraded, to hold in the detector volume 50 ktons of ultrapure water. As a result, the first model-independent evidence for neutrino oscillations was observed in 1998 in the Super-Kamiokande experiment [17]. In this case, the observed neutrinos were those produced in the top layers of the atmosphere by the interactions of the primary cosmic radiation.

In 2000 the DONUT experiment at Fermilab obtained the first direct evidence of the existence of the third neutrino $\nu_\tau$ flavor [18], confirming the predicted theory of three-flavor neutrinos.

In 2002 in the SNO experiment, solar neutrinos were detected through the observation of the charged current reaction

$$\nu_e + d \rightarrow e^- + p + p \tag{1.7}$$

and also the neutral current reaction

$$\nu_x + d \rightarrow \nu_x + n + p \quad (x = e, \mu, \tau) \tag{1.8}$$

In combination with Super-Kamiokande measurements, SNO results proved that solar $\nu_e$ on the way from the central part of the sun to

the earth are transformed into other types of neutrinos [19]. In the long-baseline accelerator neutrino experiment K2K (KEK to Kamioka) neutrinos from the accelerator at KEK (The High Energy Accelerator Research Organization, Ko Enerugi Kasokuki Kenkyu Kiko) were detected by the Super-Kamiokande detector at a distance of about 250 km with the observation of neutrino oscillations [20]. KamLAND first reported on electron antineutrino disappearance from a reactor as a source [21], at a baseline where the oscillation process is driven by the so-called solar neutrino-mass splitting (see Section 1.3). Such disappearance was observed about ten years later also by Daya Bay at a much shorter baseline, this time driven by the atmospheric neutrino-mass splitting [22].

Confirmation of neutrino oscillation had resolved the solar neutrino problem but opened a new page for particle physics. As neutrino oscillations prove that neutrinos are not massless, the mass determination is required.

The most recent discovery in neutrino field is the observation of coherent elastic neutrino-nucleus scattering (CEvNS) [23], which was predicted by the Standard Model. Precision measurements on CEvNS can give us information on non-standard neutrino interactions, sterile neutrinos, neutrino magnetic moment and other neutrino properties.

### 1.1.1 Summary

At present twelve fundamental fermions are known: six quarks $u$, $d$, $c$, $s$, $t$, $b$, three charged leptons $e$, $\nu$, $\tau$ and three neutrinos $\nu_e$, $\nu_\mu$, $\nu_\tau$ (see Fig.1.1). All of them interact via the electroweak force with photons and $W^{\pm}$, $Z$ bosons. Even if neutrinos are described in the same way in the Lagrangian of the electroweak interaction, as quarks and charged leptons, they are very special particles and the two main differences from other fundamental fermions are:

- The neutrinos cross-section of the interaction with matter is many orders of magnitude smaller than the cross-section of any other leptons. This is due to the fact that neutrinos are the only particles in the SM that interact solely via weak interactions.

- Neutrino masses are many orders of magnitude smaller than the masses of any other massive fundamental particles.

Still, after more than 80 years of neutrino studies, the whole picture of neutrino physics is not complete. Measurement of such small masses is a challenging problem, which is not yet solved. Small neutrino masses cannot be naturally explained in the framework of SM by the Higgs mechanism of mass generation. New physics and a new mechanism of neutrino mass generation beyond the Standard Model are required. To reveal new physics, various high-precision experiments (T2K, Double CHOOZ, Daya Bay, RENO, NOvA, JUNO and DUNE) are taking measurements or will be started during the next years.

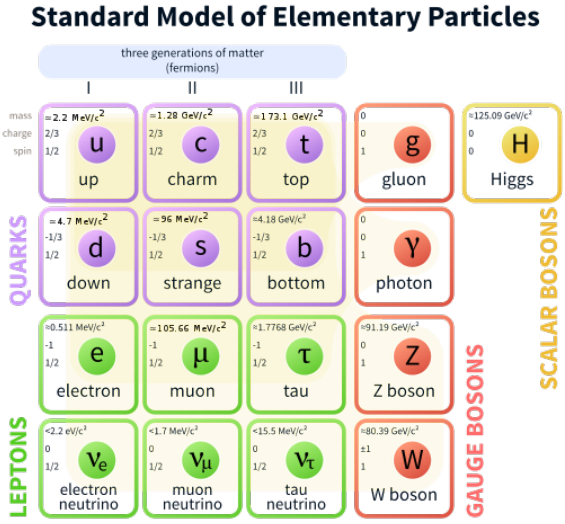


FIGURE 1.1: The schematic view of matter structure in Standard Model of elementary particles. The three generations of matter are shown in first three columns, gauge bosons in the fourth column, and the Higgs boson in the fifth. Figure taken from [24].

## 1.2 Neutrino oscillations

As mentioned above, the possibility of neutrino-antineutrino oscillations was suggested in 1957 by Pontecorvo, in analogy to kaon oscillations [9]. Later on, oscillations between different neutrino flavours were taken into consideration. This is a quantum-mechanical phenomenon due to the fact that neutrino flavor fields are superpositions of neutrino mass fields with mixing relation:

$$|\nu_l\rangle = \sum_i^3 U_{li}^* |\nu_i\rangle \tag{1.9}$$

where U is the 3×3 unitary Pontecorvo, Maki, Nakagawa, Sakata (PMNS) mixing matrix which has parametrization:

$$\begin{pmatrix} c_{12}c_{13} & s_{12}c_{13} & s_{13}e^{-i\delta} \\ -s_{12}c_{23} - c_{12}s_{23}s_{13}e^{i\delta} & c_{12}c_{23} - s_{12}s_{23}s_{13}e^{i\delta} & s_{23}c_{13} \\ s_{12}s_{23} - c_{12}c_{23}s_{13}e^{i\delta} & -c_{12}s_{23} - s_{12}c_{23}s_{13}e^{i\delta} & c_{23}c_{13} \end{pmatrix} diag(e^{i\lambda_1}, e^{i\lambda_2}, 1)$$

where $c_{ab} = \cos\theta_{ab}$, and $s_{ab} = \sin\theta_{ab}$ with three mixing angles $\theta_{ab}$. $\delta$ is Dirac CP-violating phase, and $\lambda_1, \lambda_2$ are Majorana CP-violating phases, which contribute to processes where total lepton number is violating, like neutrinoless double beta decay (this process will be described in Chapter 2). Neutrino flavors are produced in charged-current weak processes. With neutrino propagation, the flavor can oscillate, and the probability for a neutrino born in flavor state $s$ to be observed in a

state $f$ is following:

$$P(\nu_s \to \nu_f) = \delta_{sf} - 4\sum_{i>j} Re(U^*_{si}U^*_{fi}U^*_{sj}U^*_{fj})sin^2(1.27\Delta m^2_{ij}L/E)\pm \\ 2\sum_{i>j} Im(U^*_{si}U^*_{fi}U^*_{sj}U^*_{fj})sin^2(2.54\Delta m^2_{ij}L/E) \tag{1.10}$$

Where $L$ is the travel distance in km, $E$ is neutrino energy in GeV, and $\Delta m^2_{ij} = m^2_i - m^2_j$ in eV$^2$. The observable of neutrino oscillations can be either disappearance of $\nu_s$, or $\nu_f$ appearance depending on the energy E and the baseline L. Neutrino oscillation experiments can be divided according to the type of source:

- ***Solar neutrinos***, generated in the Sun core in pp-chain reaction and in the CNO-cycle, whose net effect is:

$$4p \to^4 He + 2e^+ + 2\nu_e \tag{1.11}$$

- ***Atmospheric neutrinos***, generated by an interaction of cosmic rays with atomic nuclei in the atmosphere, for example, pions and muons:

$$\pi^\pm \to \mu^\pm + \nu_\mu \tag{1.12}$$

$$\mu^\pm \to e^\pm + \nu_\mu + \nu_e(\bar{\nu_e}) \tag{1.13}$$

- ***Reactor or accelerator neutrinos***, generated by radioactive decays following nuclear fission or artificially caused reactions.

Independent of the source, such kind of experiments requires enormous detector masses. They are Cherenkov detectors, based on ultrapure liquid scintillator detectors or radiochemical searches. Such experiments, as KamLAND, GALLEX, SNO, Borexino, Super-Kamiokande, Daya Bay, Nova provided data on neutrino oscillations from different sources. The combined results are giving a three-flavor picture with the PMNS matrix parameter values, shown in Tab. 1.1.

TABLE 1.1: Parameters of PMNS matrix, obtained by global analysis of neutrino oscillations data from recent experiments [25].

| Parameter | NH (best fit) | IH (best fit) | References |
|---|---|---|---|
| $\Delta m^2_{21}$ | $7.56\pm0.19\times10^{-5}$eV$^2$ | | [26] [27] |
| $\lvert\Delta m^2_{31}\rvert$ | $2.55\pm0.04\times10^{-3}$eV$^2$ | $2.49\pm0.04\times10^{-3}$eV$^2$ | [28], [29] |
| $\theta_{12}$ | $34.5^{+1.1}_{-1.0}$ | | [26] [27] |
| $\theta_{23}$ | $41.0\pm1.1$ | $50.5\pm1.0$ | [28], [29] |
| $\theta_{13}$ | $8.44^{+0.18}_{-0.15}$ | $8.44^{+0.16}_{-0.17}$ | [25] |
| $\delta$ | $252^{+56}_{-36}$ | $259^{+47}_{-41}$ | [25] |

Neutrino-oscillation discovery is one of the most significant recent achievements in particle physics: it proves that neutrinos do have mass.

Now, this knowledge leads to a new fundamental problem, which has to be solved: determination of massive neutrinos nature. They can be four-component Dirac particles with conservation of lepton number L or two-component Majorana particles, which are completely neutral – they have no electric charge and no lepton number. It is impossible to get the answer with the neutrino oscillation experiments because in oscillation transitions $\nu_l \to \nu_{l'}$ lepton number is conserved.

## 1.3 The absolute scale of neutrino mass

As it was mentioned before (see Eq. 1.9), in the three-flavor model the neutrinos have three eigenstates with masses $m_1$, $m_2$, $m_3$. Neutrino oscillation experiments allow us to determine only the difference of the squares of the neutrino masses. The value obtained in solar neutrino

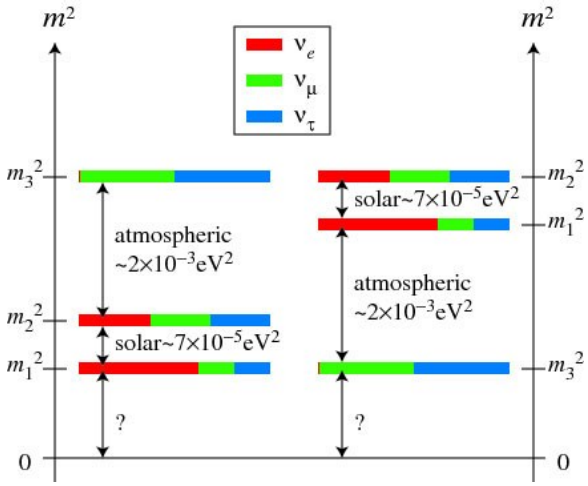


FIGURE 1.2: The two possible neutrino mass hierarchies. Figure is taken from [30].

experiments measuring $\nu_e$ disappearance is called $\Delta m^2_S = \Delta m^2_{12}$, and its sign is known. Regarding the $\nu_\mu$ oscillations from atmospheric flux the following value is obtained: $\Delta m^2_A = \frac{1}{2}|\Delta m^2_{13} + \Delta m^2_{23}|$. Only its absolute value can be measured, giving two possible allowed patterns of neutrino masses (see Fig. 1.2): Normal mass spectrum (NS): $m_{min} = m_1$:

$$m_2 = \sqrt{m^2_{min} + \Delta m^2_S}, m_3 = \sqrt{m^2_{min} + \Delta m^2_A + \Delta m^2_S/2} \tag{1.14}$$

Inverted mass spectrum (IS): $m_{min} = m_3$:

$$m_1 = \sqrt{m^2_{min} + \Delta m^2_A - \Delta m^2_S/2}, m_2 = \sqrt{m^2_{min} + \Delta m^2_A + \Delta m^2_S/2} \tag{1.15}$$

Depending on masses, there are three extreme possibilities:

- Normal hierarchy: $m_1 \ll m_2 \ll m_3$. In this case

$$m_1 \ll m_2 \simeq \sqrt{\Delta m_S^2} \approx 9 \times 10^{-3} eV, m_3 \simeq \sqrt{\Delta m_A^2} \approx 5 \times 10^{-2} eV.$$

$$m_2 = \sqrt{m_{min}^2 + \Delta m_S^2}, m_3 = \sqrt{m_{min}^2 + \Delta m_A^2 + \Delta m_S^2/2}$$

- Inverted hierarchy: $m_3 \ll m_1 \lesssim m_2$. In this case

$$m_3 \ll m_1 \lesssim m_2 \simeq \sqrt{\Delta m_A^2} \approx 5 \times 10^{-2} eV$$

- Quasi-degenerated spectra: $m_1 \lesssim m_2 \lesssim m_3 \simeq m_\nu^{QD}$ in the normal scheme and $m_3 \lesssim m_1 \lesssim m_2 \simeq m_\nu^{QD}$ in the inverted scheme, with

$$m_\nu^{QD} \gg \sqrt{\Delta m_A^2} \approx 5 \times 10^{-2} eV$$

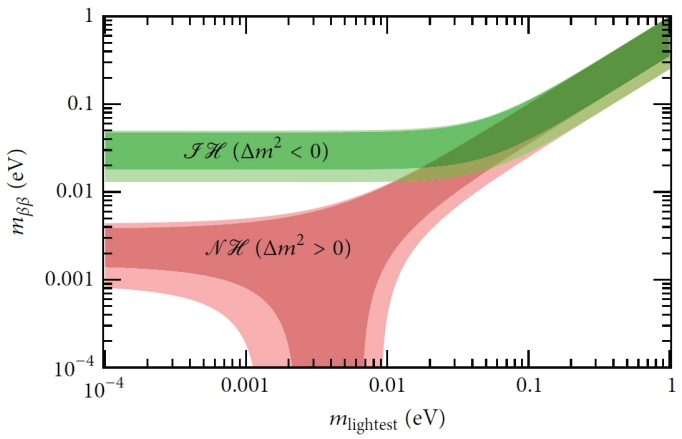


FIGURE 1.3: Effective Majorana neutrino mass as a function of the lightest neutrino mass in the normal hierarchy $m_1 < m_2 < m_3$ (red), and in the inverted hierarchy $m_3 < m_1 < m_2$ (green) scenarios. The shaded areas correspond to the $3\sigma$ regions due to the uncertainties on the oscillation parameters [31].

If neutrinos are Majorana particles, the Majorana mass term can be described as follows:

$$\mathcal{L}(x) = \frac{1}{2} \sum_{l,l'=e,\mu,\tau} \nu_l C^{-1} M_{ll'} \nu_{l'} + h.c. \tag{1.16}$$

$M_{ll'}$ is the term, that provides the lepton number violation. With the diagonalization of neutrino mass matrix the effective Majorana mass

term can be determined:

$$m_{\beta\beta} = |\sum_{i=1,2,3} U_{ei}^2 M_i| \tag{1.17}$$

$m_{\beta\beta}$ depends on the three neutrino mass eigenvalues, and $U_{ei}$ is the PMNS mixing matrix with two additional Majorana phases [32]. $m_{\beta\beta}$ can be described as a function of the lightest neutrino mass, given the constraints on the parameters obtained by neutrino oscillation experiments (mixing angles $\theta_{12}$, $\theta_{13}$, and squared mass differences $\Delta m_A^2$, $\Delta m_S^2$). As a result, the dependence shown in the Fig. 1.3 is obtained.

### 1.3.1 Neutrino mass hierarchy: clues favoring normal ordering

As was discussed above, the two possible mass orderings of neutrinos are inverted and normal hierarchy. Multiple efforts are ongoing to obtain the conclusion on the mass ordering. NOvA and T2K collaborations recently reported on disfavoring the inverted hierarchy [33],[34]. NOvA is a neutrino oscillation experiment, designed to observe muon to electron neutrino oscillations. The far and near detectors are 14 kton and 0.3 kton liquid scintillator volumes respectively. The muon neutrino beam is produced at Fermilab (the distance to detector is 810 km). The $\nu_e$ appearance experiments with enough statistics would allow determining the neutrino mass hierarchy, as in case of coherent forward neutrino scattering on electrons in the terrestrial medium the electron neutrino appearance probability is enhanced given the normal mass hierarchy, and it is suppressed for inverted mass hierarchy. With

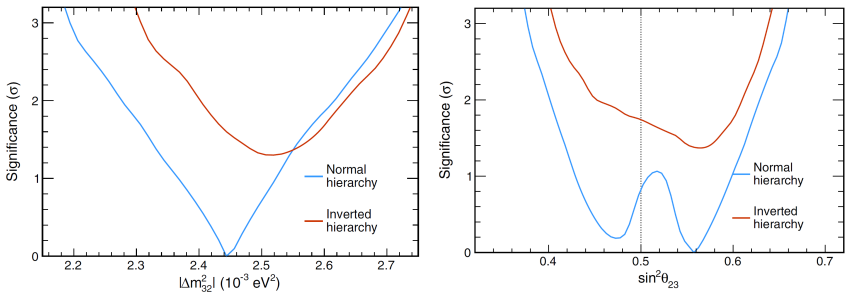


FIGURE 1.4: Significance at which each value of $|\Delta m_{23}^2|$ (left) and each value of $sin^2\theta_{23}$ (right) is disfavored in the normal (blue, lower) or inverted (red, upper) mass hierarchy. The vertical dotted line indicates the point of maximal mixing [33].

the new data, obtained by the NOvA collaboration [33] the global fit of oscillation parameters was performed for each relevant mass hierarchy and $\theta_{23}$ octant combinations. In Fig. 1.4 the significance level for two possible hierarchies depending on oscillation parameters is shown.

The significance level for the rejection of the inverted hierarchy was calculated by profiling over all the other physics parameters and the systematic uncertainties. A joint fit to the data for $\nu_{mu}$ disappearance and $\nu_e$ appearance gives the best-fit point as normal mass hierarchy. The inverted mass hierarchy is disfavored at 95% C. L. for all choices of the other oscillation parameters.

These results have close connection with the mass parameter $m_{\beta\beta}$, which is relevant for double beta decay (this process is the main subject of this thesis and it is described in details in Chapter 2). The next generation of double beta decay experiments is expected to investigate fully the inverted hierarchy region during the next decade and also the part of the normal hierarchy region defined by $m_l$>15-20 meV. Of course, the indications favoring normal mass hierarchy, imply the need of even higher sensitivity double beta decay experiments in order to access to the remaining part of the normal hierarchy region. In any case, recent estimations of probability distributions for the effective Majorana mass [35] are demonstrating that even for normal ordering double beta experiments can still probe a relevant region of the parameter space and give a valuable return on investment. These conclusions are based on the assumption that the distributions of the neutrino mass parameters and of the Majorana phases are flat (the so-called "anarchy" model) within the region currently allowed by experiments and observations, and without a specific physical mechanism that drives to zero the lightest neutrino state or the Majorana mass. As shown in Fig. 1.5, the maximum probability density is located in region of $m_{\beta\beta}$ between 100-10 meV, which correspond to sensitivity of next-generation double beta experiments. On the other hand, observation of neutrinoless double

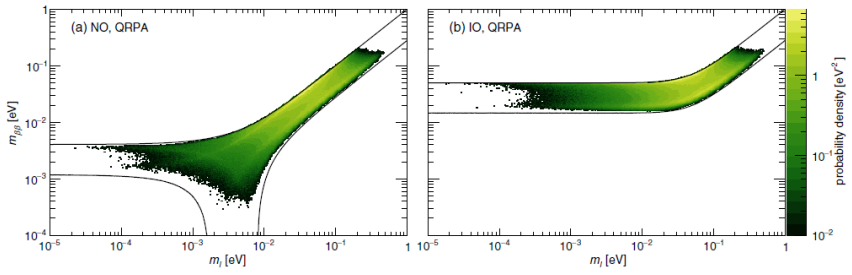


FIGURE 1.5: Marginalized posterior distributions for $m_{\beta\beta}$ and $m_l$ for NO (a) and IO (b). The solid lines show the allowed parameter space assuming $3\sigma$ intervals of the neutrino oscillation observables from NuFIT. The plot is produced assuming QRPA NMEs and the absence of mechanisms that drive $m_l$ or $m_{\beta\beta}$ to 0. The probability density is normalized by the logarithm of $m_{\beta\beta}$ and $m_l$. Figure taken from [35].

beta decay in the close future in the inverted hierarchy region would suggest that this transition is mediated by a different mechanism than

the light neutrino exchange. Therefore, development of new physics explaining such mechanism will be required.

Recent computations on combined results from cosmological experiments [36] also favor the normal mass hierarchy, but these computations are model-dependent and require further confirmation from other kinds of experiments.

### 1.3.2 Neutrino mass interpretation in the Standard Model

In the minimal SM formulation neutrinos were predicted to be massless, but the oscillation experiments have proved the opposite. For this reason, SM has to be extended, including the massive neutrinos, and there are several possible mechanisms. Many advanced theories include the so-called see-saw mechanism. It is based on Lagrangian formalism and the existence of Majorana and Dirac mass terms.

In the SM quark and charged lepton fields are right and left-handed, and neutrino fields were considered to be only left-handed in massless approach for the neutrino. If the right-handed are also assumed to be SM fields, then the neutrino masses can be generated by standard Higgs mechanism through Yukawa interaction:

$$L_I^Y = -\sqrt{2}\sum_{l'l} \overline{L_{l'L}} Y_{l'l} \nu_{lR} \Psi + h.c. \tag{1.18}$$

If we add Majorana mass term, it can be done only in the framework of a theory beyond the SM, because it violates total lepton number L. In such way neutrino masses are generated by the interaction of the lepton and Higgs doublets with heavy Majorana leptons with several outcomes:

- If neutrinos have definite masses, they are Majorana particles.
- Neutrino masses are of the order of fermion mass but suppressed by a factor which is given by the ratio of Higgs vacuum expectation value and the scale of lepton number violation.
- In addition to light neutrinos, there are heavy neutral Majorana leptons (with a mass scale determined by the parameter $\Lambda \approx 10^{15}$ GeV) that cannot be produced in accelerators.
- The number of lepton generations (three) is equal to the number of light massive neutrinos.

Neutrinoless double beta decay observation would provide a strong indication in favor of this scheme – in addition CP-violation in decays of the heavy leptons in the early universe could be the reason of the baryon asymmetry through so-called leptogenesis mechanism [37].

### 1.3.3 Measurement of neutrino masses

Being the most abundant fermion in the Universe, the knowledge on the absolute value of neutrino masses will give an essential information for numerous physics fields. In astrophysics and cosmology, the neutrinos played a significant role in the universe structure formation, including the matter-antimatter asymmetry. The value of neutrino masses can be a crucial parameter for the possible extensions of Standard Model or new unified theories in particle physics.

The measurement of neutrino masses is a challenging objective. As neutrinos interact only via the weak force, the typical way to measure the particle mass (direct kinematic measurement of two independent values, that can be combined to obtain the particle mass) cannot be used. Several indirect methods were developed to measure the neutrino mass. One of the most promising ways to determine absolute scale of neutrino masses is the search for $0\nu2\beta$ decay. This is the main subject of this thesis and will be detailed in following sections. Other approaches are described as follows.

#### Single $\beta$ decay

A sensitive and model-independent approach for the determination of neutrino masses is the study of end-point part of the $\beta$-spectrum, which

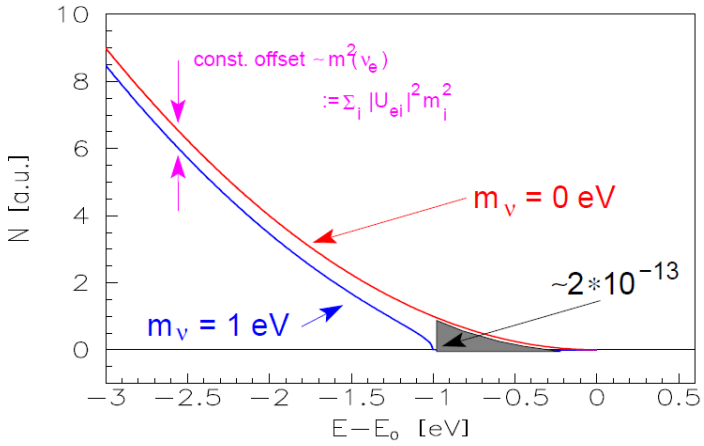


FIGURE 1.6: Endpoint of the $\beta$ spectrum. The red line corresponds to the end point of the spectrum shape with $m_{\nu_e} = 0$ eV, the blue one with $m_{\nu_e} = 1$ eV.

is affected by neutrino masses through a phase-space factor (see Fig. 1.6). Here the neutrino is not observed but the charged decay products are precisely measured. Using energy and momentum conservation the neutrino mass can be obtained. In such an experiment the model-independent bounds on the neutrino masses can be obtained by limiting

the effective electron neutrino mass:

$$m_e^2 = \sum_{k=1}^{3} |U_{ek}|^2 m_k^2 \tag{1.19}$$

A low energy $\beta$-spectrum is required for such kind of experiments and it is important to obtain high energy resolution. The best candidate is tritium decay with a transition energy at 18.6 keV. The endpoint of tritium decay is one of the lowest for all $\beta$ decays and the half-life (12.3 yr) is reasonable from an experimental point of view. In these experiments, the subject of the study is the high-energy end-point of the electron spectrum in the decay:

$$^3H \rightarrow ^3 He + e^- + \bar{\nu_e} \tag{1.20}$$

Another advantage of this decay is given by the fact that it is super-allowed and the electronic structure is simple even in case of molecular tritium. This kind of experiments is based on electrostatic spectrometers with MAC-E filter with a strong tritium source. The lowest limits on the effective electron mass were obtained in Mainz: $m_\beta \leqslant 2.2$ eV [38] and Troitsk: $m_\beta \leqslant 2.05$ eV [39] experiments.

An upgraded version of such spectrometer with a strong gaseous tritium source will be used in the KATRIN experiment [40]. Up-to-date it is the biggest detector of this kind, with a complex system of tritium production and background rejection. Currently, the detector is being tested and calibrated, preparing to start data taking by the end of 2018. The expected measurement will last for five years with the sensitivity goal at $m_\beta \leqslant 0.2$ eV.

Another viable candidate for $\beta$ spectrum endpoint studies is the $^{187}$Re isotope. The transition energy is 2.47 keV, and the half-life is $4.3{\times}10^{10}$ yr. The decay in Eq. 1.21 is the first unique forbidden transition:

$$^{187}Re \rightarrow ^{187} Os + e^- + \bar{\nu_e} \tag{1.21}$$

Even with the advantage of low endpoint energy, the spectrometer detectors cannot be used to measure the $^{187}$Re $\beta$-spectrum due to long half-life and energy losses. The "source=detector" approach was used with $AgReO_4$ cryogenic bolometers (see more on bolometer technique in Chapter 3.). The upper limit on the electron antineutrino mass was obtained at 15 eV [41].

The lowest endpoint of all known $\beta$ decays belongs to second-forbidden unique $\beta^-$ transition:

$$(9/2^+)^{115}In \rightarrow (3/2^+)^{115}Sn* + e^- + \bar{\nu_e} \tag{1.22}$$

with decay energy $Q_\beta$=147±10 eV [42] and partial half-life $T_{1/2}$=$4.3(5){\times}10^{20}$ yr [43]. This decay potentially is a promising option for measurement of neutrino mass, but with current state of technology experimental approach is not developed yet.

An alternative to $\beta$ decay studies can be an investigation of the electron capture (EC) decay of $^{163}$Ho:

$$^{163}Ho^{+} + e^{-} \rightarrow ^{163}Dy_i^{*} + \nu_e \rightarrow ^{163}Dy + E_i + \nu_e \tag{1.23}$$

with an end-point about 2.8 keV. The ECHO and HOLMES experiment will investigate the $^{163}$Ho spectrum with a large array of low temperature microcalorimeters. In the case of HOLMES, the measurement is expected to start in 2018 with calculated sensitivity to neutrino mass at 0.4 eV [44].

### Neutrino mass from cosmology

The combination of cosmological measurements and neutrino experiments, based on Earth can give us essential information on neutrino properties. In cosmological experiments an assumption is used that light massive neutrinos constitute hot dark matter. Only the sum of neutrino masses $\sum_{k=1}^{3} m_{\nu_k}$, is observable in the cosmological experiment as they are searching for neutrino contribution to the matter density.

Analysis of cosmological data using the standard Cold Dark Matter model disfavors masses which are larger than some fractions of eV. The value of the upper bonds depends on model and data sets. The effects of neutrino masses on CMB depends on the physical density of neutrinos, and the eigenstates mass difference can be neglected. However, the transition redshifts are different for the neutrinos of different masses and the mass splitting affects the matter-domination regime.

With the precise measurement of the matter power spectrum, it would be possible to obtain information about the sum of the neutrino masses and mass hierarchy. For the spatially flat universe, latest results of the Planck experiments give us a constraint on the sum of neutrino masses: $\sum_{k=1}^{3} m_k < 0.23$ eV [45]. The Baryon Acoustic Oscillations (BAO) measurements allow to include information about the cosmic expansion and to improve the limit up to $\sum_{k=1}^{3} m_k < 0.13$ eV [46].

## 1.4 Conclusions and perspectives

The neutrinos, in spite of being the most abundant fermions in the universe, are still not explored completely. The phenomenon of neutrino oscillations demonstrates that development of a new complete theory of fundamental interaction is required.

The neutrino masses determination is a hot question in modern physics, but even more important is to confirm the neutrino nature: if it is Majorana particle, the lepton number violation takes place. As an explanation of the naturalness of small neutrino masses, the see-saw mechanism with Majorana mass terms can be implemented in an extension of the current theories of particle physics.

The neutrino properties could give clues to essential features of matter, as matter-antimatter asymmetry, dark matter, leading to complete understanding of our universe mechanisms.

This thesis is focused on neutrinoless double beta decay search as a tool to investigate the neutrino nature and properties. In the next chapters, the double beta decay will be described as well as experimental methods to search for this process.

# Chapter 2

# Double Beta Decay

## 2.1 Double beta decay

Double beta decay is an extremely rare decay in which a nucleus charge changes by two units with the emission of two electrons:

$$(A, Z) \rightarrow (A, Z + 2) + 2e^{-} + 2\bar{\nu}_e \tag{2.1}$$

It was described first by Maria Goeppert-Mayer [47] in 1935 with the evaluation of the half-life for this process $>10^{17}$ years for a decay energy at 10 MeV. Unlike regular $\beta$ decay, which is the first-order process in the classic Fermi theory of weak interaction, $2\beta$ decay is a second-order process.

In principle, this transition can occur in any nucleus $(A, Z)$ as long as the nucleus$(A, Z + 2)$ has smaller mass. But viable candidates for experimental observation of double beta decay are nuclei with an even number of neutrons and protons and where $\beta$ decay is energetically forbidden, or if its probability is strongly suppressed due to the big difference between spins of mother and daughter nucleus (see Fig. 2.1). In case of even-even nuclei, they have smaller masses than odd-odd nuclei due to the pairing interaction, and two single $\beta^{-}$ decays are forbidden, but $2\beta^{-}$ decay is energetically allowed as a second-order process.

There are considered two main modes of $2\beta$ decay: two-neutrino double beta decay ($2\nu2\beta$) and neutrinoless double beta ($0\nu2\beta$) decay. The Feynman diagrams of these processes are shown in Fig. 2.2. An additional decay mode has been proposed in some extensions of the Standard Model with the emission of a light neutral boson, the so-called Majoron ($\chi^0$)[48].

In $2\nu2\beta$ mode nucleus emits two neutrinos and two electrons. This mode is not violating any conservation law, so it is allowed by the SM for any type of neutrinos and there are 35 natural isotopes, predicted to be capable of undergoing double beta decay. It is already observed for 12 nuclei. In this mode, the emitted transition energy $Q_{\beta\beta}$ is distributed between two electrons and two neutrinos. As neutrinos can have variable kinetic energy, electrons have continuous spectrum (see Fig. 2.3).

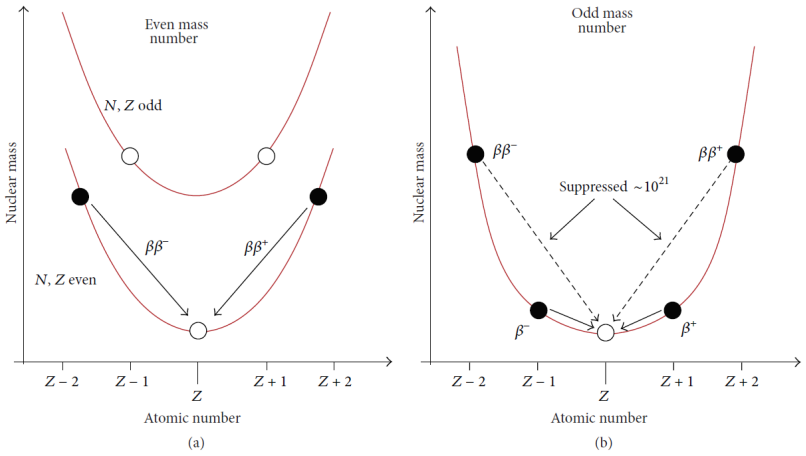


FIGURE 2.1: Nuclear mass as a function of the atomic number A in the case of an isobar candidate with A even (a) and A odd (b).

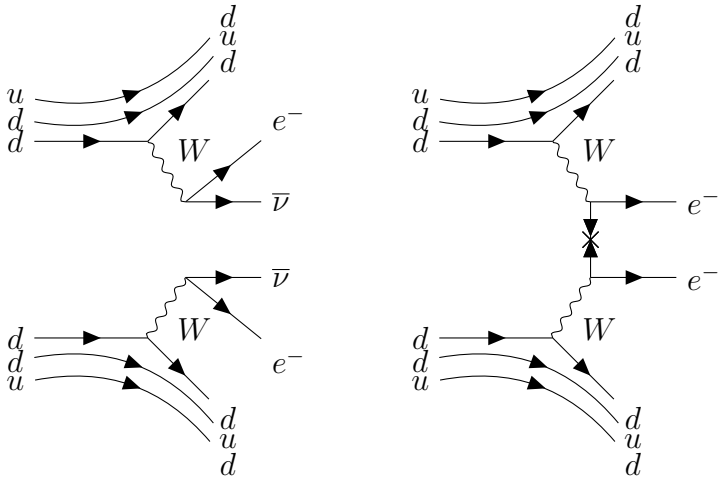


FIGURE 2.2: The Feynman diagrams of the $2\nu2\beta$ (left) and $0\nu2\beta$ decay (right).

Besides $2\beta^-$ decay there are also other possible processes, where the charge of daughter nuclei decreases by two units, such as double positron decay ($2\beta^+$), electron capture with positron emission ($\varepsilon\beta^+$) and double electron capture ($2\varepsilon$):

$$(A, Z) \rightarrow (A, Z-2) + 2e^+ + 2\nu_e \quad (2\beta^+) \tag{2.2}$$

$$e^- + (A, Z) \rightarrow (A, Z-2) + e^+ + 2\nu_e \quad (\varepsilon\beta^+) \tag{2.3}$$

$$2e^- + (A, Z) \rightarrow (A, Z-2) + 2\nu_e \quad (2\varepsilon) \tag{2.4}$$

For all the cases, the decay energy is defined by the difference of masses between mother and daughter atoms:

$$Q_{2\beta_-} = M(A,Z) - M(A,Z+2) \tag{2.5}$$

$$Q_{2\beta_+} = M(A,Z) - M(A,Z-2) - 4m_e c^2 \tag{2.6}$$

$$Q_{\varepsilon\beta_+} = M(A,Z) - M(A,Z-2) - 2m_e c^2 - E_\beta \tag{2.7}$$

$$Q_{2\varepsilon} = M(A,Z) - M(A,Z-2) - E_{\beta 1} - E_{\beta 2} \tag{2.8}$$

$\varepsilon\beta^+$ and $2\beta^+$ processes are strongly suppressed due to an influence of the Coulomb barrier on positrons and small kinetic energy. The half-life for $2\nu2\beta$ decay is described by the formula:

$$(T^{2\nu}_{1/2})^{-1} = G^{2\nu}|NME_{2\nu}|^2 \tag{2.9}$$

where $G^{2\nu}$ is the phase space integral, and $NME_{2\nu}$ are nuclear matrix elements for $2\nu2\beta$ decay.

### 2.1.1 Neutrinoless double beta decay

The double beta decay without neutrino emission was proposed by Furry [49]:

$$(A,Z) \rightarrow (A,Z-2) + 2e^- \tag{2.10}$$

With the emission of two electrons and no neutrinos, the signature of such process will be a mono-energetic line at the transition energy $Q_{\beta\beta}$ (see Fig. 2.3). The principal characteristic of $0\nu2\beta$-decay is the violation of lepton number by two units. Such process can be explained by Majorana nature of neutrino: particles and antiparticles coincide, like in case of photons. The Majorana quantum field can fully describe massive neutrinos, even if it causes different physical predictions than in case of Dirac theory.

#### $0\nu2\beta$ decay rate

$0\nu2\beta$ decay is a transition of the second-order perturbation theory. In case of light neutrino exchange mechanism, the decay rate can be described as following:

$$(T^{0\nu}_{1/2})^{-1} = G^{0\nu} g_A^4 |NME|^2 \langle m_{\beta\beta}\rangle^2 \tag{2.11}$$

Where:

- $\langle m_{\beta\beta}\rangle^2$ is squared modulus of effective Majorana mass $m_{\beta\beta}$ (see Eq. 1.17). This value can be extracted from the measurements of $T^{0\nu}_{1/2}$.
- Squared modulus of nuclear matrix element $NME$, which can be calculated on the basis of nuclear physics theory. But nuclear models describe only approximately many-body interactions and

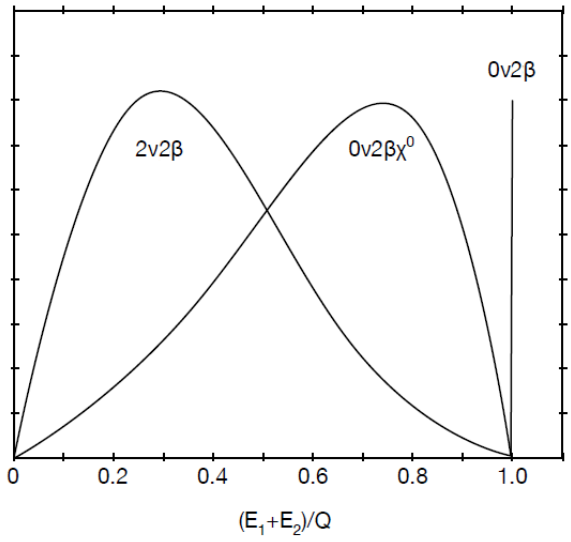


FIGURE 2.3: Scheme of the sum spectra of the kinetic energies of the two emitted electrons in three different $2\beta$ modes: $2\nu2\beta$, $0\nu2\beta$ and $0\nu2\beta\chi^0$ decay with Majoron emission. The amplitudes are arbitrary [50].

depending on the model, the difference between calculated values can be significant.

- The phase-space factor $G^{0\nu}$ is also a result of the calculation. This evaluation is much easier and the calculations are performed with high accuracy.

- The measured value of the axial coupling constant in weak interactions is $g_A = 1.269$ [51]. It is expected to be renormalized. There exist a possibility of strong quenching ($g_A < 1$), and it is still not clear if the quenching is the same both for $0\nu2\beta$ and $2\nu2\beta$ decays. [52]. The $0\nu2\beta$ rate is in fact proportional to $g_A$, and $g_A$ is usually taken as 1.25, a value close to that measured for the free neutron. In fact, $g_A$ remains an open issue, as values much lower than that (even by a factor 2) have been proposed to explain observed $\beta$-decay and $2\nu2\beta$ rates (this $g_A$ quenching would have a negative impact on the $0\nu2\beta$ rate prediction), but the situation is still controversial.

### NME models

The primary goal of $0\nu2\beta$-decay experiments is to prove that neutrinos are Majorana particles and to measure effective Majorana mass. The knowledge of NME $|M^{0\nu}|$ values with reasonable accuracy is very important for conversion of possible half-life measurements to the calculation of neutrino masses.

The $|M^{0\nu}|$ cannot be measured independently, they must be calculated using the theoretical models. However, it is possible to measure the ratio of corresponding NMEs if rates of $0\nu2\beta$-decay for at least two different nuclei are measured.

Calculation of NMEs is a complicated many-body problem, and approximation models have to be used for the computations, which include all the nuclear structure effects of the decay. There are five different models, that are mostly used for the calculation of the nuclear matrix elements for the $0\nu2\beta$-decay:

- NSM: Nuclear Shell Model
- QRPA: Quasi-particle Random Phase Approximation
- IBM: Interacting Boson Model
- EDF: Energy Density Functional
- PHFB: Projected Hartree-Fock-Bogoliubov approach.

Of course, each of these models has its advantages and disadvantages, and the problem is to establish which model provides the most precise calculation. The difference between theoretical estimations is considered as the uncertainty. For all of these models, the value of $|M^{0\nu}|$ also depends on variations of model parameters, like the axial coupling constant $g_A$. As one can see from Fig. 2.4 and Tab. 2.1, looking at the values of NME, within a factor 2-3, there are no isotopes with very high or very low decay rate, and so there are no especially favorable or disfavorable isotopes from experimental point of view.

### Phase space factor

The phase space factor is given by the following equation:

$$G^{0\nu}(Q,Z) = \frac{(G_F \cos\nu_C)^4}{ln2(2\pi)^5 R^2} \int_0^Q dT_1 E_1 |p_1| E_2 |p_2| F(E_1, Z') F(E_2, Z') \tag{2.12}$$

where $T_1 = E_1 - m_e$ is the kinetic energy of emitted electron, $Z' = Z+2$, and $Q = M_i - M_f - 2m_e$ is the transition energy of the process, which is equal to the total released kinetic energy. $G^{0\nu}$ value was calculated with high accuracy for several nuclei, considering the exact Dirac wave functions of the electrons, taking into account the finite nuclear size and electron screening. In Tab. 2.1 the $G^{0\nu}$ values are listed for the most interesting from experimental point of view $0\nu2\beta$ isotopes. The combination of $G^{0\nu}$ and NME can give us an indication of $0\nu2\beta$ decay half life (see Fig. 2.4, bottom panel), and in this case $^{100}$Mo is favored isotope for experimental searches, as would have shorter half-life comparing to other $2\beta$-active isotopes.

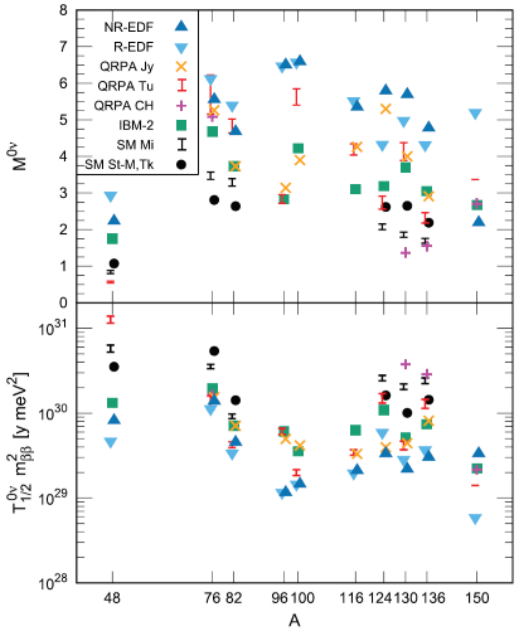


FIGURE 2.4: Top panel: nuclear matrix elements for $0\nu2\beta$ decay candidates from different nuclear models as a function of mass number A. Bottom panel: associated $0\nu2\beta$ decay half-lives, scaled by the square of the unknown parameter $m_{\beta\beta}$ [53].

## 2.2 Experimental searches for $0\nu2\beta$ decay

After the outstanding achievements in neutrino oscillations experiments, other challenging researches are coming up. The observation of $0\nu2\beta$ decay can provide information of great importance for neutrino physics, as mass scale and Majorana nature of neutrinos. However, the challenge appears to be sophisticated due to the very long half-life of this decay. The experimental sensitivity to the half-life of $0\nu2\beta$ decay can be described by following formula, which holds in case of a large number of background counts in the region of interest:

$$T_{1/2}^{0\nu2\beta} \propto a \cdot \epsilon \cdot \sqrt{\frac{M \cdot t}{b \cdot \Delta E}} \tag{2.13}$$

where a is isotopic abundance, $\epsilon$ the detection efficiency, $M$ the source mass, $t$ the exposure time, $b$ - background index and $\Delta E$ is the energy resolution in the region of interest. Looking at these parameters, several crucial points have to be considered in the first place when developing a detector:

- Reduction of the background
- Registration efficiency
- Energy resolution

TABLE 2.1: Phase-space factors [54] and nuclear matrix elements [55], calculated for several $0\nu2\beta$ candidate nuclei.

| Nucleus | $G^{0\nu}$ ($10^{-15}$ yr$^{-1}$) | $\lvert M^{0\nu}\rvert$ |
|---|---|---|
| $^{48}$Ca | 24.7 | 0.9-3.0 |
| $^{76}$Ge | 2.8 | 2.8-6.2 |
| $^{82}$Se | 10.1 | 2.6-5.4 |
| $^{96}$Zr | 20.5 | 1.8-6.5 |
| $^{100}$Mo | 15.8 | 3.9-7.22 |
| $^{116}$Cd | 16.6 | 3.2-5.5 |
| $^{130}$Te | 14.2 | 2.7-6.4 |
| $^{136}$Xe | 14.5 | 2.2-4.8 |
| $^{150}$Nd | 61.9 | 1.7-5.6 |

- Isotopic abundance and possibility of enrichment

### 2.2.1 Isotope screening

The selection of the isotope of interest is critical for the development of a viable $0\nu2\beta$ decay experiment. Taking into account the calculations of nuclear matrix elements and the phase-space factor, it would be rational to choose the isotope with the highest rate. Other important constraints have to be taken into account, considering the technique and the cost of an experiment: bigger isotopic abundance and available enrichment technology are important for building an experiment. Also, the transition energy is significant: in a calorimetric approach the true signal can be suppressed by the background, so the isotopes with a $Q_{\beta\beta}$ close to some natural radioactivity lines should be avoided. The Tab. 2.2 presents the most suitable isotopes for neutrinoless double beta decay searches. Also these isotopes have been experimentally observed to undergo two-neutrino double beta decay.

### 2.2.2 Background

The background level in the region of interest is a crucial factor for sensitivity of a $0\nu2\beta$ experiment. If the background index is so small that the total number of background counts is $\ll 1$ ("zero-background" condition) for a given exposure of a real experiment, experimental sensitivity become to be proportional to the detector mass and the time of measurement:

$$T_{1/2}^{0\nu2\beta} \propto \frac{a \cdot \epsilon \cdot M \cdot t}{\lim S} \tag{2.14}$$

where $\lim S$ is an excluded number of events, that in a case of zero background is given by $\lim S = 2.44$ at 90% confidence level [56].

Achieving the "zero-background" level will considerably increase the sensitivity without changes on the scale of the experiment. For this

TABLE 2.2: Isotopic abundance and Q-value for experimentally studied $2\nu2\beta$ emitters.

| Isotope | Isotopic abundance (%) | $Q_{\beta\beta}$ (keV) |
|---|---|---|
| $^{48}$Ca | 0.2 | 4263 |
| $^{76}$Ge | 7.8 | 2039 |
| $^{82}$Se | 9.2 | 2998 |
| $^{96}$Zr | 2.8 | 3348 |
| $^{100}$Mo | 9.6 | 3035 |
| $^{116}$Cd | 7.6 | 2813 |
| $^{128}$Te | 31.7 | 867 |
| $^{130}$Te | 34.1 | 2527 |
| $^{130}$Ba | 0.1 | 2611 |
| $^{136}$Xe | 8.9 | 2459 |
| $^{150}$Nd | 5.6 | 3371 |
| $^{238}$U | 99.3 | 1150 |

reason, current experiments are putting significant efforts on the background suppression.

### Natural radioactivity

One of the most significant background components is the natural radioactivity of the detector components. The $^{238}$U and $^{232}$Th chains are providing the most common source of environmental radioactivity (see Fig. 2.5). For the $\gamma$–$\beta$ decays the highest energy line is the 2615 keV of $^{208}$Tl from the $^{232}$Th apart from weak lines with a very small branching ratio. If the transition energy for $0\nu2\beta$ decay is higher than this value, the background index in the region of interest will be much lower, than for searches with $Q_{\beta\beta}$<2615 keV.

Some challenging contributions from natural radioactivity can be discarded, using delayed signal coincidences. Some $\gamma$–$\beta$ decays are followed by an $\alpha$ emission: for example, $^{214}$Bi $\gamma$–$\beta$ decay is followed by an $\alpha$ decay of $^{214}$Po with the lifetime of 0.163 ms. However, in any case a careful selection of detector materials is required to reduce the background index.

The radiopurity of the detectors can be divided into three categories: internal radioactivity, external radioactivity, and surface contamination. The selection of materials is a crucial point for rare events search, starting from the source purification. Monitoring of radiopurity of elements, used for detector construction and surrounding the detector volume is required. Clean environment conditions (clean room, radon-free air), surface treatment (etching) allow to avoid or decrease the surface contamination.

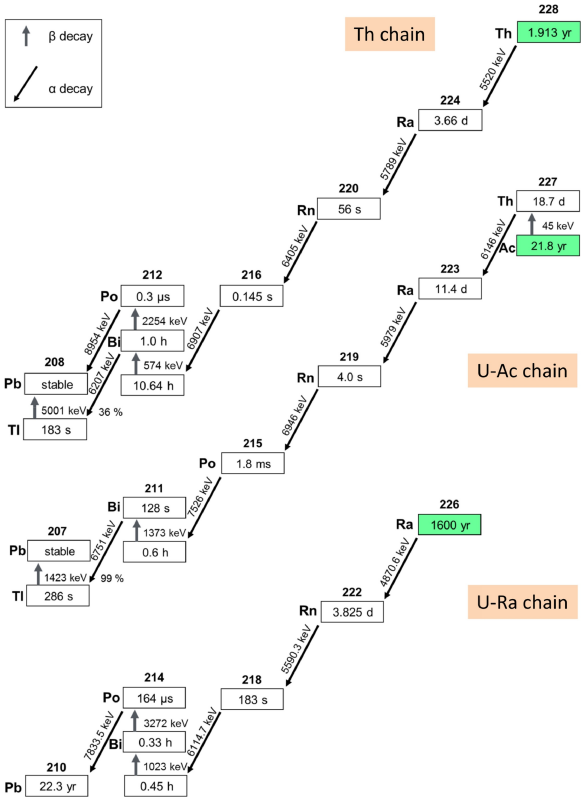


FIGURE 2.5: The three natural decay chains. Energies, half-lives and branching ratios are given.

### Cosmic muons

The flux of cosmic muons on the Earth surface is giving a significant contribution to the measured spectrum: it is 1 muon/cm$^2$/minute, with a mean energy at several GeV. If the experiment is running in the underground laboratory, the muon flux rate can be reduced to $10^{-7}$-$10^{-10}$ muon/cm$^2$/sec, depending on laboratory depth [57]. Active muon veto would exclude remaining muons and radioactivity from secondary interactions.

### Cosmogenic activation

The production of long-living nuclei in the detector materials is also possible by cosmogenic activation: mainly cosmogenic isotopes are produced by the bombardment of nuclei with high energy nucleons (neutrons are dominating at the Earth surface, protons and neutrons at high altitudes).

The cosmogenic activation can be controlled by use of shields on the surface or stocking materials underground. Also, any shipment of detector components by flight should be avoided.

The production rate for materials, commonly used in rare-decay searches, was estimated in [58].

### Pile-ups in the detectors

For the detectors with slow signals, the random coincidences on events with sum energy close to $Q_{\beta\beta}$ are dangerous. Even if events pile-ups from natural contamination are negligible, the $2\nu2\beta$ events are always present as an irreducible background. If the two $2\nu2\beta$ signals are produced within the time of detector response, such event can populate the region of interest.

With a high energy resolution (<1%) the contribution of $2\nu2\beta$ decay to the region of interest with the sensitivity to $m_{\beta\beta}$ in the inverted hierarchy region can be neglected [59].

## 2.2.3 Energy resolution

Energy resolution is a crucial factor for observation of neutrinoless double beta decay, as it allows to observe a sharp peak over a flat background (see Fig. 2.6) and it is a crucial factor in distinguishing it from the tail of the $2\nu2\beta$ spectrum, which is an irreducible background for any experimental search for $0\nu2\beta$.

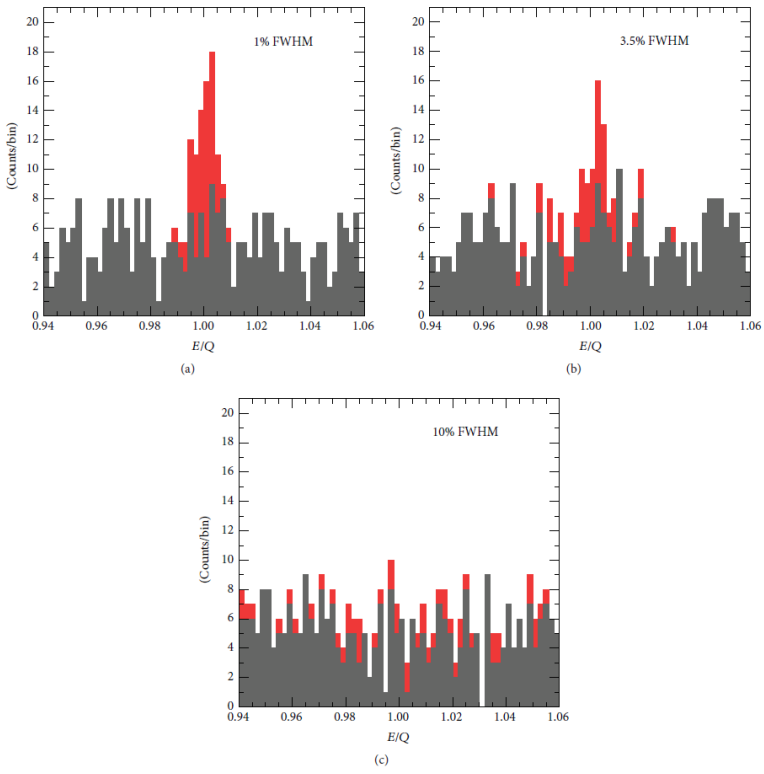


FIGURE 2.6: Signal and background (red and grey histograms, respectively) in the region of interest around $Q_{\beta\beta}$ for three Monte Carlo experiments with the same signal strength (50 counts) and background rate (1 count/keV), but different energy resolution (a: 1% FWHM; b: 3.5% FWHM; c: 10% FWHM) [60].

### 2.2.4 Sensitivity of a $0\nu2\beta$ experiment

In case of $0\nu2\beta$ decay peak observation in the energy spectrum, the half-life can be evaluated as:

$$T^{0\nu}_{1/2} = ln(2) \cdot t \cdot \epsilon \cdot \frac{N_{\beta\beta}}{N_{peak}} \tag{2.15}$$

where $t$ is the time of measurement, $\epsilon$ is the detection efficiency, $N_{\beta\beta}$ is the number of $\beta\beta$ isotope nuclei, and $N_{peak}$ is the number of observed events at $Q_{\beta\beta}$.

TABLE 2.3: $1\sigma$ ranges both for Gaussian and Poisson distributions for two different values of $N_{peak}$.

| Distribution | $N_{peak}$ | Range | Relative error (%) |
|---|---|---|---|
| Gauss | 5 | 2.8-7.2 | 44.7 |
| | 20 | 15.5-24.5 | 22.4 |
| Poisson | 5 | 3.1-7.6 | 45.0 |
| | 20 | 15.8-24.8 | 22.5 |

Due to the expected small amount of events, we use Poisson distribution for $N_{peak}$. Assuming the confidence interval at $1\sigma$, in the Tab. 2.3 we show them both for Poisson and Gauss distribution with two values for $N_{peak}$: 5 and 20.

If no peak is detected, the sensitivity is defined as the half-life of $0\nu2\beta$ decay corresponding to the maximum signal that could be hidden by the background fluctuations:

$$S^{0\nu} = ln2 \cdot \epsilon \cdot \frac{1}{n_\sigma} \cdot \frac{x\eta N_A}{M_A} \cdot \sqrt{\frac{M \cdot t}{b \cdot \Delta E}} \tag{2.16}$$

Where $b$ is the background level per unit mass/energy/time, $M$ is the detector mass, $\Delta E$ is the FWHM energy resolution, $x$ is the stoichiometric multiplicity of the element containing the $2\beta$ candidate, $\eta$ is the $2\beta$ candidate isotopic abundance, $n_\sigma$ is the confidence level, $N_A$ is the Avogadro constant, and $M_A$ is the atomic weight of the $2\beta$ isotope. This approach works well for the Gaussian limit of Poisson statistics, but for "zero-background" experiments other approach is required. For low background experiment with exposure $M \times t$ the expected number of $0\nu2\beta$ events is:

$$N_{exp} = ln(2) \cdot \frac{N_A}{M_A} \cdot \epsilon \cdot \frac{M \cdot t}{T^{0\nu2\beta}_{1/2}} \tag{2.17}$$

If there are several identical experiments with the same total exposure, they would observe a different number of events in the region of interest ($N_{obs}$), with the expectation value $\mu = N_{exp}$. The probability

distribution function of $N_{obs}$ can be described by a Poisson distribution:

$$Po(N_{obs};\mu) = \frac{\mu^n}{n!}e^{-\mu} \tag{2.18}$$

For large number of identical experiments, the observed value will coincide with expectation value only in part of cases. For example, for $\mu$=5, only in 17.5% of experiments $N_{obs}$=5. From an experimental point of view, with the observed $N_{obs}$ value, an information on true value of $\mu$ is required. In this case the confidence limits are considered: the upper and lower limits, $\mu_{up}$, $\mu_{low}$ are defined as the values of parameter $\mu$. For a large amount of experiments following the Poisson distribution $Po(N_{obs};\mu_{low})$, $Po(N_{obs};\mu_{up})$, only a small fraction $\alpha(\beta)$ of total number will yield a number larger (or smaller) than $N_{obs}$:

$$\alpha = \sum_{N_{obs}}^{\infty} Po(n;\mu_{low}) \tag{2.19}$$

$$\beta = \sum_{0}^{N_{obs}} Po(n;\mu_{up}) \tag{2.20}$$

In case of $N_{obs}$=0, only an upper limit $\mu_{up}$ can be evaluated. From Eq. 2.20, $\mu_{up} = -log(\beta)$. For CL at 90% ($\beta$=0.1) $\mu_{up} \approx 2.3$, and for 95% ($\beta$=0.05) $\mu_{up} \approx 3$. This means that in a Poisson distribution, with expectation value at 2.3, experiment would observe 0 events 10% of the time. Then, for experiments, which report a negative result, sensitivity is defined as the average upper limit from an ensemble of experiments with the expected background and no true signal. This simple approach works for ideal experiments with the expected background $b = 0$, while in more realistic case this method collapses: for small amount of observed events with expected background counts>0, the calculated $\mu_{up}$ value can be below zero, which is an absurd result:

$$\beta = \sum_{0}^{N_{obs}} Po(n;\mu_{up}+b) = \sum_{0}^{N_{obs}} \frac{(\mu_{up}+b)^n}{n!}e^{-(\mu_{up}+b)} \tag{2.21}$$

For example, if $b = 5$, for $N_{obs} = 1{,}0$, we obtain $\mu_{up} = -0.25{,}-2$. This collapse of classical limit was solved by G. Felman and R. Cousins [56]. They have introduced a method for the construction of confidence belts using an ordering principle based on likelihood ratios. This procedure unifies the treatment of upper confidence limits for both null results and two-sided confidence limits.

With this approach, the sensitivity calculation in presence of low background and no true signal is computed as an average upper limit that would be obtained by an ensemble of identical replicas of such an experiment, each one with the same mean expected background and no true signal. A function $U(n|b)$ is yielding the upper limit for a given observation $n$ and a mean predicted background level $b$. Values for $U(n|b)$ are reported in [56] for classical CL values: 68%, 90%, 95% and

99%. Then the sensitivity $S(b)$:

$$S(b) = \sum_{n=0}^{\infty} Po(n|b)U(n|b) \tag{2.22}$$

the sensitivity $S(b)$ of an experiment expecting $b$ events of background is obtained by averaging the upper limits obtained using the unifi

ed approach $U(n|b)$ with the likelihood of the individual observations $Po(n|b)$ [61]. As shown in Fig. 2.7, the difference between the sensitivity $S(b)$ and $U(b|b)$ is very small but notable for any $b$ value.

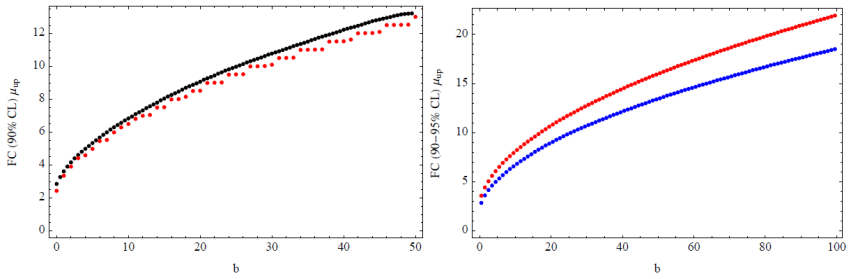


FIGURE 2.7: Left: 90% CL sensitivity curve as a function of mean background prediction b (black dots) or by simply assuming n = b (red dots). Right: sensitivity curve as a function of b for 90% and 95% CL[61].

## 2.3 Current generation experiments

Search for double beta decay requires special techniques for the investigation of such a rare process. There are two basic types of experimental methods: calorimetric and tracko-calo detectors. In calorimetric experiments the "detector=source" approach is used, which allows to provide very high detection efficiency: about 70-90% up to FWHM=0.1% at $Q_{\beta\beta}$. In tracko-calo experiments, the source is separated from the detectors. This method allows to reconstruct the complete track of the emitted electrons from the source and to measure and identify background components, but disadvantages of this method are lower efficiency and energy resolution. In the Tab. 2.4 the current experiments on different isotopes are listed together with the strongest limits on $m_{\beta\beta}$. As one can see, the current generation of experiments is only approaching the inverted hierarchy region, where $m_{\beta\beta}$ is less than 0.05 eV. In next years the community searching for $0\nu2\beta$ will focus on several of the most promising isotopes, uniting efforts to perform ton-scale experiments, which can fully investigate the inverted hierarchy region. The overview of the most sensitive experiments of the current generation is following.

TABLE 2.4: In this table, the main results on $0\nu2\beta$ isotopes with past and present experiments are listed.

| Isotope | $Q_{\beta\beta}$, keV | Experiments | Best limit on the half-life | $m_{\beta\beta}$, eV | Reference |
|---|---|---|---|---|---|
| $^{48}$Ca | 4271 | NEMO-3 | $5.8\times10^{22}$ | 3.1-15.4 | [62] |
| $^{76}$Ge | 2039 | GERDA, Majorana | $8\times10^{25}$ | 0.1-0.26 | [63] |
| $^{82}$Se | 2995 | NEMO-3, CUPID-0 | $2.4\times10^{24}$ | 0.4-0.8 | [64] |
| $^{96}$Zr | 3350 | NEMO-3 | $9.2\times10^{21}$ | 7.2-19.5 | [62] |
| $^{100}$Mo | 3034 | NEMO-3, CUPID-Mo | $1.1\times10^{24}$ | 0.3-0.6 | [62] |
| $^{116}$Cd | 2802 | Aurora | $2.4\times10^{23}$ | 1.1-1.6 | [65] |
| $^{130}$Te | 2533 | CUORE | $1.5\times10^{25}$ | 0.1-0.5 | [66] |
| $^{136}$Xe | 2479 | KamLAND-Zen, EXO-200 | $1.1\times10^{26}$ | 0.1-0.2 | [67] |
| $^{150}$Nd | 3667 | NEMO-3 | $2.0\times10^{22}$ | 1.6-5.3 | [62] |

### 2.3.1 $^{76}$Ge experiments

The isotope $^{76}$Ge is a candidate for $0\nu2\beta$ decay search with a transition energy $Q_{\beta\beta}$=2039 keV, which is relatively low. Therefore germanium experiments are very sensitive to natural background radioactivity, such as $\gamma$-rays from $^{208}$Tl, cosmogenic, potassium contamination and others. The ultrapure Germanium semiconductor diodes (see Fig. 2.8) are very well-known detectors, can be manufactured in a large amount with masses of kg range. An outstanding energy resolution in the region of interest can be obtained at liquid nitrogen temperature: typical good energy resolution is of the order of 0.2% FWHM at 2 MeV.

#### GERDA

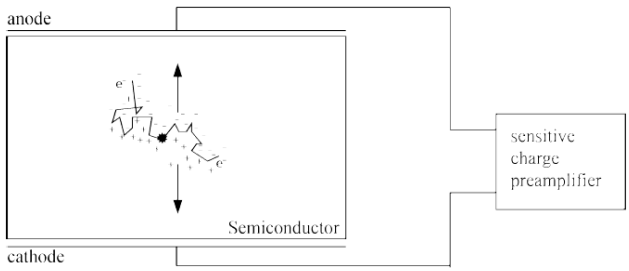


FIGURE 2.8: In semiconducting calorimeter the ionizing radiation is measured by the number of charge carriers produced in the detector material which is arranged between two electrodes. The number of e-h pairs is proportional to the energy deposit.

The GERmanium Detector Array (GERDA) experiment was proposed in 2004 and started data taking in 2011. This facility uses bare high-purity Germanium diodes, directly immersed in a liquid argon bath, which works as cooling liquid and active shield against external gammas. The cryostat contains about 100 tons of liquid Argon.

The detectors are arranged in several strings. The holders are made of ultra-pure copper and PTFE, with the aim to reduce the amount of any extra materials as much as possible. The LAr cryostat is placed in a water tank, which works as a Cherenkov muon veto (with PMTs for light collection), and due to big volume (590 $m^3$), it also serves as an external radiation shield. The detector system is shown in Fig. 2.9.

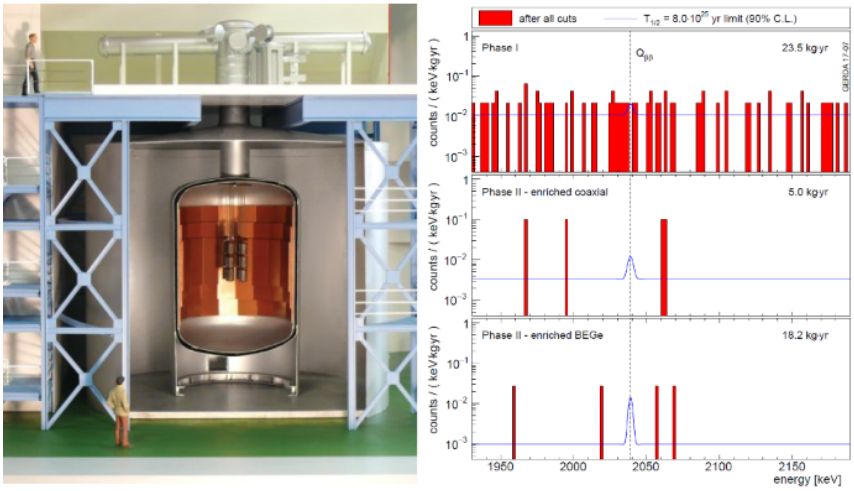


FIGURE 2.9: Scheme of GERDA experiment(left) and results of GERDA phase I+II (right).

The $0\nu2\beta$ signal is supposed to provide an energy deposit, localized in a small volume due to the short electron range in Ge. The background $\gamma$-ray signals, which mostly undergo multiple Compton scattering, are separated by $\approx 1$ cm in germanium. They can be rejected by efficient pulse-shape discrimination in BGE (Broad Energy Germanium) detectors, thanks to electric field configuration inside the detector volume: the pulse-shape discrimination (PSD) parameter is based on the ratio between the maximum amplitude of the signal and the total energy. This parameter allows rejecting more than 90 % multi-site events and practically all surface $\alpha - \beta$ events.

The GERDA experiment data taking is divided into two stages. Phase I was performed from November 2011 to March 2013 with semi-coaxial HPGe detectors, that were used previously in Heidelberg-Moscow and IGEX experiments (enriched to 86% in $^{76}$Ge), plus natural crystals from the GENIUS-TF project, with the total mass of 17.7 kg. Resulting from the first phase, a measurement of $2\nu2\beta$ and a limit on $0\nu2\beta$ decay half-life ($T^{0\nu}_{1/2} > 2.1 \times 10^{25}$ yr) were obtained with 17.9 kg yr of exposure.

In Phase II the active mass was increased by about 20 kg and the detector setup was refurbished with the goal to reduce the background. Recently obtained limit on sensitivity on $0\nu2\beta$ decay half-life is $5.8{\times}10^{25}$ yr. With the last dataset the background index of BEGe detectors with exposure of 30.8 kg$\times$yr is $0.6^{+0.4}_{-0.2} \times 10^{-3}$ counts/keV/kg/yr.

This is an outstanding result, given the $Q_{\beta\beta}$ at 2 MeV. With such low background the experiment can be considered "zero-background". The full exposure is expected to be 100 kg×yr with the sensitivity $\approx 1.4\times10^{26}$ yr. The phase II is supposed to be finished in 2019 [63].

#### Majorana

The Majorana Demonstrator is located in the Sanford Underground Research Facility, South Dakota. 58 high-purity Ge detectors of P-type, point-contact (PPC) are used for the experiment with a total mass of 44.1 kg. 35 modules are fabricated out of enriched Ge (88% of $^{76}$Ge, 29.7 kg), and the remaining 23 are made of 14.4 kg of natural Ge (7.8 % of $^{76}$Ge). This experiment also working with the PSD parameter to reject multi-site events, but for a case of surface $\alpha$'s there is used the lithiated dead layer, covering the detectors surfaces. Also, the delayed charge recovery parameter is used to identify $\alpha$ events in the detector volume. The operation of Majorana experiment started in 2015, and with the exposure of 26 kg×yr of $^{76}$Ge the obtained sensitivity is $T^{0\nu}_{1/2} > 2.7 \times 10^{25}$ yr with background index at $1.54\pm2.0 \times10^{-1}$counts/FWHM/kg/yr [68], [69].

### 2.3.2 $^{136}$Xe experiments

Due to chemical properties of $^{136}$Xe, this isotope can be studied in liquid scintillator detector or Time Projection Chamber (TPC). The main advantage of such types of detectors is the possibility to build a detector with active mass bigger than for any other type of detector. Such experiments can exploit the facilities which were first designed for neutrino oscillation measurements and are already meeting the requirements for the double beta decay experiments: low background, high detector efficiency. The main disadvantage of $^{136}$Xe experiments is low energy resolution with respect to other $0\nu2\beta$ decay searches. The transition energy $Q_{\beta\beta}$ of $^{136}$Xe is 2459 keV, which is lower than endpoint of natural $\gamma$ radioactivity, the background in the region of interest influences the sensitivity and require careful analysis.

#### Kamland-Zen

Kamland-Zen experiment exploits the KamLAND infrastructure and the detector volume which were previously used for neutrino oscillations detection. A balloon filled with 13 tons of Xe-loaded scintillator (Xe-LS) was suspended inside the outer balloon, filled with 1 kton of liquid scintillator (see Fig. 2.10). Another layer of protection is the 3.2 kton water Cherenkov detector. The scintillation light is collected by 1,879 photomultiplier tubes (PMTs). In the Xe-LS there is 3% of xenon by weight, and xenon was enriched to 91 % of $^{136}$Xe (and 9% of $^{134}$Xe). The total mass of added Xe is around 300 kg. Two phases of measurements were performed, with significant improvement of the background in the

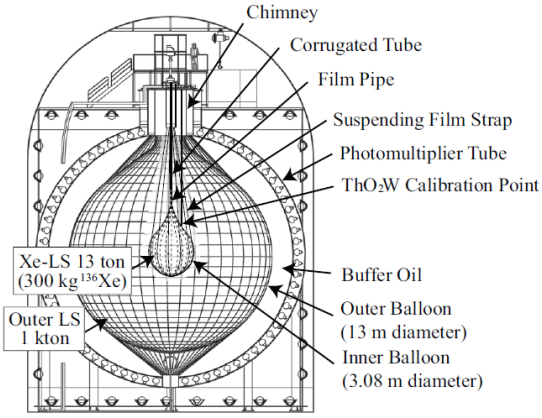


FIGURE 2.10: A scheme of Kamland-Zen detector.

phase II thanks to the purification of Xe-LS. The calibration and energy scale studies were performed using $^{60}$Co, $^{68}$Ge and $^{137}$Cs sources. The energy resolution is $\sigma \approx 7.3\%/\sqrt{E(MeV)}$. Series of cuts were applied to reject the background: muons and any events within 2 ms of delay are removed, the reconstructed vertex of an event must be within 2 m of the detector center, the Bi-Po events are rejected using delayed coincidence tag.

The obtained limits on the combined phase I and phase II results are giving the strongest current upper limit on $m_{\beta\beta} < 61 - 165$ meV, which corresponds to the lowerr limit for the $0\nu2\beta$ decay half-life of $T^{0\nu}_{1/2} > 1.07 \times 10^{26}$ yr [67]. The KamLAND-Zen experiment is planned to be upgraded with reduction of the backgrounds and increased mass of 800 kg of enriched Xe. The sensitivity of this experiment is limited by the energy resolution, but it is compensated by its big mass scale.

### EXO-200

EXO-200 is another experiment, searching for $0\nu2\beta$ in $^{136}$Xe. It is located at the Waste Isolation Plant Project (WIPP) in New Mexico, USA. The detector consists of a time-projection chamber (TPC), filled with liquid xenon (enriched to 81% of $^{136}$Xe). This cylindrical chamber is split into two drift regions by a common cathode. A simple scheme of the detector is shown in Fig. 2.11. The two types of signals are collected simultaneously: scintillation light (read by avalanche photodiodes) and ionization charge (read after being drifted to crossed-wire panels at each anode). Using the signals from wire panels, the event vertex position is reconstructed in the x-y plane, and the delay between prompt light and the delayed charge signal allows to reconstruct the z position. The data-taking started in 2011 and was stopped in 2014 (phase I). Due to an accident at WIPP, phase II started only in 2016 with several improvements (electric field increase, reduction of radon level, new electronics). Average energy resolution in phase II is 1.2%.

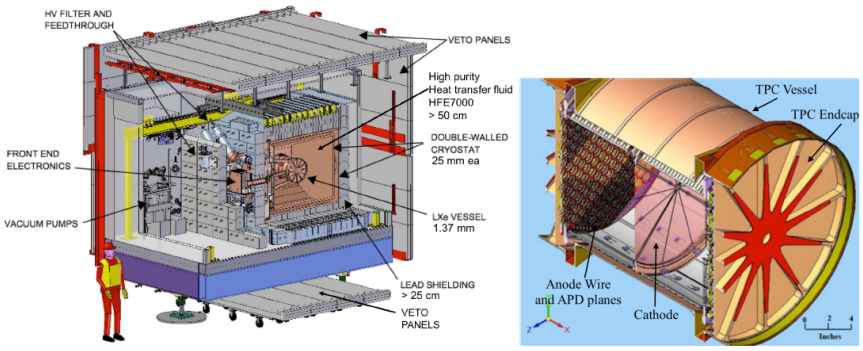


FIGURE 2.11: Cutaway view of the EXO-200 full set-up with the main components identified (left), and a cutaway view of the time projection chamber (right).

With the total exposure of 177.6 kg×yr of $^{136}$Xe a limit on the half-life of $T_{1/2} > 1.8 \times 10^{25}$ yr was obtained [70].

### 2.3.3 $^{130}$Te

The $^{130}$Te isotope has the biggest natural abundance (34%) among $2\beta$-active nucleus, giving a possibility to perform an experiment with big mass without enrichment. This isotope was one of the first to be studied regarding double beta decay. The transition energy is 2.5 MeV, which increases possible background in the ROI and requires special attention to the radiopurity of the detector components.

#### CUORE

The Cryogenic Underground Observatory for Rare Events (CUORE) is searching for the decay of $^{130}$Te using natural $TeO_2$ crystal bolometers. The CUORE Collaboration developed the detector prototypes and demonstrator in Cuoricino [71] and CUORE-0 experiments [72]. CUORE is the first ton-scale cryogenic bolometric experiment, started operation in 2017. The bolometric technique (it will be described in details in Chapter 3) requires to cool down the detectors to very low temperatures (10-20 mK) so that when crystal absorbs energy, it can be measured as a change of the temperature. The cryostat inner shielding is made of radiopure copper, and 6 tons Roman lead shield is covering the experimental volume on top (see Fig. 2.12). CUORE is currently operating 988 $TeO_2$ crystals (each module is 5×5×5 cm$^3$ and 750 g of weight) with NTD sensors. The array structure of the detectors allows to perform anti-coincidence selection (rejection of events in different bolometers within the coincidence window).

With the combined exposure of Cuoricino+CUORE-0+CUORE of 44 kg×yr of $^{130}$Te, the strongest limit on the $^{130}$Te half-life is obtained: $T^{0\nu}_{1/2} > 1.5 \times 10^{25}$ yr [66]. CUORE data-taking is ongoing.

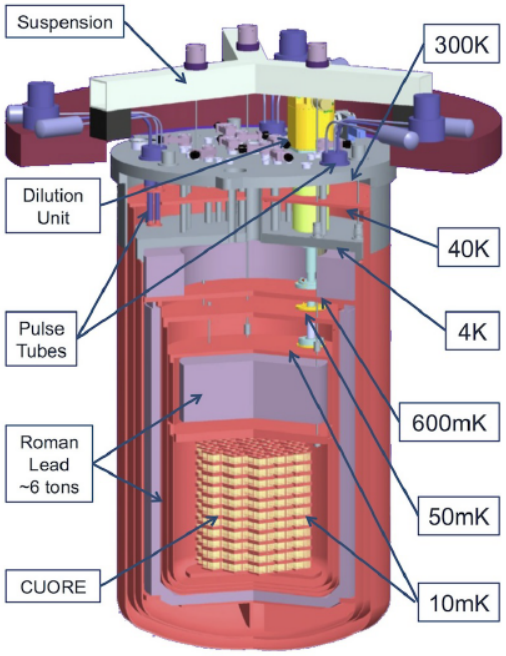


FIGURE 2.12: Cutaway view of the CUORE cryostat

### SNO+

SNO+ is an experiment, investigating double beta decay in $^{130}$Te at SNOLAB. The infrastructure mostly was developed for SNO neutrino experiment with heavy water. Now the detection medium was converted to liquid scintillator, loaded with 0.5 % of natural Te (260 kg of $^{130}$Te in the first phase). The acrylic vessel with scintillator is surrounded by almost 9,500 photomultiplier tubes (see Fig. 2.13). The external shielding consists of 5300 tonnes of water, and it acts also as muon veto (monitored by 92 PMTs). A dedicated plant for production of radiopure liquid scintillator was developed [73]. Tellurium will be dissolved in the form of a Te-butanediol complex. The purification of Telluric acid will be performed underground. The Te loading is planned to be performed in spring 2019. The projected sensitivity of the fist phase to $0\nu2\beta$ decay half-life of $^{130}$Te in 5 years of measurement is $\approx 2\times10^{26}$ yr. A possible second phase with bigger mass (1% or more of loaded Te) will aim to reach sensitivity to the half-life at $1\times10^{27}$ yr, which corresponds to full investigation of inverted mass hierarchy [74].

## 2.3.4 $^{100}$Mo

The $^{100}$Mo isotope has favorable theoretical predictions, a high transition energy (3034 keV), a possibility of enrichment in a large scale with gas centrifugation. The CUPID-Mo project, investigating this isotope

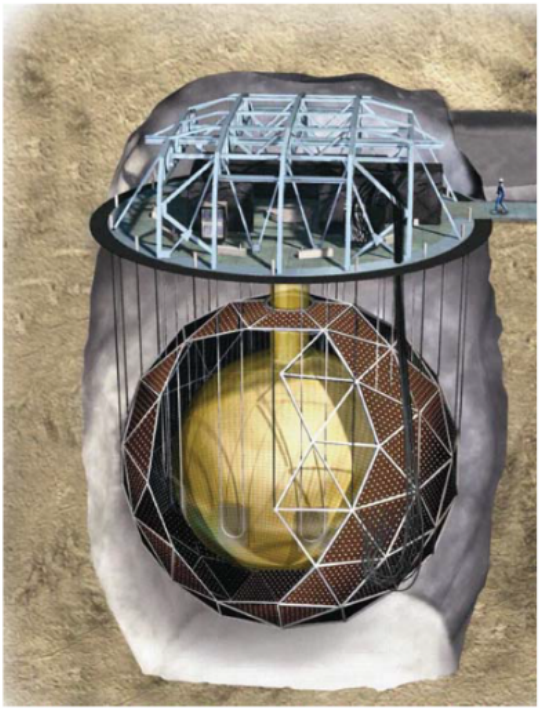

FIGURE 2.13: Cutaway view of the SNO+ detector.

with scintillating bolometers technique, is the main topic of this thesis and will be described in next chapters.

### NEMO-3

NEMO-3 is a traco-calorimetric experiment, which was investigating different isotopes starting from 2003 to 2011. The detector consists of three main components: the source (thin foil containing the isotope of interest and copper), the tracker made of wire cells, operating in Geiger mode (the readout of signal arrival time allows full 3D-reconstruction) and the calorimeter, made of scintillating blocks, readout by PMTs. The schematic view of the detector is shown in Fig. 2.14. NEMO-3 was composed of 20 identical sectors. Each sector was hosting different $2\beta$ sources, with the total mass of almost 10 kg. Three sectors were used for background measurements and were equipped with pure Cu foil and natural $TeO_2$. The majority of the detector, 12 sectors, were hosting 6.9 kg of $^{100}$Mo (purified). Other isotopes, investigated in the NEMO-3 detector, were: $^{82}$Se (932 g), $^{130}$Te (454 g), $^{116}$Cd (405 g), $^{150}$Nd (36.6 g), $^{96}$Zr (9.4 g), $^{48}$Ca (7.0 g).

The detector was surrounded by a solenoidal coil to obtain magnetic field of 25 Gauss inside the wire chamber in order to identify electrons and positrons by measuring the curvature of their tracks. The passive shielding was provided by 20 cm low-radioactivity iron and tanks filled with borated water to capture neutrons. In 2004 the radon-free air factory was installed to improve the background.

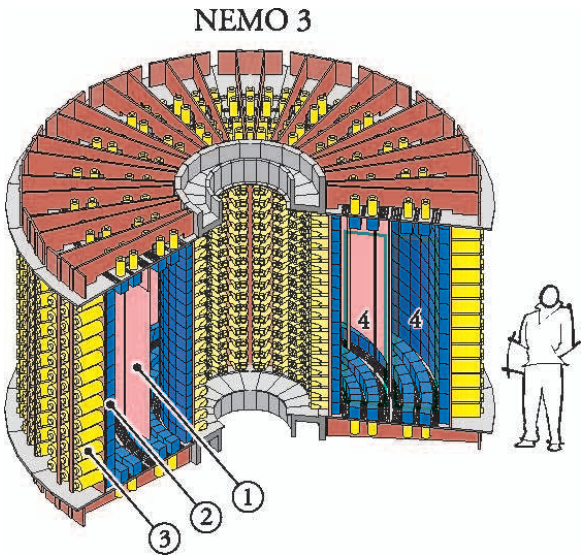


FIGURE 2.14: The NEMO-3 detector without shielding. 1 – source foil; 2– plastic scintillator; 3 – low radioactivity PMT; 4 – tracking chamber.

Thanks to traco-calo technique, the double beta decay events could be selected by common vertex and two electron tracks. Use of energy and time-of-flight cuts allows efficient rejection of any background type.

The $2\nu2\beta$ decay measurements were performed for seven isotopes, placed in the detector volume. For each isotope the energy spectrum (sum and single-electron) and the angular distributions were obtained. $2\nu2\beta$ decay rate was measured, but no evidence of $0\nu2\beta$ decay was found for all seven isotopes. The limits on the neutrinoless mode half-life were set. The limit for $^{100}$Mo isotope is the most stringent up-to-date: $T^{0\nu}_{1/2} > 1.1 \times 10^{24}$ [75].

## 2.4 Future DBD experiments

### 2.4.1 CUPID

CUPID (CUORE Upgrade with Particle IDentification) is a proposed ton-scale bolometric experiment with the goal to explore all the inverted hierarchy region of the neutrino mass pattern [76]. To observe the effect with high confidence (at least $3\sigma$) with the half-life at $10^{27} - 10^{28}$ yr, a set of technical requirements has to be fulfilled: the mass in the 100-1000 kg range, "zero background" in the ROI, the exposure $\approx$1 ton$\times$yr, high energy resolution (0.1%). The estimated sensitivity to $\langle m_{\beta\beta} \rangle$ is 7-20 eV for 10 years of measurement. The existing cryostat and infrastructure of CUORE experiment will be used. The detector technology will be improved to suppress background caused by surface contamination of the detectors by $\alpha$ and high energy $\beta$ active nuclides. Such a sensitivity goal requires usage of enriched crystals, active background

rejection, high radiopurity of the detector materials. Multiple R&D projects are ongoing to demonstrate possible options for the CUPID experiment [77]. There are valuable arguments to perform $0\nu2\beta$ decay experiments with several nuclei and $^{100}$Mo is one of the most promising candidates for such a measurement [78]. The CUPID-Mo ($Li_2{}^{100}MoO_4$ scintillating bolometers) and CUPID-0 (ZnSe scintillating bolometers) demonstrators are the subject of this thesis and will be described in following chapters.

### 2.4.2 LEGEND

LEGEND is a proposal for a ton-scale experiment, investigating the $^{76}$Ge isotope with point-contact high purity germanium detectors. It will use the experience from both GERDA and MAJORANA projects, combining best features of both experiments. LEGEND development will be divided into two phases, starting with LEGEND-200, operating up to 200 kg of Ge detectors. The first phase will be performed in LNGS (Italy), exploiting the existing infrastructure of GERDA experiment. The goal is to perform a "zero-background" measurement (0.6 counts/(FWHM×ton×yr) with an exposure of 1 ton×yr. The second phase, LEGEND-1000 would operate up to 1000 kg of Ge detectors in a new underground facility. The desired exposure is above 10 ton×yr, and the sensitivity goal for $0\nu2\beta$ decay half-life for $^{76}$Ge is up to $10^{28}$ yr. Numerous improvements will be applied in LEGEND with respect to current experiments, as the bigger mass of each detector module, better readout electronics, improved active shield, background reduction [79].

### 2.4.3 nEXO

nEXO experiment is the proposed follow-up of the EXO-200 experiment. The detector will contain five tons of liquid xenon enriched to 90% in $^{136}$Xe (see Fig. 2.15). The TPC technology, developed in EXO-200, will remain, but with several improvements: there will be no central cathode, to remove radioactivity from the center of the TPC. The passive lead shielding will be enclosed in a water tank instrumented by photomultipliers, working as a Cherenkov detector. New cold readout electronics is under development. The experiment will take place in a deeper underground lab (SNOLab or Jinping). The estimated sensitivity of nEXO experiment to $m_{\beta\beta}$ is at 5.7-17.7 meV [80].

### 2.4.4 SuperNEMO

SuperNEMO is the next phase of the NEMO-3 experiment, the only advanced traco-calo detector searching for neutrinoless double beta decay. The SuperNEMO module has a layered design: the thin foil, containing the isotope of interest, is sandwiched between two tracker modules and calorimeter walls. The structure of the modules is similar to NEMO-3: 2034 drift cells operated in Geiger mode, 520 scintillating blocks

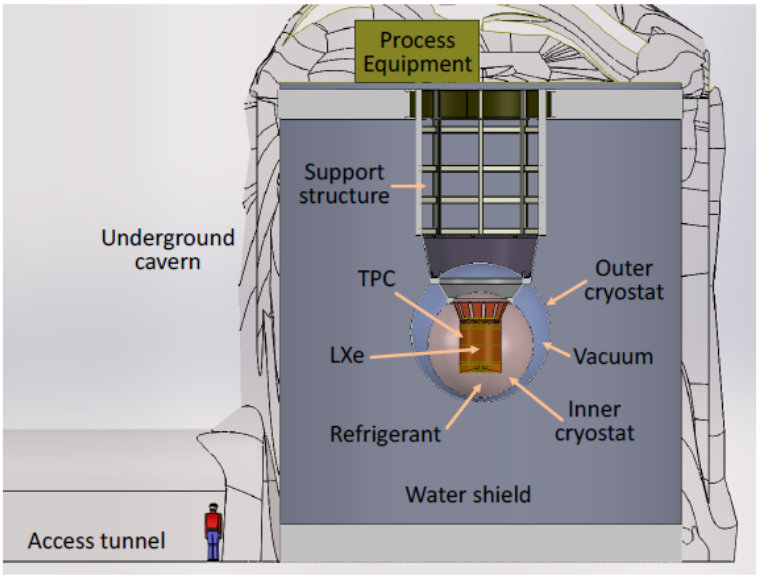


FIGURE 2.15: Engineering design rendering of the nEXO experiment concept

with PMTs. In the SuperNEMO experiment only one nucleus will be investigated, and the isotope of interest is $^{82}$Se. The preparation of the detector is ongoing in LSM (Laboratire Souterraine de Modane) underground laboratory [81].

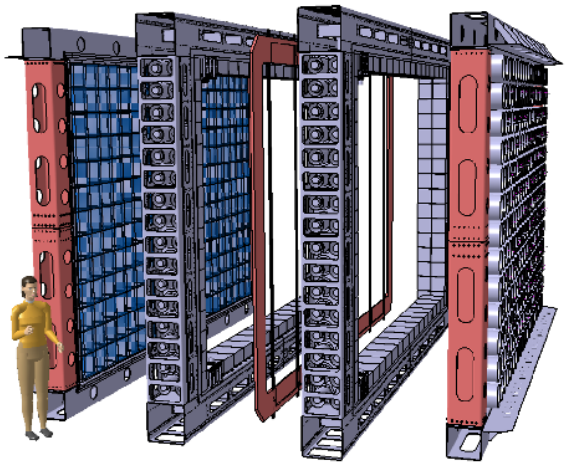

FIGURE 2.16: Expanded diagram of the SuperNEMO Demonstrator showing (from left to right) calorimeter wall, tracker, source foil frame, tracker, calorimeter wall.

## 2.5 Conclusions and perspectives

The neutrinoless double beta decay discovery would have great importance for particle physics. If it is observed, the neutrino nature will be established, opening a way to new physics models investigation.

Even though this process was theoretically described almost 80 years ago, $0\nu2\beta$ decay was never observed. The development of $0\nu2\beta$ experiments is ongoing with the investigation of new detector techniques and data analysis tools. The landscape of $0\nu2\beta$ decay investigation is given by the dependence of effective Majorana neutrino mass on the lightest neutrino mass: the inverted hierarchy region of neutrino masses will be the first sensitivity milestone (the required sensitivity to $m_{\beta\beta}$ is not achieved yet, but the current limit reaches the bottom of the quasi-degenerate neutrino mass region, see Fig. 2.17).

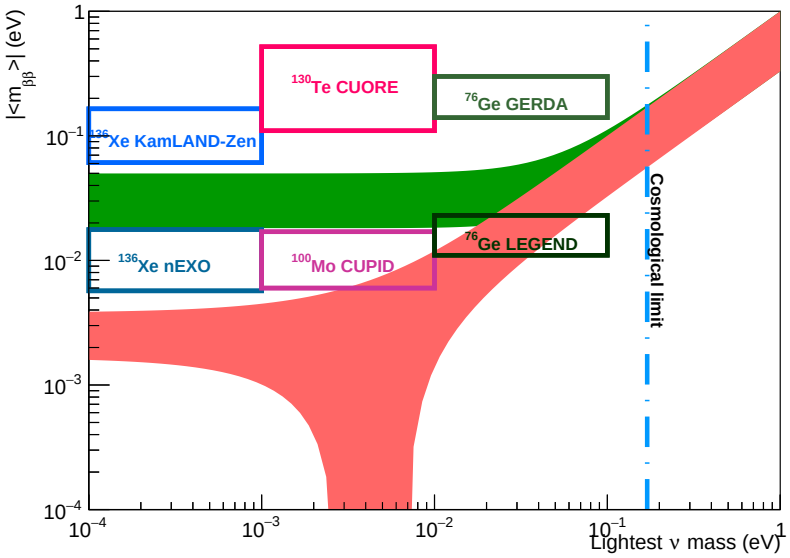


FIGURE 2.17: The effective Majorana mass as function of the lightesr neutrino mass, plotted using the lastest results on neutrino oscillation parameters (see Tab. 1.1). The constrain on the lightest neutrino mass from cosmological experiments is shown by a blue vertical line. Current limits on $m_{\beta\beta}$, achieved with $0\nu2\beta$ decay researches are shown (solid line) as well as prospects on sensitivity of future ton-scale experiments (dashed line). The limits on $m_{\beta\beta}$ are covering all scale of lightest neutrino mass, the boxes are used for better graphical representation.

The clues, favoring normal hierarchy, point out the necessity to unite

efforts on building ton-scale experiments with "zero-background" approach. The low-background detector technology was actively improving during the last decade, giving the possibility to perform next generation $0\nu2\beta$ decay experiments with very high sensitivity, approaching to the observation of this process.

# Chapter 3

# Scintillating bolometers

## 3.1 The bolometric technique

A promising experimental approach to study neutrinoless double beta decay is to use the bolometric technique. It offers excellent high energy resolution and extremely high efficiency, using the "detector=source" approach.

Large mass bolometers (with masses of the order of tens or hundreds of grams) are operated at temperatures below 20 mK, where the bolometer temperature changes are measurable even if induced by very small energy releases (of the order of keV or even less). One of the most important advantages of this kind of detectors is their heat conversion efficiency: almost all deposited energy is converted into phonons, while in other types signal is mediated by excitations which contain only a fraction of the total deposited energy.

In a simplified approach, the bolometer can be described with following components: energy absorber, phonon sensor, thermal link to the heat bath. A simple scheme is shown in Fig. 3.1.

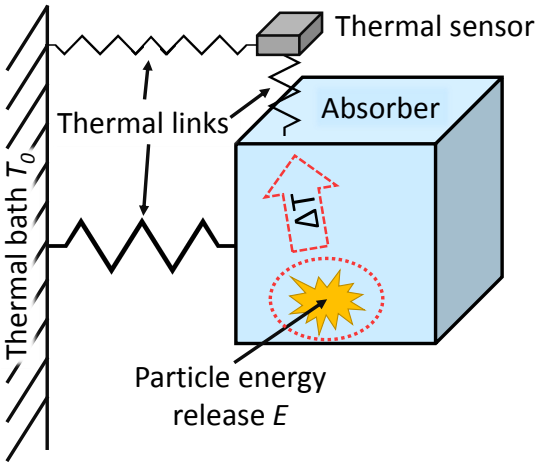


FIGURE 3.1: Scintillating bolometer scheme. The absorber is connected to the heat bath with a thermal link.

### 3.1.1 Absorber

Usually, the sensitive part of a bolometer is a single dielectric diamagnetic crystal. The energy, deposited in the absorber by a nuclear event, is measured through a temperature change (heat signal). After particle interacts in the absorber, the temperature increases by $\Delta T$, which is proportional to the deposited energy $E$:

$$\Delta T = \frac{E}{C} \tag{3.1}$$

where $C$ is the heat capacity of the detector. In an ideal calorimeter the signal will be produced by an instantaneous thermalization of the energy $E$, and the decay time constant will be:

$$\tau = \frac{C}{G} \tag{3.2}$$

where $G$ is the conductance of the thermal link.

To obtain a measurable signal amplitude, heat capacity should be relatively small. If absorber is a dielectric and diamagnetic crystal, the molar specific heat can be described by the Debye law:

$$C_r(T) = \frac{12\pi^4}{5} N_A k_b (\frac{T}{\Theta_D})^3 \tag{3.3}$$

where $\Theta_D$ is the Debye temperature that characterizes the crystal. Usually with dielectric crystals the heat capacity value, small enough for a bolometer operation can be reached at temperatures of 10-20 mK. Operation of such systems is a difficult task: they require complicated cooling systems, that can work for a long time with a stable temperature level (the description of cryostats operation principle can be found in Appendix A).

In proper conditions, such detectors can have excellent energy resolution. The intrinsic limit to the energy resolution for bolometers is given by thermodynamic fluctuations in the detector, due to random exchanges of phonons with the heat bath through the thermal link. The average energy of excitation is $\langle \epsilon \rangle \sim k_B T$, where $k_B$ is the Boltzmann constant. Then the energy $E = \langle \epsilon \rangle \cdot N = k_B T N$, where N is the number of phonons in the absorber. The internal energy of bolometer is $E = C(T) \cdot T$, and number of phonons is given by the heat capacity: $N = C(T)/k_B$. Then, the intrinsic RMS noise is given by the fluctuations of internal energy:

$$\Delta E_{int} = \sqrt{N} \cdot k_B T = \sqrt{k_B C(T) T^2} \tag{3.4}$$

As an example, a $Li_2MoO_4$ crystal would have intrinsic energy resolution of 2 eV at 10 mK. Of course, the energy resolution is affected by other noise sources and energy losses in the absorber. One of the challenges in bolometric experiments is reduction of vibrational and

microphonic noise. Typical energy resolutions of macrobolometers are of the order of few keV.

For the selection of an absorber, the heat capacity is a crucial parameter to get high and fast signals. For the $0\nu2\beta$ experiments with the proper choice of absorber compound, one can build a detector, which contains the source in its material. Also, the quality and cleanness of the crystal play a significant role: impurities can trap the e-h pairs and a part of the energy will be lost. In polycrystals, signals are position-dependent or have a slow response.

### 3.1.2 Thermistors

The thermal sensor is a device that converts temperature radiations into an electrical signal. There are several types of sensors that work at low temperatures:

- Neutron Transmutation Doped (NTD) Ge thermistors are critically doped semiconductors operated below the metal-insulator transition. They can be operated at a wide range of temperatures, but have relatively slow signals. The semiconducting element is usually glued at the absorber [82].

- Transition Edge Sensors (TES) are based on superconductivity phenomenon: they are operated at transition temperature $T_c$, where the resistance of the sensor changes significantly with the small variations of the temperature, resulting in a narrow range of operation ($T_c$ width). TES can be directly evaporated on the absorber surface, providing much faster response and sensitivity to athermal phonons than in case of gluing [83].

- Metallic Magnetic Calorimeters (MMC) are using materials with magnetization-temperature dependence. They have high energy resolution, fast signals, but MMC requires complicated read-out system based on SQUIDS [84].

Each type of sensors has its advantages and disadvantages. Since bolometers described in this work are based on the NTD thermistors, we will focus on their properties.

#### Neutron Transmutation Doped thermistors

This type of thermistors appears to be remarkably reproducible with excellent performance and high radiopurity [82]. Such feature is essential for the creation of large-scale experiment with big arrays of detectors.

NTDs are produced by irradiation of a pure natural Ge crystal with a flux of thermal neutrons. This process causes the production of dopants of Ga, As and Se.

The most important parameter, that characterizes the thermistor performance is the sensitivity:

$$A = |\frac{dlog(R(T))}{dlog(T)}| = \frac{T}{R}\frac{dR(T)}{dT} \tag{3.5}$$

The resistance of a semiconductor increases with the decreasing of impurities concentration, which can create energy levels or below the conductance band or above the valence band. Beyond a certain concentration level, named as Metal-Insulator Transition (MIT), the behavior of the doped sample becomes metallic independently of the temperature. For low dopant concentrations at low temperatures, the carriers are trapped in the valence band, and the semiconductor behaves as an insulator. In this case, at very low temperatures (T<10 K), the conduction is due to a quantum-mechanical tunneling effect through the potential barriers separating the dopant sites. This conduction regime is named Variable Range Hopping (VRH) and it is characterized by hopping processes mediated by phonons between two energetically separated sites. The resistance dependence is described in Eq.3.6. For NTDs $\gamma = 1/2$ [85].

$$R(T) = R_0 exp(\frac{T_0}{T})^{\gamma} \tag{3.6}$$

The NTD sensors are characterized by the parameters $T_0$ and $R_0$, and

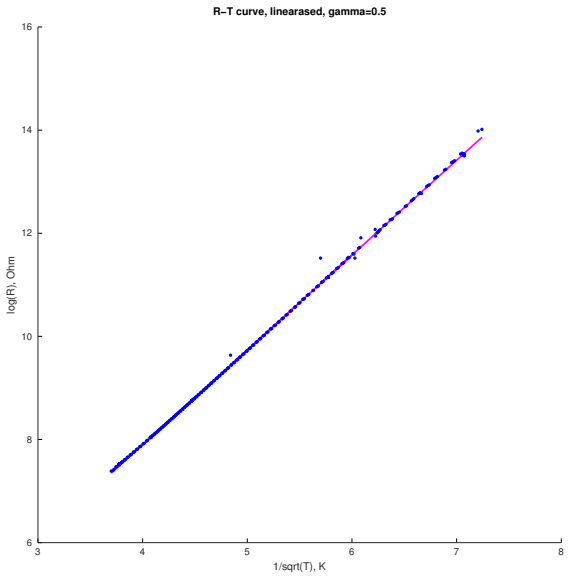


FIGURE 3.2: Typical dependence of NTD resistance on temperature (linearized). Values extracted from NTD R(T) characterization (for more details see Chapter 7).

these two parameters can be measured experimentally by fitting the exponential part of R-T dependence (see Fig.3.2). The NTD readout usually is done with fixed current, while the voltage change is registered as the signal.

## 3.2 Scintillating bolometers

The particle detection via scintillation light is one of the commonly used and old techniques in particle physics, regularly used as well as in liquid and solid detectors. In $0\nu2\beta$ decay search, scintillators are successfully used in tonne-scale experiments, as KamLAND-Zen (see Chapter 2).

Regarding the bolometer case, the crystal absorber, depending on the compound, can scintillate. It is possible to measure the produced light simultaneously with the heat signal with the help of a thin auxiliary bolometer facing the main crystal and working as a photodetector. The amplitude of the light signal from $\alpha$ particles is usually smaller than the one from a $\gamma/\beta$ interaction with the same energy and this difference allows to discriminate two particle bands (see Fig. 3.3)).

Scintillating bolometers, thanks to a proper choice of the compound on which they are based, can efficiently study isotopes with a $0\nu2\beta$ Q-value greater than 2.6 MeV, corresponding to the end-point of the bulk of natural $\gamma$ radioactivity. (This is the case for $^{100}$Mo - the isotope at the center of the proposed PhD subject - which has an energy transition of 3034 keV.) They would, therefore, take advantage of a significantly reduced background in the $0\nu2\beta$ decay signal region. Close-by sources or internal contamination can still produce events above 2.6 MeV, but this tiny component can be kept actively under control with a proper selection of radiopure materials. The dominant background is expected to be given by $\alpha$ particles which, however, can be rejected thanks to the different scintillation-to-heat ratio between $\alpha$ and $\beta$ particles. Detailed

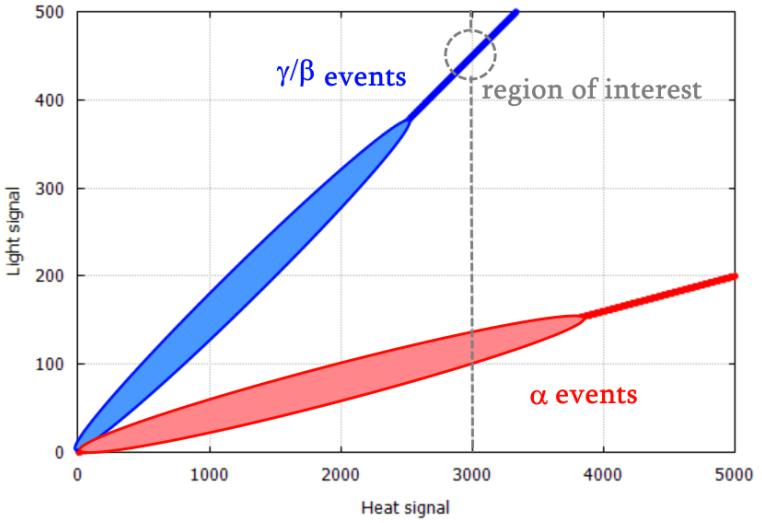


FIGURE 3.3: A schematic representation of a scatter plot: the red band represent $\alpha$ events and the blue band $\gamma/\beta$ events.

Monte Carlo simulations show that the most dangerous contaminant is $^{228}$Th. The internal contamination of the crystal with this isotope

must be less than 10 $\mu$Bq/kg in order to achieve a background index at the level of $10^{-4}$ counts/(keV×kg×yr) in the region of interest [86].

### 3.2.1 Scintillation mechanism

Scintillation in inorganic solids is a complicated physical process with several stages. The mechanism is triggered by absorbtion of a high-energy particle with the creation of inner shell hole and an electron. The electrons and holes are multiplied due to radiative decay (secondary X-rays), non-radiative decay (Auger process) and inelastic electron-electron scattering. The electrons and holes get thermalized when the electron energies are becoming less than the ionization threshold. As the position of the absorbtion and the final emission does not coincide, the energy migration to luminescence center occurs. In the final phase, the excited center of emission releases its energy with photon or through a non-radiative process.

The number of created electron-hole pairs depends on the initial absorbed energy $E_i$:

$$N_{e-h} = \frac{E_i}{E_{e-h}} \tag{3.7}$$

Where $E_{e-h}$ is the average energy of creation of electron-hole pair and it is related to the forbidden energy gap of the material. The scintillation light yield (characterizes efficiency of conversion of ionization energy to light output) is given by

$$LY(ph/MeV) = N_{e-h}SQ = \frac{E_i}{E_{e-h}}SQ \tag{3.8}$$

where $S$ is the efficiency of excitation transfer to luminescent center, and $Q$ is the quantum efficiency. $Q$ can be determined from the photo-luminescence studies, while $S$ is the least-known parameter and it depends on the material, temperature and any impurities in the crystal. On another hand, the light yield can be calculated using the information on the total energy ($E$) of the particle and the amount of light ($L$) produced by scintillation[1]

$$LY(keV/MeV) = \frac{dL}{dE} \tag{3.9}$$

The light yield of $\alpha$, protons, fast neutrons (e. g. particles which provide a high ionization density) is suppressed with respect to $\gamma/\beta$ particles (the most common case, for some particular compounds (e.g. ZnSe) it is the opposite, see Chapter 6). This difference can be explained by the fact that $\beta/\gamma$ particles release their energy in a bigger

[1]When discussing the performance of scintillating bolometers for double beta decay, the LY is often expressed in kev/MeV units, as these units reflect the deposition of heat signals of the order of MeV's (region of interest for $0\nu2\beta$ decay experiments is in 2-3 MeV range), while light signal for same events is of the order of keV's, depending on scintillation crystal properties.

volume, as the path is longer for the same energy. A semi-empirical formula was proposed to quantify this phenomenon [87]:

$$\frac{dL}{dr} = \frac{A_s \frac{dE}{dr}}{1 + kB\frac{dE}{dr}} \tag{3.10}$$

where $A_s$ is the absolute scintillation factor, $k$ is the quenching parameter and $B\frac{dE}{dr}$ is the density of excitation centers along the track. $kB$ is usually treated as a single parameter (Birks factor). For $\beta$ and $\alpha$ particles, the Eq. 3.10 can be approximated as follows:

$$LY_\alpha(E) \approx \frac{A_s}{kB}\frac{1}{dE/dr}, LY_\beta(E) \approx A_s \tag{3.11}$$

Then the quenching factor $QF$ can be defined as the ratio of light yields:

$$QF = \frac{LY_\alpha}{LY_\beta} \approx \frac{1}{kB(dE/dr)} \tag{3.12}$$

In this approximation, the quenching factor is considered not to depend on the energy, but in general case it is not true [88].

For scintillating crystals the quenching factor depends on many conditions:

- QF depends on impurities and defects in the crystal. In case if scintillator is doped, QF depends on kind and amount of dopant.
- Scintillation has several components with different amplitudes for different particles. Depending on the temperature, these amplitudes can change the QF.
- The signal acquisition should be performed in a proper time window. Otherwise, the part of signal amplitude can be lost, and QF will be miscalculated.

The scintillation properties strongly depend on the crystal quality, as well as the internal purity, the absence of defects, and the optical quality and transparency, which allows collecting the light signal without significant losses.

### 3.2.2 Light detectors

The light detectors, coupled to scintillating crystals, are also operated as bolometers. In this work, the thin Ge slabs with NTD sensors are used for light collection. Germanium-based bolometers are sensitive detectors in a wide range of photon energies, with high energy resolution. Germanium is known to be highly radiopure material, which is important for rare event searches.

The sensitivity of light detectors has to be high, as only a small fraction of particle energy is converted into scintillation photons, and

the light signals have energies of few keV. The typical sensitivity values are hundreds of nV/keV.

### 3.2.3 SiO coating

A way to significantly improve the light detector's performance is to increase the light collection by minimizing the reflected light. Such improvement can be obtained by using a special anti-reflective coating on the side of the light detector which is facing the scintillating bolometer.

One of the simplest ways to reduce the reflection is the so-called refraction index matching method. In the approximation of normally incident light from a transparent to an absorbing medium, the absorbed fraction can be calculated by the following formula:

$$R = \frac{(n_0 - n_1)^2 + k^2}{(n_0 + n_1)^2 + k^2} \tag{3.13}$$

where $n_0$ is the real refraction index of the transparent medium and $n_1$ ($k$) is the real (imaginary) part of the complex refraction index of the absorbing medium, i. e. germanium. If we consider a pure vacuum-germanium interface, the intensity of absorbed light is only 51%. If a thin coating layer with $n_i$ value between $n_0$ and $n_1$ is introduced between the two mediums, the Eq. 3.13 should be calculated first for the vacuum-coating, then for the coating-germanium transitions. The optimum value for $n_i$ of the anti-reflective material in case of germanium is $\approx 2.4$ which leads to a gain on the light absorbtion of the 35% with respect to bare germanium.

The best thickness for the layer can be determined by fulfilling the conditions for an optimal anti-reflective coating in the approach of the single-layer interference method. The coating thickness should be $d = \lambda/4$, where $\lambda$ is the wavelength of the incident light in the coating medium. This method works well for a distinct light wavelength of the source. In our case, we can take $\lambda$=630 nm. The optimal thickness results to be around 65 nm, for $n_i \approx 2.4$. It is to be noted that the optimal choice of the refractive index of the coating material, which is the square root of the Ge refraction index ($\sim 5.4$), is close to the value set to optimize the refraction index matching method.

### 3.2.4 Neganov-Luke light detectors

A powerful method to boost the signal from the light detector is an application of the Neganov-Trofimov-Luke effect on semiconductor absorbers. This effect can be observed in a bolometer when an electric field is applied in its volume. The charges, produced by an ionizing particle, while drifting along the field, produce phonons. The supplementary phonons are increasing the thermal signal proportionally to the number of produced e-h pairs. Each e-h pair has potential energy equal to $eV$, where $e$ is electron charge and $V$ is the voltage applied by

the electrodes. If $E_c$ is the energy necessary for one e-h pair production, then $N = E/E_c$ is the number of produced pairs, and the total thermal signal $E_t$ measured after the absorbtion of energy E is

$$E_t = E(1 + eV/E_c). \tag{3.14}$$

In germanium, the energy gap between the valence band and the conduction band is 0.64 eV, but only a part of interacting particle energy is used for e-h production. $E_c$ should be divided by the quantum efficiency $\eta(E)$, which depend on the interacting particle energy, but becomes constant for E>2.2 eV.

In bolometric searches this kind of light detectors is required in cases when the crystals do not produce scintillating light: for example, $TeO_2$ crystals in $0\nu2\beta$ decay experiments. In this case, with the signal amplification the Cherenkov light can be detected with the amplitudes, sufficient for particle discrimination [89]. Moreover, if the light yield is too weak for acceptable discrimination of $\alpha/\gamma(\beta)$ particles, Neganov-Luke light detectors are used to amplify the scintillation light. A description of such application can be found in Chapter 7 for $Li_2WO_4$ crystal.

## 3.3 Bolometer signal

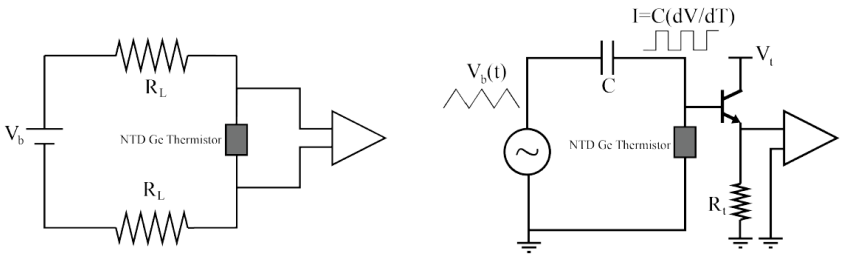


FIGURE 3.4: The electric scheme of the bias circuit for the thermistor readout with DC circuit on the left and AC circuit on the right [90].

As it was already said before, the temperature increase in the absorber is translated to a voltage signal from NTD sensor. There are two main methods to establish the NTD circuit (both types of circuits were used in this work):

- Direct current (DC): the NTD sensor is polarized through symmetric circuit shown in Fig. 3.4. The current is static and its value is controlled by a constant voltage $V_{bias}=V_{bol}+2R_L \times I$. The two load resistors should be $R_L \gg R_{NTD}$ to obtain a stable current flow in the NTD. An amplifier is connected to the bolometer output. All the front-end electronics is operated at room temperature, while the sensor output is connected through

a twisted wire, thermalized inside the cryostat. This kind of electronic is used for Ulysse and CUPID-0 cryostats (see Appendix A) and adopted from CUORE approach [91].

- In the EDELWEISS set-up (see Appendix A) the AC (alternating current) bias circuit is used. The current flow through the sensor is established through a square wave, which is obtained thanks to running a triangular wave through a capacitor (see Fig 3.4). The square wave is needed to have constant power in the thermistor. The signal from the bolometer is transferred to an AC-amplifier. This approach allows to shift the signal frequency to a high frequency region, which is free from low frequency components of the amplifier noise, which can affect the signal quality. As a drawback, the demodulation is required: a procedure of true signal shape reconstruction (includes inversion of negative sections and a low pass filtering).

### 3.3.1 Detector response: signals

The thermal signals from a bolometer have two main components: the region of rising signal, and the decaying region. The rise time of the signal is related to the time, needed for the heat to reach the sensor. This time constant (measured as time, required for the signal to rise from 10% to 90% of its amplitude) is relatively fast, and it gives ≈10% of the total duration of the signal. The decay time(measured as time, required for the signal to go down from 90% to 30% of its amplitude) of the signal is related to thermalization of the sensor to the heat sink. Such signal shape can be well described by several exponent components (in first approach two, often three are required for an accurate pulse fit).

The pulse shape (time evolution) depends on the detector characteristics (heat capacity, thermal conductance), the working point (bias current) and the temperature. The output signal has two main components: the pulse shape function and the noise. To extract all useful information it is important to minimize the noise contribution. The optimal filtering is applied for analysis in this case, also allowing to perform a precise pulse-shape investigation.

#### Optimal filtering

The signal can be described as $S(t) = A_0 f(t)$, where $A_0$ is the signal amplitude and $t$ is time. It is the most important parameter, as it gives the information on the energy of the absorbed particle. Essential is to obtain the best estimation of $A_0$ in the presence of the noise with known spectral density $e_n(f)$. The calculation in the time domain appears to be problematic, as the noise is correlated in different time bins.

To simplify the processing, the $S(t)$ is subjected to discrete Fourier transform to obtain $s_i$ values, which are the signal amplitudes in the

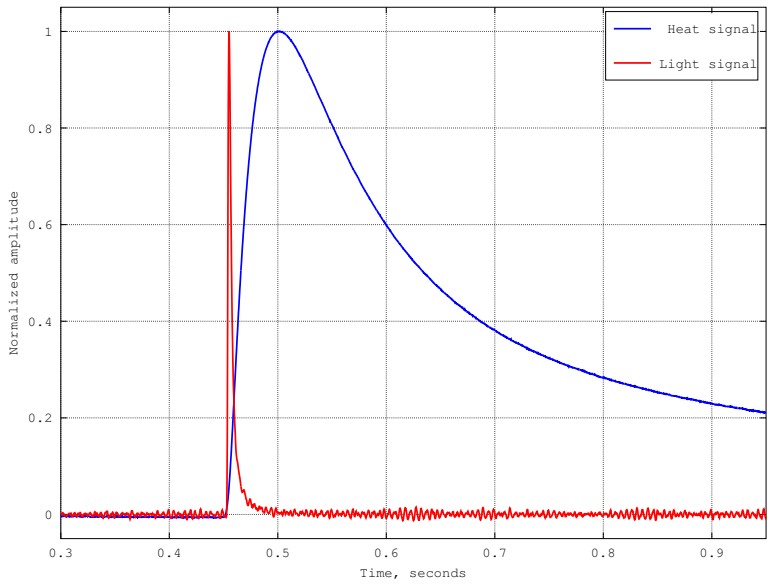


FIGURE 3.5: Typical signals from two bolometers in coincidence: in red is the signal from a light detector, in blue is the signal from crystal absorber.

i$^{th}$ frequency bin and each $s_i$ is proportional to the $A_0$ value. The RMS of the noise is given by $n_i$ in the frequency domain. If we introduce set of weights $w_i$ so that expected signal value is

$$A = \sum_{i=1}^{\infty} w_i s_i \tag{3.15}$$

and the noise fluctuation is:

$$\Delta A_{RMS} = (\sum_{i=1}^{\infty} (w_i n_i)^2)^{1/2} \tag{3.16}$$

The $w_i$ should allow to maximize the signal-to-noise ratio ($A/A_{RMS}$), and this maximization can be obtained from the solution of equation (the derivative $A/A_{RMS}$=0 [92]):

$$w_k = \frac{s_k}{n_k^2} (\sum_{i=1}^{\infty} (w_i n_i)^2 / \sum_{i=1}^{\infty} w_i s_i) \tag{3.17}$$

In the frequency domain we transfer from $w_i$ weights to the transfer function $W(j\omega)$ so that the treated signal ($\tilde{s}(T)$) is:

$$\tilde{s}(T) = \frac{A}{2\pi} \int_{-\infty}^{+\infty} W(j\omega) S(\omega) e^{-j\omega t} d\omega \tag{3.18}$$

The RMS noise after the filter application is described by following equation:

$$\langle \tilde{n}^2 \rangle^{\frac{1}{2}} = (\frac{1}{2\pi}\{\int +\infty_{-\infty} N(\omega)|W(j\omega)|^2 d\omega\}^{\frac{1}{2}} \tag{3.19}$$

where $N(\omega)$ is the spectral power density of the noise. The transfer function is chosen to maximize the signal to noise RMS ratio. The easiest way to find the transfer function in this case is to maximize the square of this ratio:

$$\frac{\tilde{s}(T)}{\langle \tilde{n}^2 \rangle^{\frac{1}{2}}} = \frac{A}{2\pi} \frac{\{\int_{-\infty}^{+\infty} W(j\omega)S(\omega)e^{-j\omega t}d\omega\}^2}{\int +\infty_{-\infty} N(\omega)|W(j\omega)|^2 d\omega} \tag{3.20}$$

After the equation solution, the transfer function appears as follows:

$$W(j\omega) = (Constant)\frac{S^*(\omega)}{N(\omega)}e^{-j\omega t} \tag{3.21}$$

This optimal filtering method was proposed by Gatti and Manfredi [93]. This filter gives the best signal-to-noise ratio, but the signal shape is not conserved. This approach is widely used in data analysis of bolometric signals, allowing to extract the amplitudes from the background noise with high efficiency.

## 3.4 Summary

The technology of bolometer detectors was developing fastly during last decades: starting from few grams of absorber material, nowadays there are experiments, operating hundreds of kilograms of bolometric crystals. This technique, depending on the absorber compound, can be used for various applications: dark matter searches, $0\nu2\beta$ decay, neutrino scattering, neutron detectors. The detectors, operated in proper conditions, can reach high energy resolution at the level of 0.1% FWHM. With the right choice of the absorber and sensor, various energy regions can be investigated.

With the use of scintillating crystals, the $\alpha$ background rejection will allow to reach very low background levels, needed for ton-scale "zero-background" experiments.

In the following chapters, the development and application of scintillating bolometers for $0\nu2\beta$ decay search is described.

# Chapter 4

# LUMINEU R&D: $ZnMoO_4$ and $Li_2MoO_4$ bolometers

LUMINEU (Luminescent Underground Molybdenum Investigation for NEUtrino mass and nature) is a project using scintillating bolometers for high sensitivity searches for neutrinoless double beta decay. The final goal of the LUMINEU project is to demonstrate that a ton-scale experiment based on the same technique can be sensitive enough to explore the parameter space of the inverted hierarchy region of the neutrino mass pattern.

The $^{100}$Mo isotope was chosen for its high transition energy (3034 keV), which is higher than the end-point of natural $\gamma$ radioactivity (2615 keV), possibility to enrich in big amounts (with the gas centrifugation method) and favorable theoretical predictions for the $0\nu2\beta$ decay rate. The decay scheme of $^{100}$Mo is shown in Fig. 4.1.

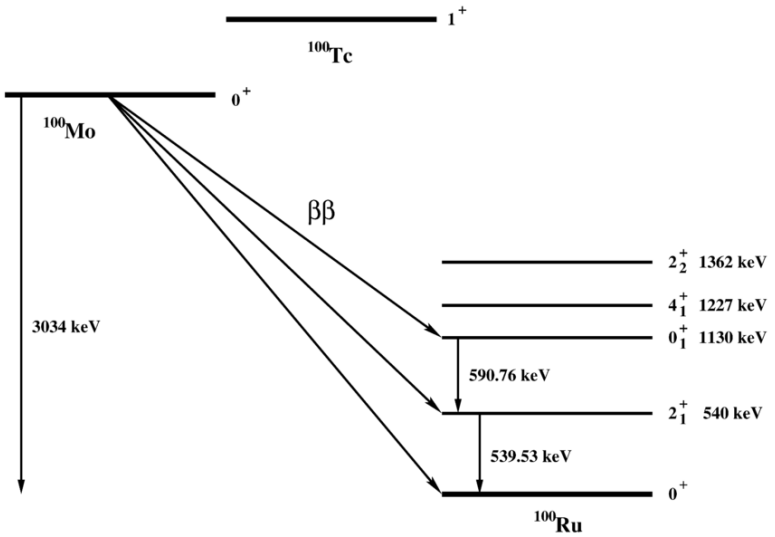


FIGURE 4.1: The double beta decay scheme of $^{100}$Mo to the ground and excited states of $^{100}$Ru [94].

Funded by ANR, the project started in 2012 with the goal to develop a technology of Mo-based scintillating bolometers suitable for a ton-scale experiment. During these years multiple tests on Mo-containing crystals with light detectors were performed. At the beginning the

main compound of interest was $ZnMoO_4$, but during the development of the project, another promising compound was considered: $Li_2MoO_4$. Natural and enriched crystals were tested both aboveground and underground [90]. The quality and radiopurity of crystals were significantly improved during the project development and the decision on the final crystal type has been made. The $ZnMoO_4$ crystals were giving promising results with high energy resolution and good radiopurity. First enriched crystals of $Zn^{100}MoO_4$ were produced and measured in underground conditions. In parallel, $Li_2MoO_4$ crystals were tested as an additional possibility, showing very promising results in terms of performance and radiopurity.

In the following a description with results of the main tests performed within LUMINEU project are reported. I have actively participated in these measurements, including activities such as the detector assembly, installation in the cryostat and data analysis.

### 4.0.1 Development of Mo-based crystals

FIGURE 4.2: The $Li_2MoO_4$ crystal boules (left), and $ZnMoO_4$ crystal boules (right). $ZnMoO_4$ boules have less homogeneous structure due to difficulties in crystal growth.

The first step of the LUMINEU project, was to develop a dedicated protocol for molybdenum purification. The widely used procedure of molybdenum oxide ($MoO_3$) sublimation under atmospheric pressure is not meeting the requirements on the concentration of impurities for $0\nu2\beta$ decay searches (due to the chemical affinity of W and Mo, the W content is too high). The new developed procedure requires addition of high pure $ZnMoO_4$ (1%) to the $MoO_3$ so that an exchange reaction occurs:

$$ZnMoO_4 + WO_3 = ZnWO_4 + MoO_3 \uparrow \tag{4.1}$$

This reaction allowes to reduce the tungsten concentration in $MoO_3$ and to perform a separation of W compound. For further purification an additional recrystallization of ammonium molybdate from aqueous solutions is performed [95].

For the crystal production, the low-thermal-gradient Czochralski technique has been chosen. This method was developed at the Nikolaev Institute of Inorganic Chemistry (NIIC, Novosibirsk, Russia). The crystal growth occurs in highly pure platinum crucibles (⌀40 and ⌀80 mm diameter). The temperature gradient is below 1 K/cm and the crystallization speed is 0.8-1.2 mm/hour. It allows to grow a large-mass (∼1.5 kg) colorless boules with a high yield (∼80%), which is important for the growth with use of enriched materials. The irrecoverable losses of material are less than 0.6 %. In case of $ZnMoO_4$, a double crystallization protocol was applied to improve the crystal quality, while for $Li_2MoO_3$ single crystallization is sufficient.

## 4.1 Underground measurement on $ZnMoO_4$ and $Li_2MoO_4$ scintillating bolometers

This thesis activity has started simultaneously with the preparation of detectors for a run in the EDELWEISS set-up, marked as "run 310" (for more information on the cryostat, see Appendix A). The main goal of this measurement was to directly compare the performance of two detectors based on $ZnMoO_4$ and $Li_2MoO_4$ compounds in the same working conditions. This comparison is the milestone for LUMINEU project, as the outcome of the run will lead to the decision on the compound which will be used in the demonstrator phase of this activity.

In the EDELWEISS cryostat, detectors are usually installed in the so-called "galette", rigidly fixed. For run 310, it was decided to use a suspension system for scintillating bolometers to reduce the microphonic noise of the detectors, induced by vibrations coming from thermal machines, as demonstrated in other bolometric experiments [96]. The noise issue requires specific attention, as it can strongly affect the detector energy resolution and light detectors performance.

### Crystals

Two crystals were chosen for this run for a direct comparison of the two compounds (see Fig. 4.3). Both crystals were grown in Nikolaev Institute of Inorganic Chemistry with low-thermal-gradient Czochralski method, using purified $MoO_3$. Both elements have high purity and optical quality.

- Natural $ZnMoO_4$: ⌀ 50×40 mm, weight - 334 g, high transparency, yellow color. It was already measured as scintillating bolometer in underground test, and considered as reference detector with the best performance at that moment [97].

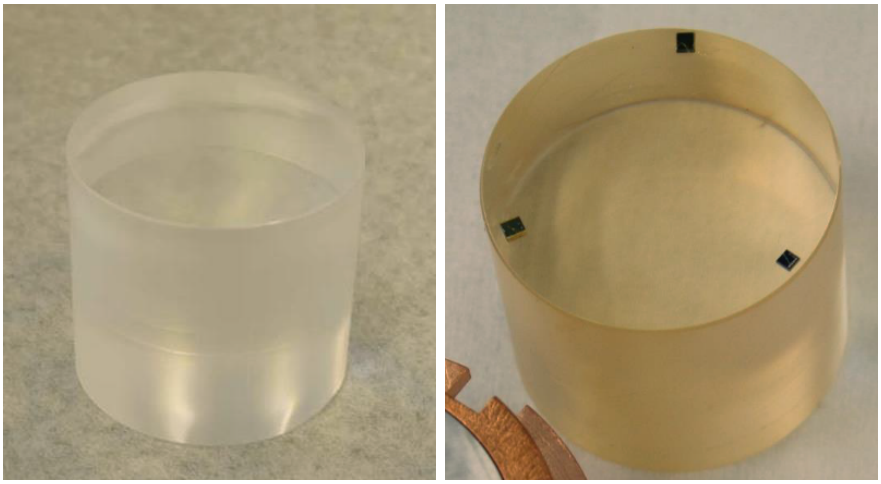

FIGURE 4.3: The two crystals before detector assembly. $ZnMoO_4$ crystal with already glued sensors is on the right, $Li_2{}^{100}MoO_4$ without any treatment is on the left.

- Enriched $Li_2{}^{100}MoO_4$: ∅ 44×40 mm, weight - 185.8 g, high transparency, white color. It was never measured before, first large grown enriched crystal of this type.

### 4.1.1 Detector assembly

The holders for bolometers are providing mechanical support and they are working as a thermal bath for the crystal. Copper is used as holder material since it is a soft metal and it is simple to machine custom shapes. Radiopure copper is available in large amount for low-background measurements. Oxygen-bearing copper is known to be a suitable material for cryogenic measurements as it can be cooled down to 10 mK temperatures without heat release during the cooling down. The inner surface of detector cavity was covered with a reflecting foil (3M, 99% reflection) for better light collection from scintillation light.

As spacers between the absorber and the holder, PTFE (polytetrafluoroethylene) elements were used: L-shape in the bottom part, S-shape on the top. PTFE is a well-known radiopure material. Additionally to the thermal link function, PTFE spacers are providing fixation of the crystal and compensation of the thermal contraction during cooling down. Light detectors were made of thin germanium wafers (high purity, produced by UMICORE) with the size of ∅ 44×0.17 mm. When assembled, they are facing the circular base of the crystal, being also kept by PTFE elements (see fig. 4.4).

The suspended tower design and production of holders were provided by CEA-SPEC (Service de Physique de l'Etat Condense).

In this run, each scintillating crystal had two heat channels provided by NTD sensors, and one silicon resistance (so-called heater).

This resistance is used for baseline stabilization, and its utilization can significantly improve the energy resolution of the detector [98]. The light detectors were equipped only by one NTD of reduced size. For the final analysis, the heat channel with the best performance was chosen out of two available.

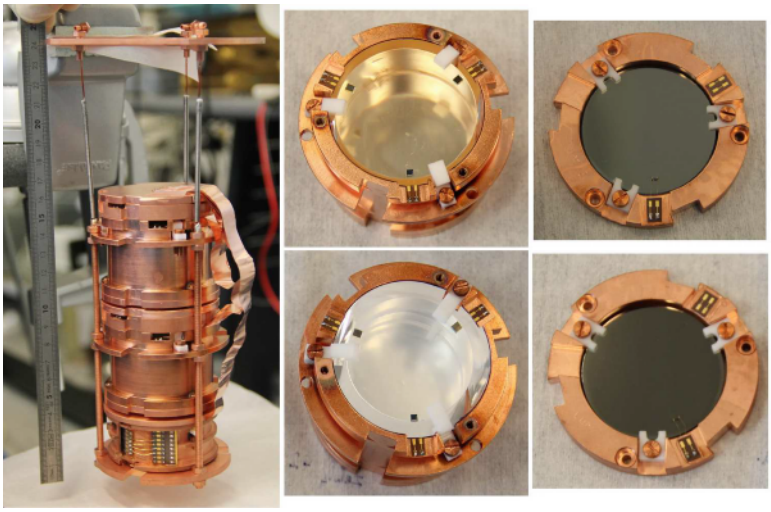

FIGURE 4.4: The suspended tower (on the left) with $ZnMoO_4$ bolometer on top, $Li_2{}^{100}MoO_4$ in the middle, and EDELWEISS germanium detector on the bottom. On the right: crystals and light detectors before tower assembly.

### Cleaning procedure of the detector elements

A careful cleaning of all detector elements is required to avoid the surface contamination which can affect the low-background measurements. For this run the procedure was the following:

1. Cleaning with soap: Solution of ultrapure water and ELMA micro-60 concentrated cleaning solution in proportion 10:1 was used in combination with the ultrasonic bath at 40-50 °C for 15-20 minutes. After this procedure, all pieces were rinsed with ultrapure water, immersed in ethanol, then dried.

2. Etching with nitric acid: Etching was done with 30% acid solution with ultrapure water. This solution was prepared using 70% ultrapure nitric acid and water in proportion 100:130. All pieces were immersed into the solution for 30 seconds (15 seconds for copper screws), then rinsed in the tap water, ultrapure water and ethanol, in each for 60 sec.

3. Drying was performed using an industrial dryer with temperature 120 °C and wipes.

4. PTFE pieces were cleaned with soap solution and ultrasonic bath (as in point 1), and with ethanol and ultrasonic bath, no acid treatment.

### Gluing

The quality of sensors coupling can strongly affect the performance of the sensors [99]. The radiopure two-component glue Araldite was used for NTD and heaters coupling to the crystals [100]. This glue has a viscosity of 30 Pa×s and low radioactivity of $<8.9\times10^{-4}$ Bq/kg of $^{232}$Th and $<1.0\times10^{-2}$ Bq/kg of $^{238}$U [101]. In case of NTD thermistors, the

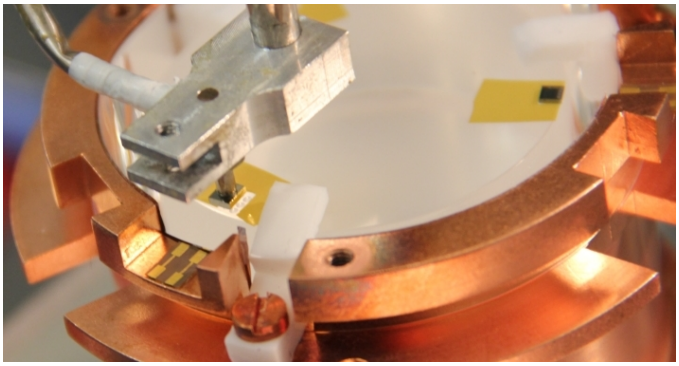

FIGURE 4.5: The gluing process on the $Li_2{}^{100}MoO_4$: mylar mask is surrounding the six glue spots, NTD, kept by a pump, will be pressed over the mask.

glue was deposited on the crystal surface using a matrix with pogopins to make six homogenous spots. The distance between NTD and crystal surface is 50 $\mu$m (a mylar mask of required thickness is used – see Fig. 4.5), so the spots will not be merged. After mixing the components, there are only 3 minutes to perform the gluing procedure before polymerization.

### Electrical contacts

For thermal and electrical contact of NTDs and heaters, gold bonding wires ($\varnothing$ 25 $\mu$m) are used. A Kapton foil with gold contact pads was used for wire connection: a gold wire is bonded on NTD and on a golden pad, while a wire for the outer electrical connection is soldered on the other side (see Fig. 4.6). The contact pads are glued on the copper holders with Araldite glue.

## 4.1.2 Detector performance

The suspended tower was installed in the EDELWEISS cryostat in January 2016. After the cooling down and temperature stabilization, the optimum working point was established for all detectors. A precise

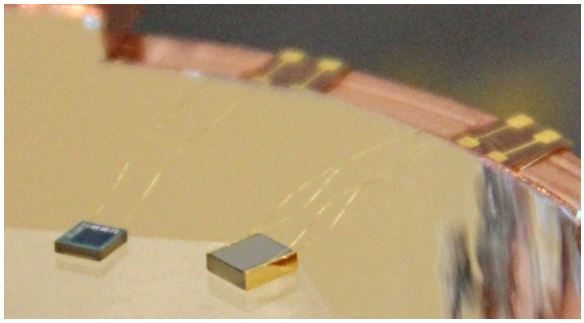

FIGURE 4.6: Example of NTD and heater bonded with golden wires on kapton contact pad.

investigation of crystal performance was performed at the base temperature of 19-20 mK. The total acquisition duration was more than 2000 hours (13th March – 5th July 2016). A minor part of collected data was rejected due to temperature perturbations or high noise on the detectors. The major part of the elapsed time was dedicated to the physics data collection – the background (>1400h). The data was collected in the "trigger mode", where only events with a certain threshold are recorded within a defined time window. If one channel is triggered, all the other channels are recorded in coincidence. For more information on data acquisition system see [102]. The trigger was set on the heat channels, while the light signals were recorded in coincidence with a delay, depending on the rise time of signals.

### Noise

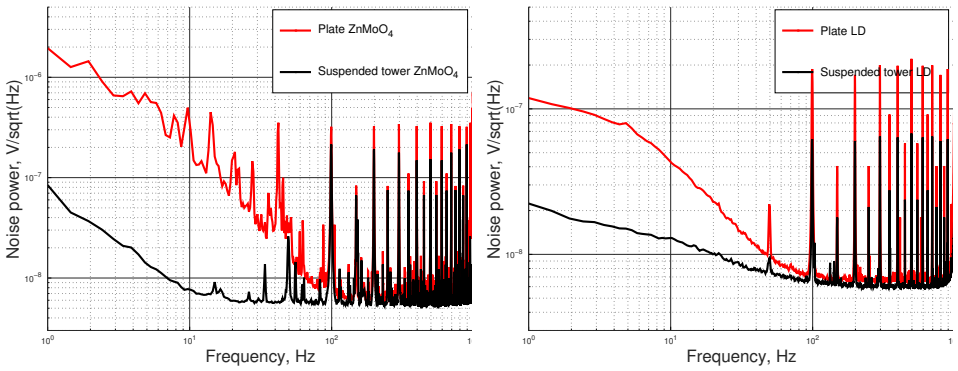


FIGURE 4.7: Comparison of noise spectra for detectors with rigid fixation (red) and suspension (black). The right plot is showing $ZnMO_4$ noise spectra while the left plot is showing light detectors noise.

During the first measurement taken with scintillating bolometers in the suspended tower in the EDELWEISS set up, we have collected noise spectra to compare the noise level for the detectors in the suspended

tower compared to those on the plate. The comparison is shown in Fig. 4.7. From the plots one can see that noise level in the low-frequency region is reduced by one order of magnitude going from $10^{-7}$ V/$\sqrt{Hz}$ to $10^{-8}$ V/$\sqrt{Hz}$ in the signal region. These measurements have confirmed the efficiency of suspension systems for bolometric measurements in the EDELWEISS cryostat.

### Stabilization

After the processing of raw data, an essential step is the baseline stabilization: the baseline level is drifting with time and it can strongly affect the energy resolution of the detector. To solve this issue, we use silicon resistances, glued on the crystal surface. During the measurement short voltage pulses are injected in such resistances, resulting in a signal with constant amplitude in the detector. The pulses were injected each 60 seconds with 2.5 V amplitude. Heater events can be discriminated by the correlation of the pulse shape parameter: heater signals have the different shape. Usually, the injected pulses are located in the high energy region in order to not interfere with physical events. Fig. 4.8 demonstrates the effect of stabilization on energy resolution: a narrow peak appears after applying the procedure, significantly improving the energy resolution. Heater events are rejected after stabilization procedure and they do not appear in the final spectrum.

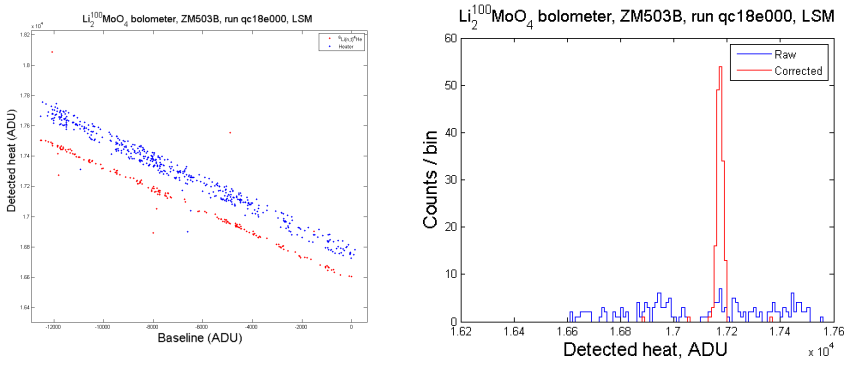


FIGURE 4.8: Stabilization procedure: baseline versus energy plot on the left, energy spectrum before and after stabilization on the right.

### Performance: energy resolution

Several calibration sources were used during the run for energy calibration and resolution measurements. In the EDELWEISS cryostat there are sources with $^{60}$Co and $^{133}$Ba, controlled remotely. $^{133}$Ba is used for calibration of germanium detectors for Dark Matter searches. $^{60}$Co sources are used for regeneration of ionization channels, and they are too intense (≈200 kBq) to perform calibration of scintillating bolometers: tremendous events rate does not allow to acquire meaningful data

in the heat channel. In future measurements (see Section 4.3.2), we started to use the $^{60}$Co source for light detectors calibration.

### Ba calibration

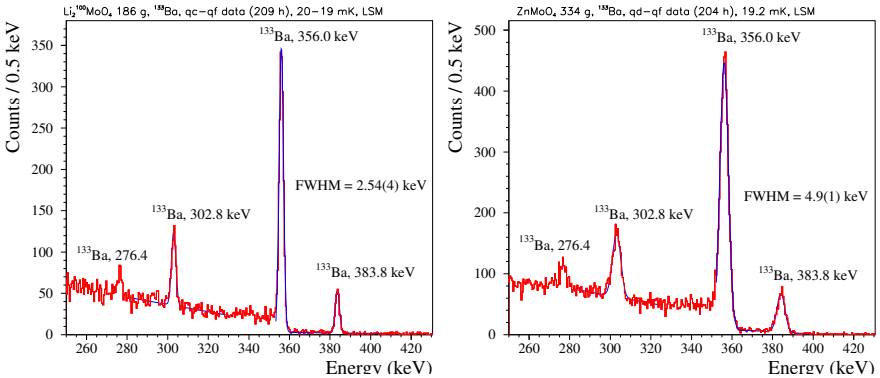


FIGURE 4.9: Barium calibration, performed over 200 hours for $Li_2{}^{100}MoO_4$ (left) and $ZnMoO_4$ (right). Energy resolution of the $Li_2{}^{100}MoO_4$ bolometer is almost 2 times higher.

$^{133}$Ba source was used periodically and total spectra were accumulated during $\approx$ 200 h. The spectra of two crystals are shown in Fig. 4.9. The $^{133}$Ba peaks are fitted with Gaussian peak and flat background. The energy resolution on the most intense peak (356.0 keV) for $Li_2MoO_4$ is 2.5 keV, which is almost two times better than for $ZnMoO_4$ with FWHM at 4.9 keV.

Barium calibration data were also used to monitor the stability of the detectors energy scale in time. Short calibration runs were often performed (every 1-2 days), as it was also required for dark matter research.

### Potassium calibration

A potassium calibration was performed in order to check the viability of Geant 4 Monte-Carlo simulation model. $^{40}$K is an appropriate source for this objective, as it has a strong single $\gamma$ line at 1461 keV, and it is sufficiently easy to build a simulation model.

A custom source was produced using potassium salt (KCl). The salt was dried in the oven in order to reduce the amount of water and estimate precisely the total weight of source. The salt with the total mass of 331.4 g was hermetically sealed in four plastic boxes and placed on the top of the cryostat for calibration (see Fig. 4.10). Total calculated activity of the source in $^{40}$K was 5.5 kBq (calculated out of total mass of the salt and the isotopic abundance of $^{40}$K. The result of calibration and comparison with simulations is shown in Fig. 4.11. The simulated spectra and detection efficiencies in peak and continuum

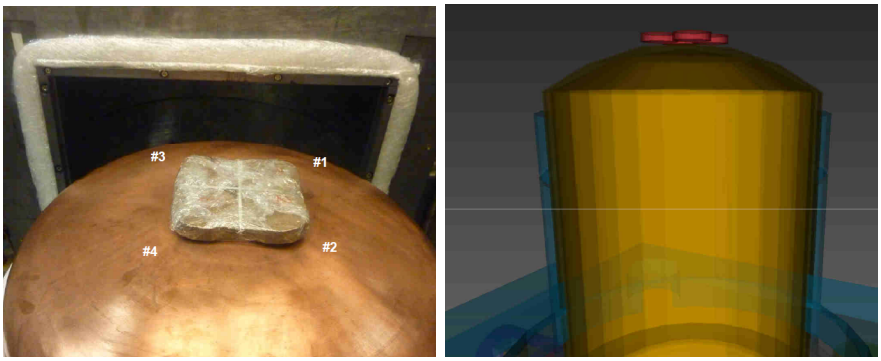


FIGURE 4.10: The potassium source, placed on the top of the cryostat on the left and simulated set-up on the right.

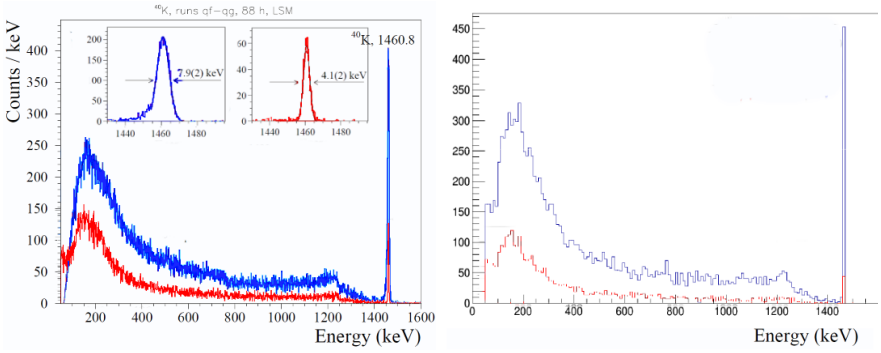


FIGURE 4.11: $ZnMoO_4$ (blue) and $Li_2{}^{100}MoO_4$ (red) potassium calibration spectra on the left, and simulated spectra on the right.

are in reasonable agreement with the experimentally measured ones [103]. The summary and comparison of simulated and experimental efficiencies are listed in Tab. 4.1.

TABLE 4.1: Comparison of simulated end experimental efficiency with $^{40}K$ calibration.

| | $N_{decays}$ | $N_{peak}$ | Efficiency in peak, $10^{-6}$ | Efficiency 1.1-1.2 MeV, $10^{-6}$ |
|---|---|---|---|---|
| $ZnMoO_4$ sim | $10^8$ | 465(22) | 465(22) | 3.71(19) |
| $Li_2{}^{100}MoO_4$ sim | | 45(7) | 0.45(7) | 0.68(8) |
| $ZnMoO_4$ exp | $1.74\times10^9$ | 6177(79) | 3.56(9) | 3.26(4) |
| $Li_2{}^{100}MoO_4$ exp | | 663(26) | 0.38(2) | 0.69(2) |
| | | | | |
| $ZnMoO_4$ sim/exp | | | 1.31(9) | 1.14(7) |
| $Li_2{}^{100}MoO_4$ sim/exp | | | 1.18(17) | 0.99(15) |

### Thorium calibration

The thorium calibration was performed with a $^{232}$Th source made of thoriated tungsten wires containing 1% of thorium in weight. The source was fixed on the external shield. Using this calibration the energy resolution in high energy region was estimated with $^{208}$Tl peak. Thanks to different values of FWHM in a wide energy section, we estimated the energy resolution in the region of interest (at $Q_{\beta\beta} = 3034$ keV). Results are shown in Tab. 4.2 and the spectra are in Fig. 4.12. The $Li_2{}^{100}MoO_4$ detector has better energy resolution in average for all energy regions. It is clearly seen that energy resolution of $Li_2{}^{100}MoO_4$

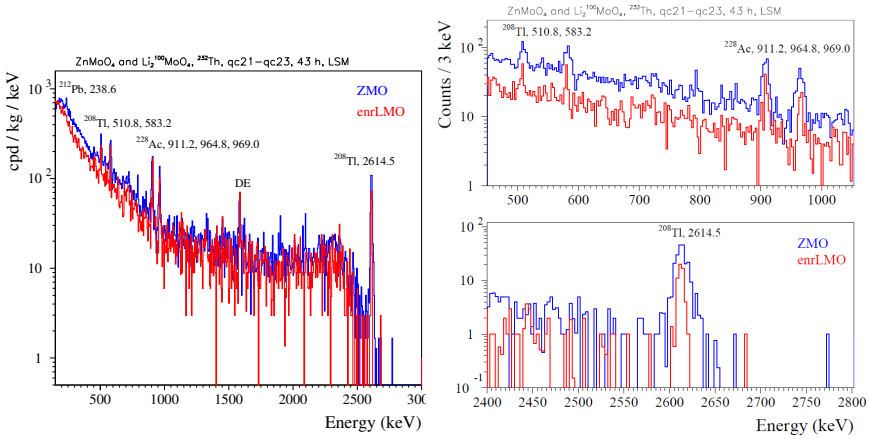


FIGURE 4.12: Thorium calibration, performed over 43 hours for $Li_2{}^{100}MoO_4$ (left) and $ZnMoO_4$ (right).

is higher by a factor two. $ZnMoO_4$ was demonstrating good performance, even though the detector did not reach its best energy resolution, obtained in previous measurements (FWHM 9 keV at 2615 keV was reached at lower temperature of 18 mK, published in article [97].In the same article it is described the comparison of energy resolution dependence on energy for $Zn^{100}MoO_4$ and $Li_2{}^{100}MoO_4$ with the measurements, performed in better conditions (lower base temperature, lower baseline noise) in LNGS, and the energy resolution is shown in Fig. 4.13. The test on $Li_2{}^{100}MoO_4$ in LNGS is described in following section. These measurements impacted the final decision on compound choice, as the overall performance of $Li_2{}^{100}MoO_4$ detectors is better than of $ZnMoO_4$ in various conditions.

### Particle discrimination

Using the scintillation light, it is possible to perform the discrimination of $\alpha$ particles from $\gamma/\beta$ band. As $\alpha$ particles emit less light than $\gamma/\beta$ ones with the same energy, amplitude of the light signal gives us essential information for the background rejection. The triggering was performed on heat channel and the light pulses amplitudes were

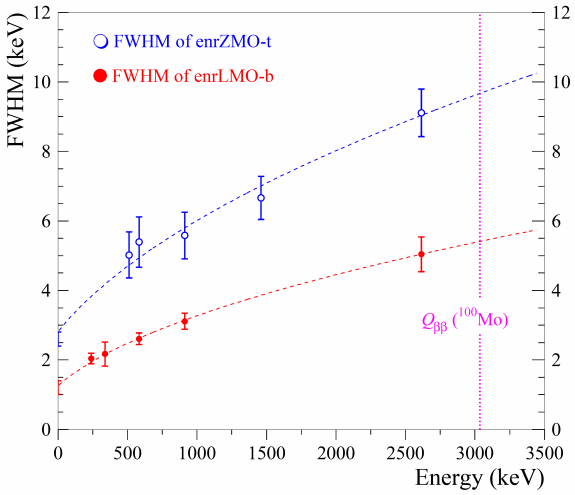


FIGURE 4.13: Energy resolution dependence on energy, with fit and estimation of FWHM in region of interest ($Q_{\beta\beta}$=3034 keV). The fits to the data by a function $FWHM(keV) = \sqrt{(p_1 + p_2 \times E_\gamma(keV))}$ ($p_1$ and $p_2$ are free parameters) are shown by the dashed lines. The parameters of fits are 7.9(5) keV$^2$ and 0.0282(6) keV for the $Zn^{100}MoO_4$ and 1.6(2) keV$^2$ and 0.0091(3) keV for the $Li^{100}MoO_4$.

measured in coincidences. After processing of the data, the heat amplitude (energy) versus light amplitude (energy) scatter plots are built to perform the particle discrimination. The resulting scatter plots (background measurement) are shown in Fig. 4.14, and the Q-plots (light yield versus energy) are shown in Fig. 4.15.

The discrimination power (DP) is calculated as follows:

$$DP(\sigma) = \frac{LY_{\beta/\gamma} - LY_\alpha}{\sqrt{\sigma^2_{\beta/\gamma} + \sigma^2_\alpha}} \tag{4.2}$$

Where LY and $\sigma$ are the parameters of Gaussian fit of the light/heat amplitude at the energy of interest. The amount of scintillation light is higher for $ZnMoO_4$, but the full discrimination of the $\alpha$ band is achieved for both detectors, with $18\sigma$ for $Li_2{}^{100}MoO_4$ and $21\sigma$ for $ZnMoO_4$ (see Fig. 4.16).

During these measurements, we have observed a problem of "bright" alphas: several events in the alpha region had light amplitude, higher than average light amplitude for alpha particles. These events are considered to appear because of scintillation of reflecting foil. As the reflecting foil can scintillate itself, the $\alpha$ decays on the crystal surface can deposit energy on the foil, producing an additional scintillation light, enhancing the light signal. If such event takes place, energy-degraded

TABLE 4.2: Summary on $Li_2{}^{100}MoO_4$ and $ZnMoO_4$ energy resolutions at 20 mK.

| Energy (keV) | FWHM (keV) | |
|---|---|---|
| | $Li_2{}^{100}MoO_4$ | ZMO |
| 0 | 1.2 | 3.6 |
| 356 | 2.54(4) | 4.9(1) |
| 511 | 3(1) | 8(2) |
| 583 | 4(1) | 9(2) |
| 911 | 3.1(5) | 10(1) |
| 1461 | 4.1(2) | 7.9(2) |
| 2615 | 6.3(6) | 13(2) |

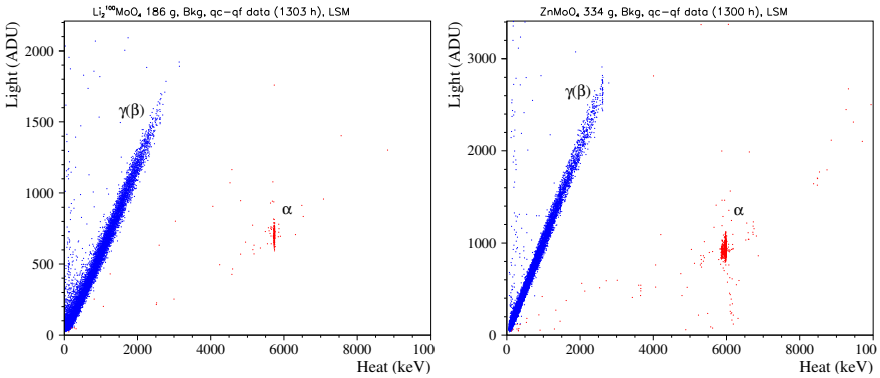


FIGURE 4.14: Scatter plots of background measurements, collected over more than 1300 h for $Li_2{}^{100}MoO_4$ (left) and $ZnMoO_4$ (right)

alphas can populate the region of interest, providing an avoidable background. This issue was studied experimentally in the next run (see next sections).

### Neutron calibration

A neutron calibration of detectors was performed with an AmBe source. $^{241}Am$ produces an $\alpha$ particle, which interacts with $^{9}Be$, resulting in $^{12}C$ and neutron emission.

The neutron cross-section with $^{6}Li$ is very high with reaction $^{6}Li(n,t)\alpha$. With the natural content of $^{6}Li$ (7.6%) in $Li_2{}^{100}MoO_4$, we performed a measurement of thermal neutron capture peak with an excellent result: a FWHM of 5.9(2) keV (see Fig. 4.17). It is one of the best resolutions obtained with this reaction.

The $Li_2MoO_4$ scintillating bolometers can be efficiently used as neutron detectors: they have a background-free region of interest (thanks to particle discrimination), ≈100% detection efficiency of thermal neutrons and excellent resolution on neutron peak.

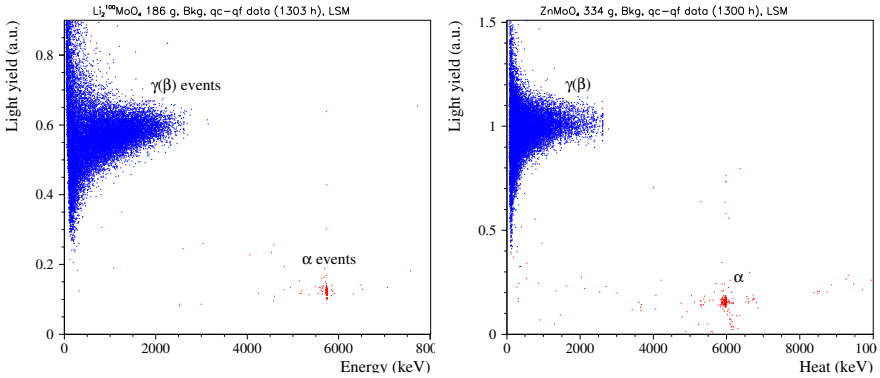


FIGURE 4.15: Q-plots of background measurements, collected over more than 1300 h for $Li_2{}^{100}MoO_4$ (left) and $ZnMoO_4$ (right).

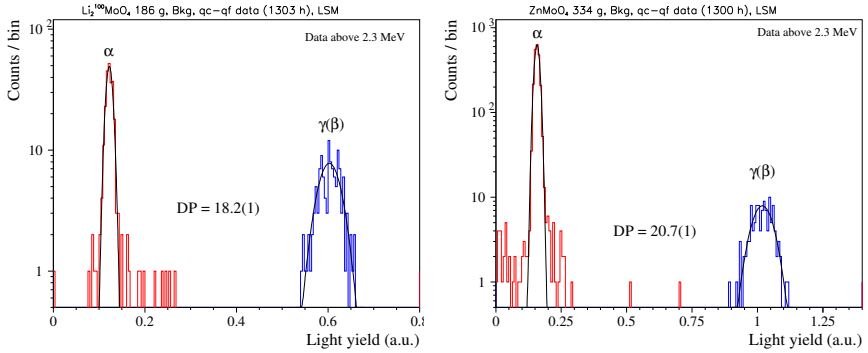


FIGURE 4.16: Light yield histogram with estimated discrimination power by Gaussian fit for $Li_2{}^{100}MoO_4$ (left) and $ZnMoO_4$ (right).

## Background

The background measurements, used for analysis after the rejection of bad quality data, were acquired during 1300 h. In Fig. 4.18. we can see the effect of crystal enrichment: the $Li_2{}^{100}MoO_4$ spectrum had the strong component of $2\nu2\beta$ decay events.

Thanks to particle discrimination, the precise investigation of the $\alpha$ region was performed (see Fig. 4.19). The radiopurity of $Li_2{}^{100}MoO_4$ is at excellent level: $^{210}$Po activity is at 0.23(2) mBq/kg, while for $ZnMoO_4$ crystal it is at 1.32(3) mBq/kg.

These results confirm the high quality of the crystals and demonstrate the power of particle discrimination with scintillation light: this method has high efficiency, resulting in very low backgrounds in the region of interest.

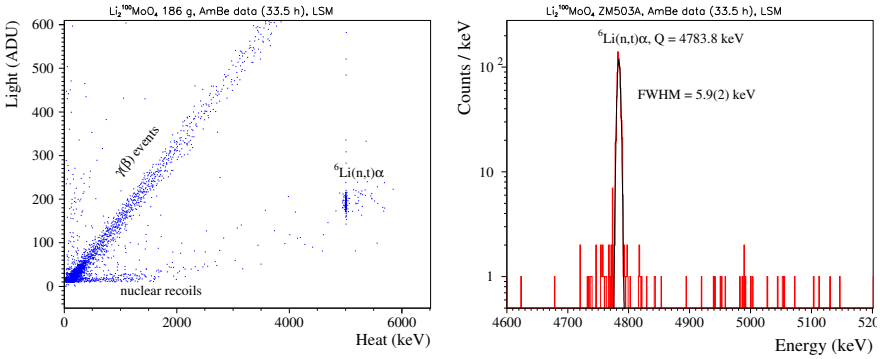


FIGURE 4.17: Scatter plot of $Li_2{}^{100}MoO_4$ during AmBe calibration (left) and the peak of $^6$Li(n,t)$\alpha$ reaction on the right.

### Double beta decay investigation

The spectrum, accumulated with an exposure of 10 kg×day, was fitted by a simple background model with the result:

$T_{1/2}^{2\nu2\beta} = 6.90 \pm 0.15(stat) \pm 0.42(syst) \times 10^{18}$ yr.

This value is one of the most precise measurements of $2\nu2\beta$ decay at that moment, obtained with a very short exposure: to compare, the result, obtained by NEMO-3 experiment with exposure of 7.37 kg is $T_{1/2}^{2\nu2\beta} = 7.11 \pm 0.02(stat) \pm 0.54(syst) \times 10^{18}$ yr [62]. This outcome again confirms perspectives for $Li_2{}^{100}MoO_4$ crystals: with good background model and increased exposure we can obtain measurements with high precision, thanks to high energy resolution and low background of these detectors.

## 4.1.3 Selection

After this direct test comparing two types of crystals as scintillating bolometers, $Li_2{}^{100}MoO_4$ and $ZnMoO_4$, a decision was taken about compound for the CUPID-Mo demonstrator. The comparison of the different features for the two types of crystals is listed as follows and main features are shown in Tab. 4.3:

- $Li_2{}^{100}MoO_4$ crystals have a higher concentration of molybdenum for the same sample weight: 55% against 44% in $ZnMoO_4$. However, the density of $Li_2{}^{100}MoO_4$ crystals is lower (3.04 g/cm$^3$ against 4.18 g/cm$^3$), so if we consider the unit volume (as cryostat experimental volume is severely restricted), $ZnMoO_4$ contains 5% more of molybdenum.

- The only radioactive isotope in both compounds is $^{100}$Mo, and it undergoes only $2\beta$ decay. Zn, Li and O natural compounds do not contain radioactive isotopes.

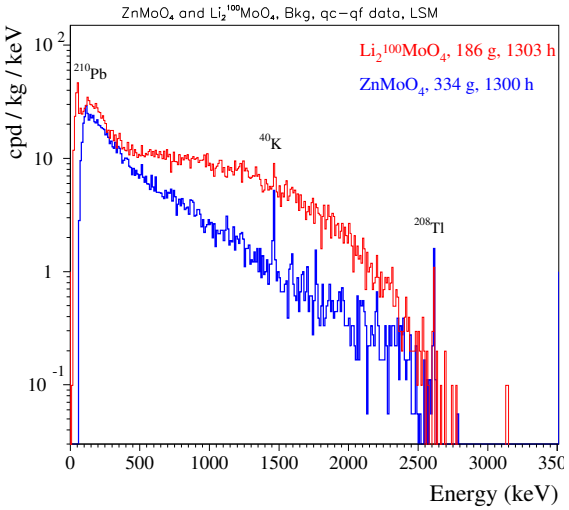


FIGURE 4.18: Background energy spectrum, collected over more than 1300 h for $Li_2{}^{100}MoO_4$ (red) and $ZnMoO_4$ (blue).

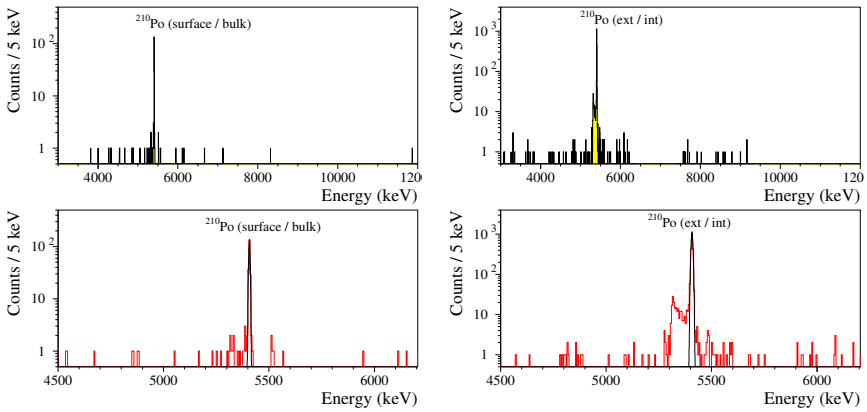


FIGURE 4.19: Background spectrum of $\alpha$ particles in high energy region of $Li_2{}^{100}MoO_4$ on the left and $ZnMoO_4$ alpha spectrum is on the right.

- Regarding the crystal growth, $Li_2{}^{100}MoO_4$ is easier to treat: it has a lower melting point, there are no phase transitions during the growth process and the crystal quality along the boule is more stable.

- $Li_2{}^{100}MoO_4$ crystals are slightly hygroscopic. However, they can be operated in clean room conditions without any special requirements. This property opens a possibility to treat the crystal surface with water etching.

- The energy resolution of $Li_2{}^{100}MoO_4$ is almost two times better than of $ZnMoO_4$.

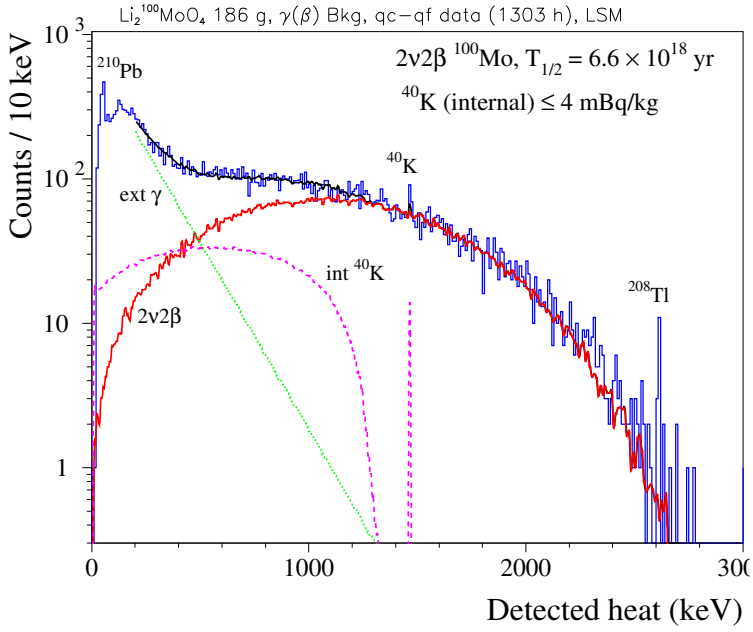


FIGURE 4.20: Background energy spectrum, collected over more then 1300 h with $Li_2{}^{100}MoO_4$ detector, and fitted by a simple model.

- The light yield of $ZnMoO_4$ is about 30% higher, but the alpha rejection at the level of $18\sigma$ or more is obtained for both types of detectors.
- The radiopurity of both compounds is high and meets the required level of internal U/Th contamination for a "zero-background" experiment.

In conclusion, $Li_2{}^{100}MoO_4$ crystals have demonstrated better performance in general, easier to grow in a large amount with good reproducibility. $Li_2{}^{100}MoO_4$ crystals were chosen as absorbers for the demonstrator stage with 20 enriched crystals.

## 4.2 Test of $Li_2MoO_4$ crystal as a scintillating bolometer at LNGS

There were produced two $Li_2{}^{100}MoO_4$ crystals from the same boule, one was tested in run 310 and described above (top of the boule), while second crystal (⌀ 44×42 mm, 203.7 g, bottom of the boule) was sent to LNGS for a complementary test and comparison of performance in two different set-ups. The scintillating bolometer was coupled with Ge light detector with no SiO coating, two NTD sensors on $Li_2{}^{100}MoO_4$,

TABLE 4.3: Comparison of $Li_2{}^{100}MoO_4$ and $ZnMoO_4$ main features.

| | $Li_2{}^{100}MoO_4$ | $ZnMoO_4$ |
|---|---|---|
| Mo concentration per unit weight | 56% | 44% |
| Mo concentration per unit volume | 55% | 60% |
| Melting point | 705 °C | 1003 °C |
| Phase transitions | No | Yes |
| Losses of enriched material | 0.1% | 0.6% |
| Double crystallization | Optional | Required |
| Crystal quality | High | Imperfections |
| Hygroscopicity | Yes | No |
| Energy resolution in ROI | ≈ 6 keV | ≈ 10 keV |
| Light yield, keV/MeV | 0.6 | 1.0 |

one on LD. Both light and heat bolometers were equipped with silicon resistance for stabilization. The crystal was surrounded by a reflecting foil (Vikuiti) for increase of light collection. A $^{55}$Fe source was used for light detector calibration.

The measurement was performed in R&D cryostat at Hall C of LNGS (see Appendix A for the cryostat description). The data-taking was performed in a stream mode with the sampling rate of the heat and light channels at 2 kHz and 4 kHz respectively. Thanks to stable operation conditions and good cryostat performance, the temperature was stabilized at 11 mK (while in EDELWEISS cryostat the range of temperatures during data-taking is ∼20 mK). The calibration was performed with use of $^{232}$Th source, ∼170 hours of calibration and ∼320 hours of background measurements were collected. The comparison of background spectra is shown on Fig. 4.21. The light detector was showing good performance with signal at ∼2.9 $\mu$V/keV, FWHM (5.9 keV) at ∼0.3 keV and the $FWHM_{bsl}$ ≈0.13 keV.

TABLE 4.4: Comparison of $Li_2{}^{100}MoO_4$ scintillating bolometers performance in two different set-ups.

| Measurement | LNGS (10 mK) | LSM (20 mK) |
|---|---|---|
| Signal, $\mu$V/MeV | ∼84 | ∼62 |
| $FWHM_{bsl}$, keV | ∼1.2 | ∼1.2 |
| FWHM at 583 keV, keV | 2.6±0.2 | 4.0±1.0 |
| FWHM at 911 keV, keV | 3.1±0.3 | 3.1±0.5 |
| FWHM at 2615 keV, keV | 5.0±0.7 | 6.3±0.6 |

Also, the issue of "bright alphas" was confirmed: we again observed several events in $\alpha$ energy region, but with higher light amplitude, than expected (see Fig. 4.22). The discrimination power of two particle bands is ∼12$\sigma$, which is lower than value observed in LSM measurement due to absence of SiO anti-reflective coating on the light detector in LNGS measurement. The radiopurity of both crystals is very high,

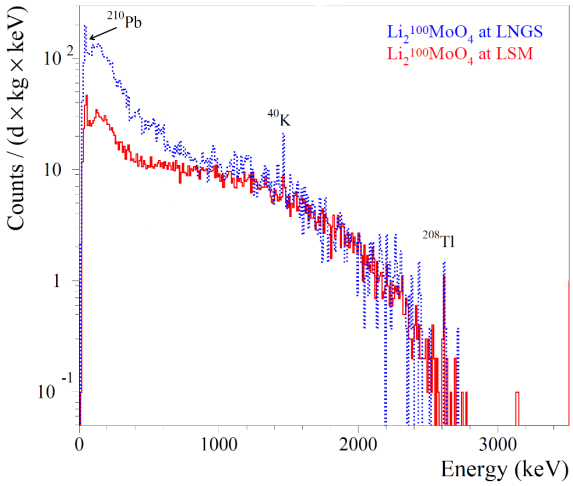


FIGURE 4.21: The background energy spectra of $\gamma(\beta)$ events, measured with two different $Li_2{}^{100}MoO_4$ scintillating bolometers, collected during the runs at LNGS and LSM.

but in case of $^{210}$Po contamination the crystal, cut from the bottom part of the boule has factor 3 lower contamination: ~60 $\mu$Bq/kg versus ~210$\mu$Bq/kg for top of the boule. These values indicate on the depletion of radionuclides in enriched $Li_2MoO_4$ crystals. Thanks to low temperature and stable conditions, we were able to obtain higher energy resolution, than in previous test in LSM. In Tab. 4.4 is shown the comparison of two crystals performance in different set-ups. As these two modules were cut from the same boule, the quality of crystals is expected to be the same. Better energy resolution of LNGS measurement is explained by lower temperature of the measurement.

## 4.3 Four crystal test: run 311

The next step before scaling to the 20-crystal array was the measurement with four enriched crystals to check the uniformity of performance and reproducibility of the previously obtained results on one enriched crystal.

The four crystals, grown in NIIC with the Czochralski technique, were cut from two boules with an average size of ⌀ 44×40 mm and weight ≈ 210 g. The crystals were marked as LMO1t, LMO1b, LMO2t, LMO2b, defining the number of boule (1 or 2) and position in the boule (top or bottom). The LMO1b and LMO1t measurements were described before. The radiopurity of the crystal can depend on the segment of the crystal growth, that is why it is essential to keep the trace on crystal growth.

In addition, two R&D crystals were studied in this run:

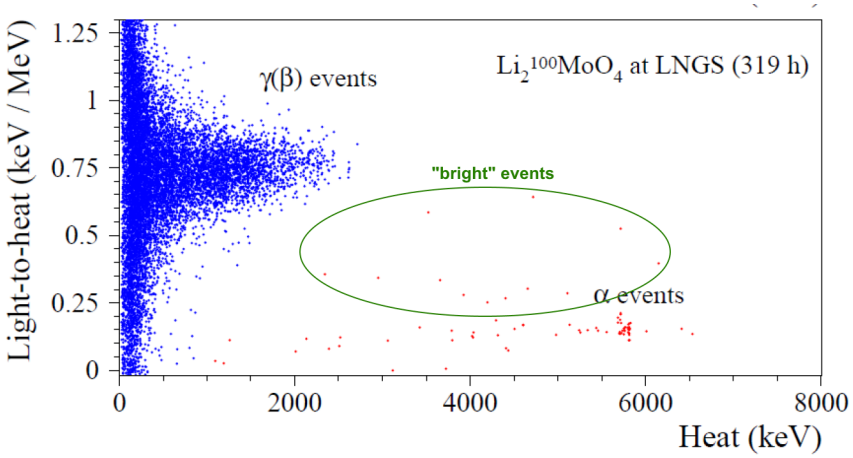


FIGURE 4.22: The Q-plot of $Li_2{}^{100}MoO_4$ background measurement at LNGS.

- Natural $CdWO_4$ to perform precise shape investigation of $^{113}Cd$ $\beta$-spectrum and characterize the crystal as a possible compound for $0\nu2\beta$ decay search of $^{116}Cd$ [104].
- Natural $TeO_2$ crystal 50×50×50 mm with Neganov-Trofimov-Luke light detector to perform measurement with particle identification using Cherenkov light tagging in the framework of CUPID R&Ds [89].

As these two detectors are related to other branches of CUPID R&Ds, studying $^{116}Cd$ and $^{130}Te$ isotopes for $0\nu2\beta$ searches, the results will not be described in this thesis.

### 4.3.1 Design, assembly, and installation

The towers had the same design, as in the previous run for five modules out of six (three per tower). One module, containing cubic $TeO_2$ had a special design due to the crystal shape (see Fig. 4.23).

The cleaning and assembly procedures were the same as in run 310, with one exception: to study better the issue of "bright alphas" and the light collection, two modules with $Li_2{}^{100}MoO_4$ crystals were assembled with reflecting foil (LMO2b, LMO2t), and two were without (LMO1b, LMO1t).

Each crystal was equipped with one NTD and one heater. We could not use two sensors per crystal as in run 310 because the number of available channels was limited. The NTD size was 2.5×3.0×1.0 mm for main crystals and 2.8×1.0×1.0 mm for light detectors. Since light detectors have a much smaller mass, the sensors should have lower heat capacity.

The position in the EDELWEISS cryostat is shown in Fig. 4.24.

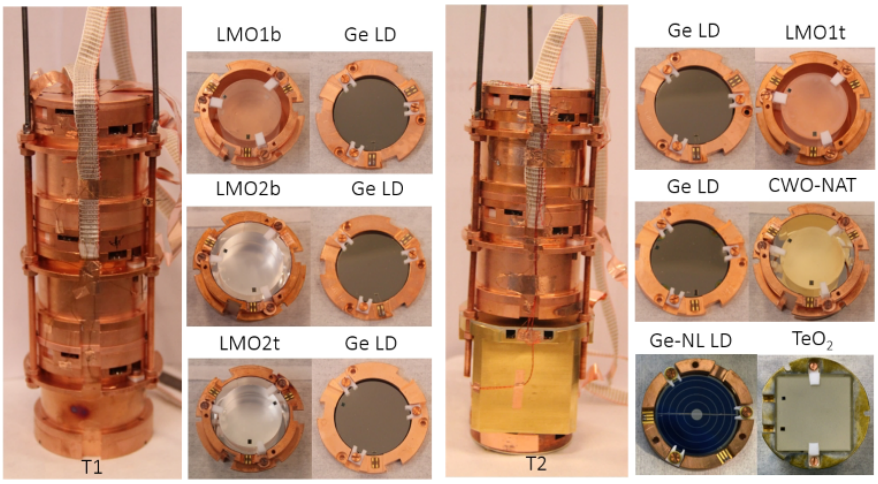


FIGURE 4.23: Assembled tower 1 (left) and tower 2 (right) and their structures.

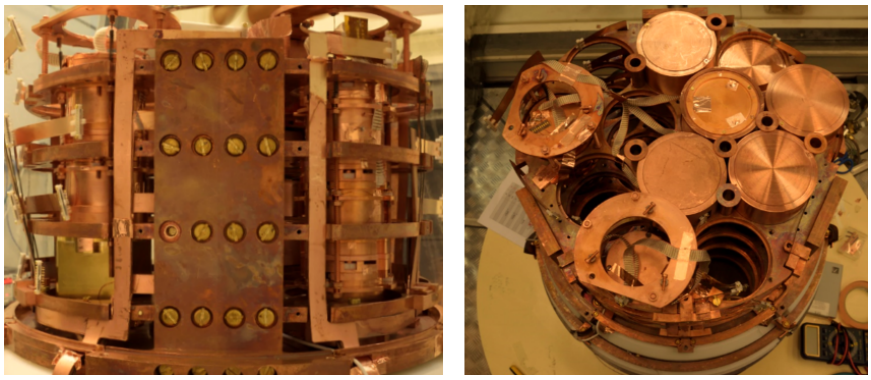

FIGURE 4.24: The two towers installed in the EDELWEISS cryostat together with EDELWEISS detectors, fixed on the galette, side view (left) and top view (right).

### 4.3.2 Results

During the measurements of run 311 we have changed the way of data-taking: instead of triggering, data was collected in a stream, recording all the baseline changes in time. In this way triggering is performed off-line, independently for each channel.

Measurements with a four $Li_2{}^{100}MoO_4$ scintillating bolometer array were highly successful: detectors have demonstrated uniform high energy resolution, high level of radiopurity and full $\alpha/\gamma(\beta)$ separation, meeting the requirements for CUPID-Mo demonstrator (see Table 4.5) [105]. The uniformity of performance had confirmed that this compound is suitable for mass production and use in bigger scale of experiments. With thorium calibration we have obtained the FWHM distribution and estimation of energy resolution in the region of interest (see Fig. 4.25).

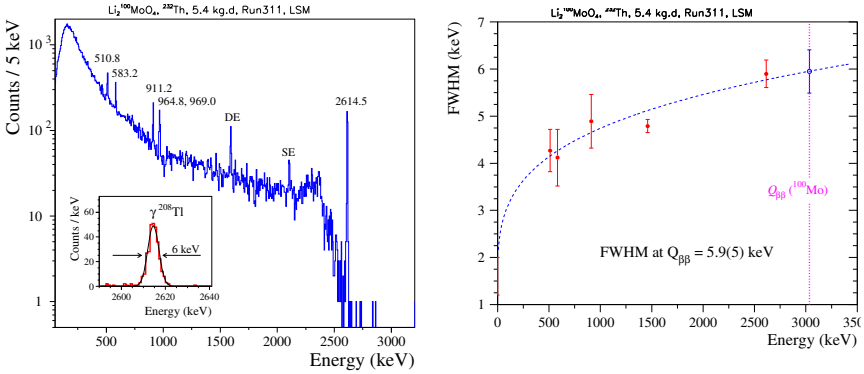


FIGURE 4.25: Energy spectrum of the $^{232}$Th calibration (left) and energy dependence of the FWHM energy resolution (right) measured by a four-bolometer array.

TABLE 4.5: Performance of four $Li_2{}^{100}MoO_4$ scintillating bolometers in run 311.

| | | $Li_2{}^{100}MoO_4$ | crystal # | |
|---|---|---|---|---|
| | 1t | 1b | 2t | 2b |
| Crystal's mass, g | 186 | 204 | 213 | 207 |
| FWHM, keV at 2615 keV | 5.8±0.6 | 5.7±0.6 | 5.5±0.5 | 5.7±0.6 |
| LY, keV/MeV | 0.41 | 0.38 | 0.73 | 0.74 |
| $\alpha/\beta$ separation | $9\sigma$ | $9\sigma$ | $14\sigma$ | $14\sigma$ |
| Activity of $^{228}$Th, $\mu$Bq/kg | $\leq$4 | $\leq$6 | $\leq$3 | $\leq$5 |
| Activity of $^{226}$Ra, $\mu$Bq/kg | $\leq$6 | $\leq$11 | $\leq$3 | $\leq$9 |

### Light yield studies

During run 311 we have tested the possibility to calibrate the light detectors with $^{60}$Co source: its high intensity allows to perform calibration by X-rays, induced from Cu and Mo nuclei with high accuracy (see Fig. 4.26). Thanks to this possibility, the light detectors performance was evaluated. The result is shown in Tab. 4.6. The four light detectors, coupled to $Li_2{}^{100}MoO_4$ crystals, are demonstrating uniform high performance with low baseline noise thank to use of suspended towers. Comparing the behavior of detectors with reflecting foil and

TABLE 4.6: Performance of four Ge light detectors in run 311 at 17 mK.

| Light detector | 1t-LD | 1b-LD | 2t-LD | 2b-LD |
|---|---|---|---|---|
| Signal, $\mu$V/keV | 1.16 | 0.73 | 0.85 | 1.06 |
| $FWHM_{bsl}$, eV | 71(1) | 107(1) | 124(1) | 109(1) |
| FWHM at 17.5 keV, keV | 0.8(1) | 0.51(4) | 0.64(6) | 0.85(9) |
| FWHM, % | ∼4.6 | ∼3 | ∼3.5 | ∼4.8 |

without during the run, we observed twice increased light collection

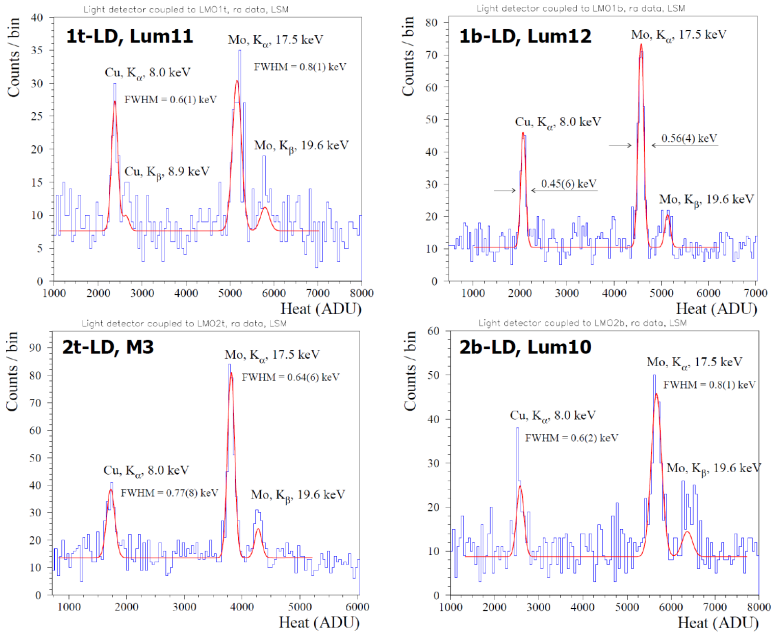


FIGURE 4.26: Spectrum of four light detectors, acquired during the $^{60}$Co calibration at 17 mK.

for crystals with reflecting foil (see Fig. 4.27). However, the $\alpha/\beta(\gamma)$

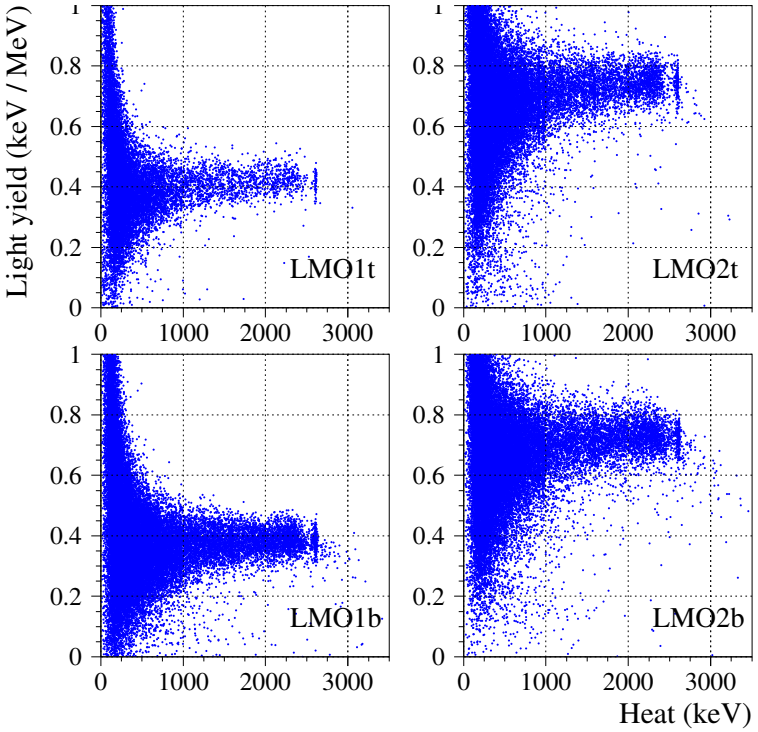


FIGURE 4.27: Q plots of four enriched crystals from thorium calibration. The two detectors on the right, LMO2t and LMO2b were equipped with reflecting foil.

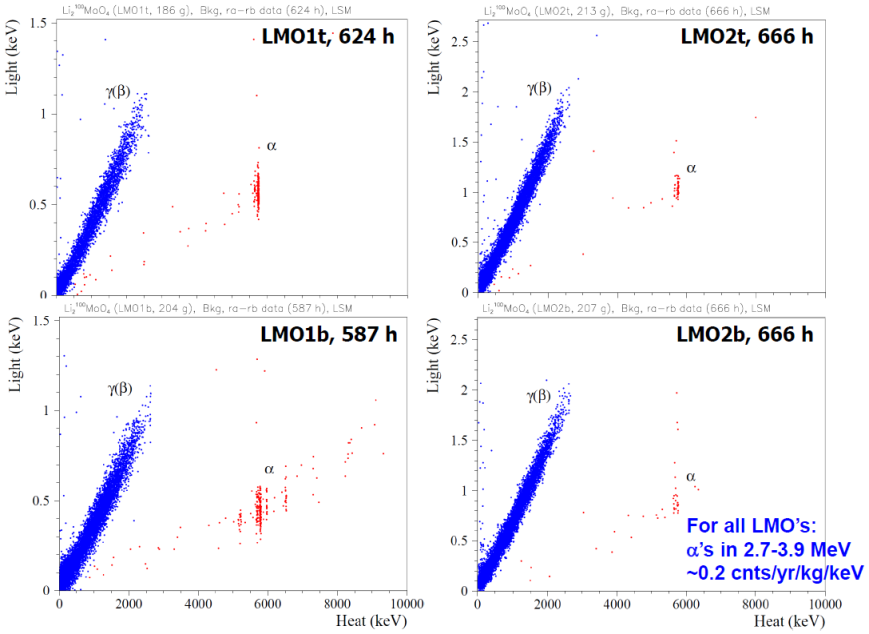


FIGURE 4.28: Scatter plots of four enriched crystals from background measurement. The two detectors on the right, LMO2t and LMO2b were equipped with reflecting foil.

separation is efficient in both cases: the DP, calculated using AmBe calibration (see Fig. 4.29) was at $14\sigma$ with scintillating foil and $9.5\sigma$ without. Due to the possibility to obtain a dangerous background in the region of interest, the decision was taken not to use the reflecting foil in future measurements with scintillating bolometers.

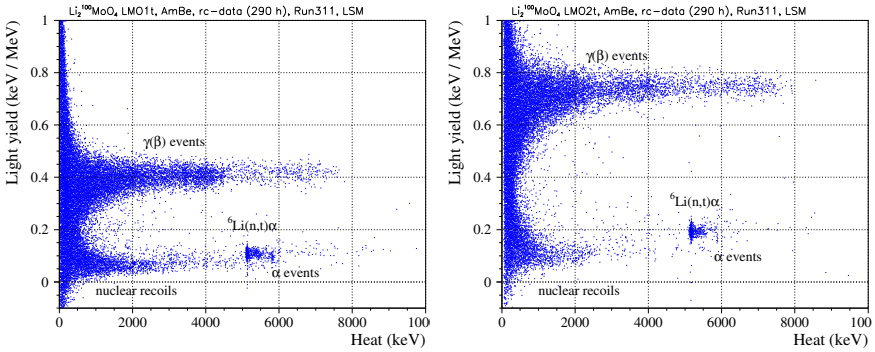


FIGURE 4.29: The Q-plots of LMO1t without reflecting foil (left) and LMO2t with reflecting foil (right), AmBe calibration.

Fig. 4.28 demonstrates the scatter plots collected during background measurements over more than 600 h. The four crystals demonstrate high radiopurity in $\alpha$ region. LMO1b has increased $^{210}$Po activity due to surface contamination. The crystals from the second boule are highly radiopure ($^{210}$Po=0.08-0.02 mBq/kg).

## 4.4 LUMINEU 2$\beta$ investigation

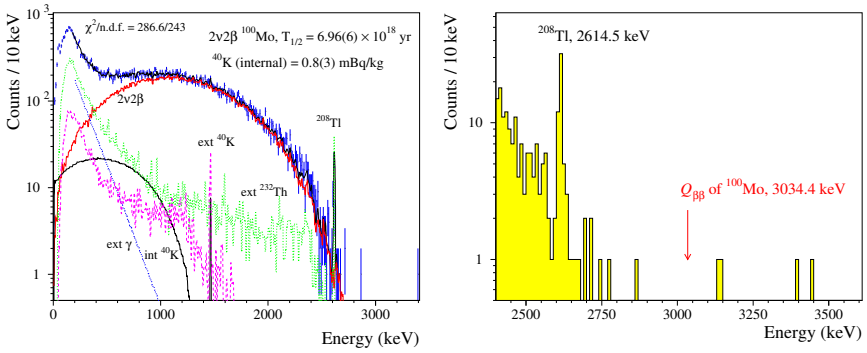


FIGURE 4.30: The $\gamma(\beta)$ energy spectrum (left) accumulated over 0.04 kg×yr with fit by a simple model constructed from a distribution of the $2\nu2\beta$ decay of $^{100}$Mo ($2\nu2\beta$) and other contributions of $\gamma/\beta$ backgrounds. The $2\nu2\beta$ signal-to-background ratio above 1.5 MeV is 10:1. The energy spectrum of ($\gamma$) events in the vicinity of $0\nu2\beta$ decay of $^{100}$Mo extracted from the 0.11 kg×yr background measurements is on the right.

During the measurement of the four crystal array, an accurate investigation of double beta decay was performed (see Fig. 4.30).

The most precise up-to-date $^{100}$Mo $2\nu2\beta$ half-life value was obtained: $T_{1/2}^{2\nu2\beta} = (6.92 \pm 0.06(\text{stat}) \pm 0.36(\text{syst})) \times 10^{18}$ yr with an exposure of $^{100}$Mo of only 0.04 kg×yr [105]. This result is in a good agreement with the value obtained by the NEMO-3 experiment [62]. Regarding $0\nu2\beta$ mode, a few events were registered in the energy region above 2615 keV, but no events have been observed in a 200-keV-wide energy interval centered at the $Q_{\beta\beta}$ of $^{100}$Mo.

The obtained limit on the $^{100}$Mo $0\nu2\beta$ half-life is $T_{1/2}^{0\nu2\beta} > 0.7 \times 10^{23}$ y with an exposure of 0.06 kg×y. This limit is about one order of magnitude weaker than the NEMO-3 result ($1.1 \times 10^{24}$ [75]), however, it was achieved over a factor 600 shorter exposure.

The background level in the region of interest was estimated as 0.06(3) counts/keV/kg/yr, which is higher than required level for demonstrator stage ($10^{-3}$ counts/keV/kg/yr). A precise investigation of possible background sources was performed. The press-fit contacts in the

cryostat, which are used for EDELWEISS detectors were found to contain $^{232}$Th. This isotope is not dangerous for dark matter searches, as they are investigating low energy region, but for double beta decay, the pile-ups of high energy gammas can invade the region of interest. The press-fit contacts in proximity to double beta decay detectors were removed during the preparation to the next measurement for background reduction.

Another possible background source is the muons, as the muon veto in run 311 was not used during the measurement. This issue also was taken into account, and in the demonstrator run it will be exploited.

## 4.5 Conclusions

The LUMINEU project was working on scintillating bolometers development for $0\nu2\beta$ decay search during several years. Within these years the LUMINEU group have obtained impressive results:

- The protocol of crystal growth was developed with the outcome of radiopure, high quality well reproducible crystals.
- The technology of germanium light detectors production and operation with the high performance was developed.
- The production of enriched crystals with available high purity $^{100}$Mo powder (96% enrichment) was established.
- The two compounds: $ZnMoO_4$ and $Li_2MoO_4$ were tested as scintillating bolometers, both natural and enriched crystals.
- Few $Li_2{}^{100}MoO_4$ crystals were produced and tested as bolometers, with excellent performance and reproducibility.

The results, obtained in two runs in EDELWEISS cryostat (run 310 and run 311), are of great importance. The run 310 outcome allowed to take a clear decision on detector compound choice for $0\nu2\beta$ decay search with $^{100}$Mo. The run 311 have confirmed the excellent performance of $Li_2{}^{100}MoO_4$ scintillating bolometers, giving a green light for experiment extension: a demonstrator with few kilograms of $^{100}$Mo.

# Chapter 5

# The CUPID-Mo demonstrator: $0\nu2\beta$ decay search with $^{100}$Mo

The CUPID experiment is a proposed ton-scale "zero-background" experiment with cryogenic bolometers, aiming to reach sensitivity to exploit completely the inverted mass hierarchy region of neutrino masses. CUPID will be based on the CUORE infrastructure and experience, improving the background level and detector performance.

The CUPID interest group have decided to perform multiple R&D activities in order to exploit different technologies and to choose the detectors with best performance and radiopurity for the ton-scale stage of the experiment [76], [77]. The topics of R&Ds can be divided into two main groups: the first is $TeO_2$ bolometers, well-studied crystals in the CUORE framework, but requiring additional improvements to reject alpha background in the region of interest. The second group is studying alternative isotopes ($^{82}$Se, $^{100}$Mo, $^{116}$Cd) using the scintillating bolometer technology (see Fig. 5.1).

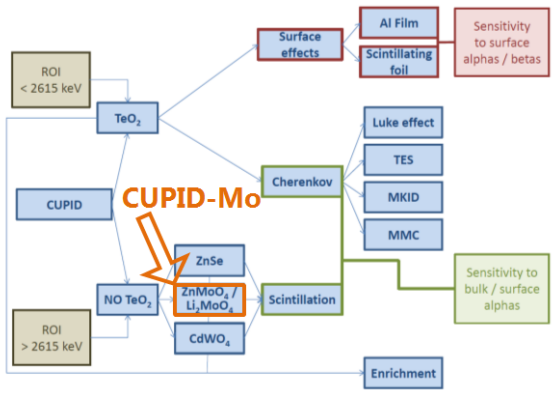


FIGURE 5.1: Scheme of the R&D detector activities for CUPID.

Among these projects there is CUPID-Mo, a proposed demonstrator experiment operating $Li_2^{100}MoO_4$ crystals as scintillating bolometers. The primary goal of this project is to provide the detector technology

with the background and performance suitable for the ton-scale CUPID experiment.

Using the experience provided by the LUMINEU project and described in Chapter 4, the CUPID-Mo demonstrator has started its preparation in 2017 with 20 enriched crystals to be installed and measured in the EDELWEISS set-up. I was deeply involved in CUPID-Mo activities, in particular, I was responsible for detector preparation, held in LAL clean room, which will be described in the following sections.

### 5.0.1 Test of a new tower design

Before scaling to the 20-crystal configuration, a test of a new mechanical structure was performed with four enriched crystals. The new tower design allowed to have four crystals in one tower (instead of three), with light detectors now facing two crystals (light collection from two directions).

Three out of four crystals were measured in a previous run in LSM while one crystal was a new one from the 20 crystal batch.

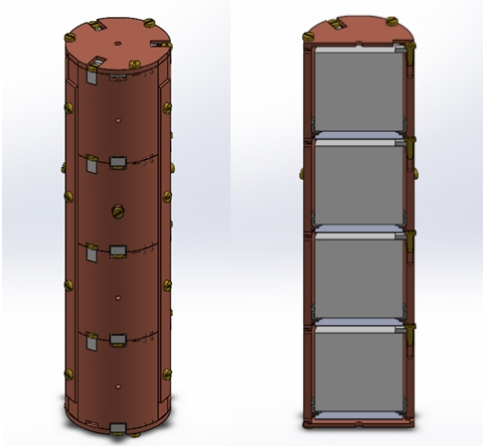

FIGURE 5.2: New test tower design with four crystals and four light detectors.

In this configuration no reflector is used. We have used this test to compare two different types of electrical connections for the NTD: two modules were equipped with copper tubes with gold plating and two with Kapton pads (see Fig. 5.3).

These electrical connections can produce some "heat-only" events in the detectors, that is why it was decided to test two types of electrical connections to check their effect on the "heat-only" signals. An advantage of the copper tubes compared to the Kapton pads is the radiopurity of the material. Even if the amount of material is very small, these contacts are facing directly the crystal so it is important to monitor the contamination in such components. In case of Kapton pads, tin is used for wire soldering. The soldering tin is known to be a

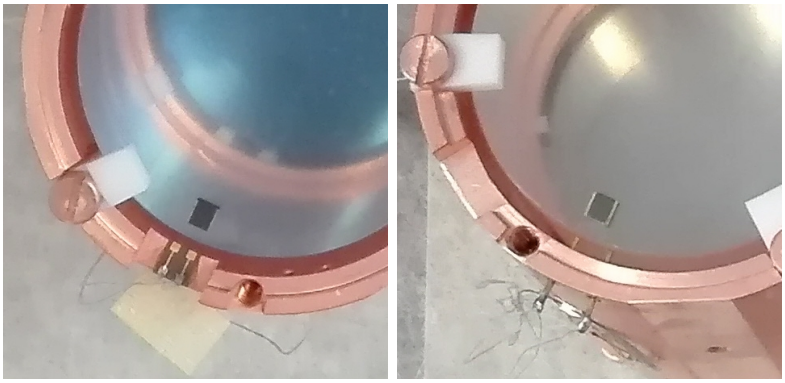

FIGURE 5.3: The two configurations of electrical contacts: Kapton pads on the left and gold-plated copper tubes on the right.

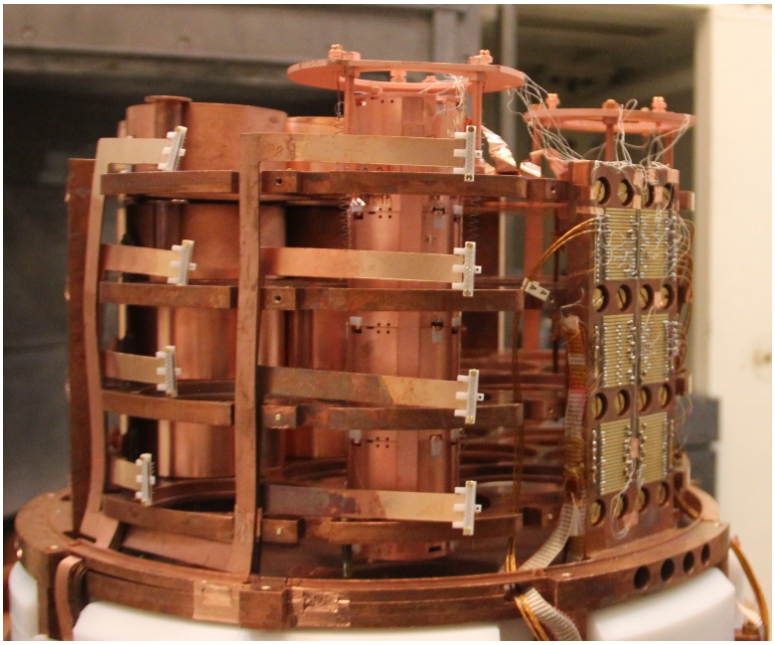

FIGURE 5.4: The tested tower installed in the EDELWEISS cryostat.

material, difficult to purify, due to the lead content used for soldering efficiency.

The measurement was performed during three months, with 527 hours of calibration data and 576 hours of background collected. The summary of detector performance is shown in Tab. 5.1. The FWHM of the 2615 keV line was enlarged with respect to a previous run. This is due to the fact that in run 313 a new thorium source with a higher activity (0.5 kBq of U/Th, while typical detector response 1 second) was used with an impact on the energy resolution of the detectors. For future measurements the source rate will be reduced. No significant issues with mechanical structure were observed.

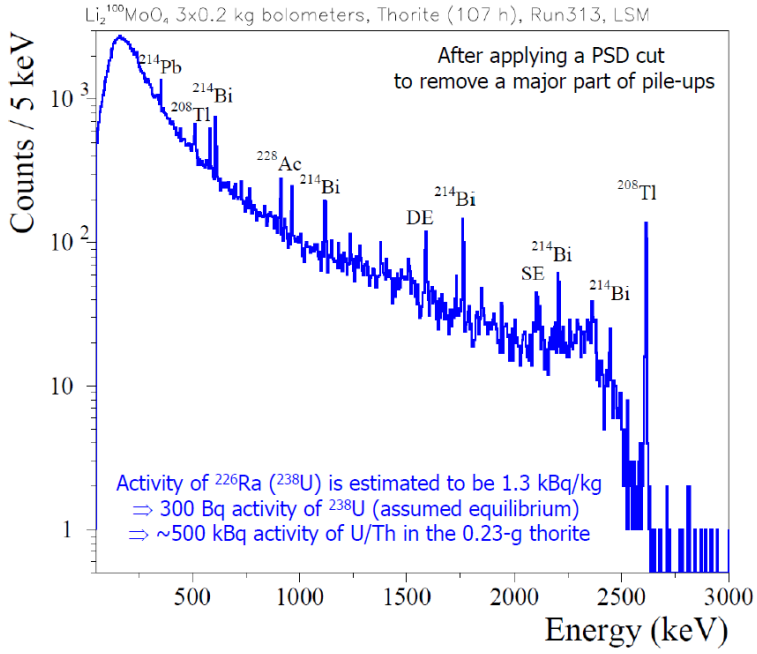


FIGURE 5.5: The total measured spectrum of three enriched crystals with new Th source. The fourth detector was not operational during the calibration run.

TABLE 5.1: Overall performance of $Li_2{}^{100}MoO_4$ scintillating bolometers in run 313.

| Signal, nV/keV | 20-33 |
|---|---|
| Baseline FWHM, keV | 1.1-2.0 |
| FWHM 356 keV, keV | 2.7-3.1 |
| FWHM 2615 keV, keV | 5.6-7.1 |
| Light yield, kev/MeV | 0.4-0.2 |

### Heat-only events studies

"Heat-only" events are the non-particle events with a significant heat signal and no scintillation light. Such events have different shape from particle events and they provide an additional source of background. Heat-only signals are related not to absorber, but to the thermal sensor itself. If there are two sensors on the same crystal, one can distinguish two families of events, corresponding to the sensors, as shown in Fig. 5.6. The origin of such signals is still under investigation, but they are related to the sensors connections.

Thanks to the two available types of electrical connections, an investigation of heat-only events was performed. Such signals do not provide scientific interest, so it is preferable to reduce their rate as much as possible, to avoid pile-up and loses of physical events. In the Fig. 5.7 we show the correlation versus amplitude plots. Both (kapton-induced and

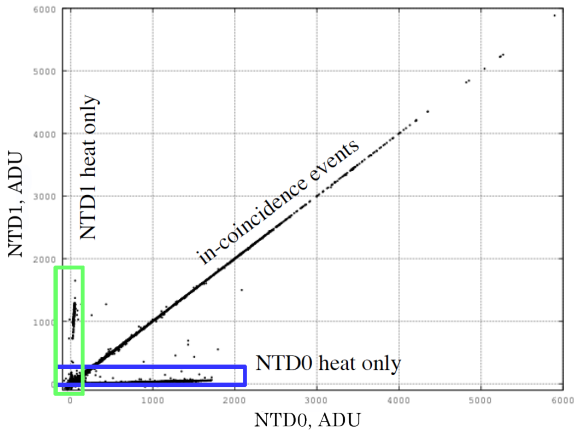


FIGURE 5.6: A scatter plot of pulses amplitudes, recorded by two NTDs on the same absorber.

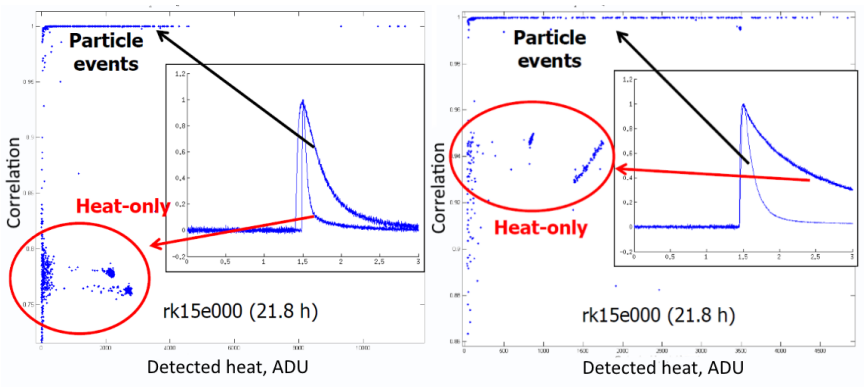


FIGURE 5.7: Heat-only events in two detectors with different types of contacts: Kapton on the left and copper tubes on the right.

tubes-induced) types of heat-only events can be rejected by the correlation parameter, based on comparison of filtered reference pulse and the individual signal, but the rate (shown in Tab. 5.2) is higher in case of Kapton pads.

TABLE 5.2: Rate of heat-only events in the detectors.

| Detectors | | Rate (counts/h) of heat-only events | |
|---|---|---|---|
| | | All | High energy |
| LMO4 | Kapton pads | 11 | 6 |
| LMO3 | | 27 | 11 |
| LMO2 | Copper tubes | 8 | 5 |
| LMO15 | | 10 | 6 |

The decision to use the connection type with the smaller rate of heat-only events (copper tubes) was taken for the next phase of the experiment. However, the origin and the physical model of this kind of events has to be further investigated.

## 5.1 CUPID-Mo preparation

The preparation of the demonstrator with 20 enriched crystals included the realization of new design, sensors gluing, cleaning of detector elements, assembly of detectors and installation in the cryostat. Several changes were applied to these procedures with respect to previous experience in order to obtain high radiopurity level and good detectors performance.

The 20 enriched crystals for the demonstrator were produced in NIIC, Novosibirsk, with the developed procedure of high quality crystal growth (see Chapter 4). Shipping to Orsay, France, was done by ground transportation and before the assembly activities the crystals were stored in LSM underground laboratory under nitrogen flux to avoid cosmogenic activation and radon contamination of the crystals.

The high-purity Ge wafers for light detectors production were purchased from UMICORE. The anti-reflective layer deposition was performed in CSNSM, the Ge wafers were coated with SiO 70 nm layer on both sides, as now each light detector will face two crystals.

### 5.1.1 20 detectors assembly

For the assembly of 20 scintillating bolometers, we have profited of the experience obtained in R&D runs to improve the design and to have a compact structure in the cryostat.

The basic components for the assembly of one module are shown in Fig.5.8. The mechanical support is provided by a copper holder, which acts as well as a heat sink. The holders for CUPID-Mo were designed in SPEC (CEA), fulfilling the following requirements: compact structure and simple procedure of assembly. The copper elements were produced out of NOSV copper with high radiopurity. The pieces were realized by the mechanical workshop of LAL (Laboratoire de l'Accélérateur Linéaire, Orsay). The crystal is fixed with PTFE elements and contacts for bonding wires are provided by copper tubes (provided by goodfellow [106]) with a gold coating (bonding on top for one side and crimping of wire on the other side). The used NTDs were provided by Lawrence Berkeley National Laboratory, type 41B ($T_0$=3.8 K, $R_0$=1.5 Ohm). The NTD size was 3.0×3.0×1.0 mm for those glued to $Li_2{}^{100}MoO_4$ crystals while 3.0×1.0×0.5 mm for the light detectors. We have reduced their size by a factor six with respect to NTDs on crystals to boost the sensitivity.

### 5.1.2 Cleaning procedure of holder elements

As surface contamination give a significant contribution to the total background, a special cleaning procedure was established to clean the copper pieces:

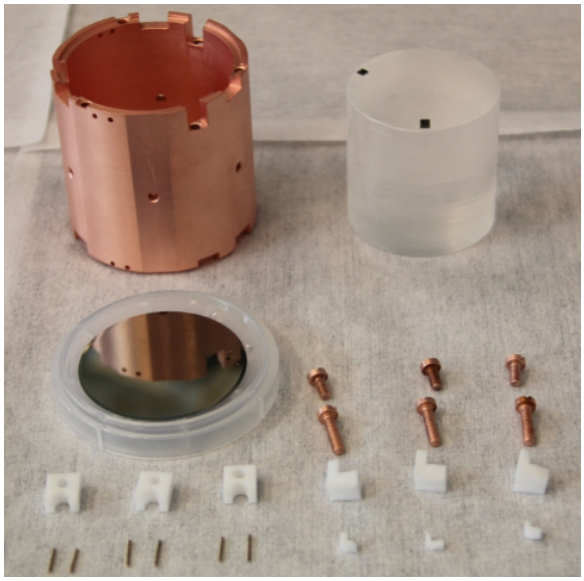

FIGURE 5.8: All components required to assemble one module: copper holder, crystal with NTD and heater, light detector with NTD, copper screws, PTFE spacers, copper tubes with gold plating for contacts.

FIGURE 5.9: On the left: cleaned holders in the oven during the drying. On the right: cleaning with citric acid in the ultrasonic bath.

- Pre-cleaning and removing of the grease with the soap: ultrasonic bath at 40-50 $^o$C with ultrapure water and 5% of micro-90 cleaning solution(about 10-20 min).
- Rinse with ultrapure water.
- Citric acid (1): ultrasonic bath at 40-50 $^o$C with ultrapure water, 4%±2% of citric acid and 0.5-2% of hydrogen peroxide and the amount depends on the solution temperature (the hotter the solution, the smaller is the needed quantity of $H_2O_2$).

- This operation lasts about 30-45 min. An indicator for the end of the procedure should be the changing of the solution color from blue to green, meaning that about 10-20 $\mu$m have been removed. However, this color changing depends on the amount of solution with respect to the surface to wear away.
- Rinse with ultrapure water.
- Citric acid (2): everything as in Citric acid (1), but this step lasts about 15 min and removes about 3-5 $\mu$m.
- Rinse with ultrapure water.
- Wipe with kim-wipes.
- Drying of the copper pieces is performed in an oven at 60-80 $^o$C for about one hour.
- The cleaned pieces have to be kept under nitrogen or oxygen to avoid repeated contamination.

The cleaning procedure was performed in clean room of class 1000 in LAL (see Fig. 5.9).

Before and after the cryogenic runs, the enriched crystals are kept under $N_2$ flux in LSM to avoid cosmogenic activation [107] and $Li_2{}^{100}MoO_4$ crystals have been brought to sea level only to perform the assembly of the detectors.

### 5.1.3 Gluing procedure

The glue chosen for thermistor coupling is a two-component Araldite glue, used for its high radiopurity and density, suitable for NTDs gluing. The gluing procedure established for 20 crystals foresees nine spots for each NTD and one spot for each heater.

The gluing was performed with a special tool also used for CUPID-0. The NTD is kept at the place by a small pump. The middle part of the tool, which keeps the NTD, can be moved in Z axes, and fixed at any level. The metallic cap has a 50 $\mu$m step, which allows to fix the NTD surface on this distance from the outer "ring" of the tool, which after keeps the crystal (see Fig. 5.10). The metal spacer allows to obtain the 50 $\mu$m distance between the NTD and the crystal surface. This distance is very important to obtain separate glue spots, as the quality of gluing can strongly affect the performance of the bolometer. As five out of twenty crystals were used in R&D measurements, the glued NTDs were not removed and the six-spots gluing was kept. For the new fifteen crystals, the gluing procedure with the nine spots was performed, see Fig. 5.11.

The coupling of NTDs to the light detectors was also performed with Araldite glue, but instead of spots matrix we have obtained a veil of glue, as the thermal contraction is not a problem for Ge-Ge

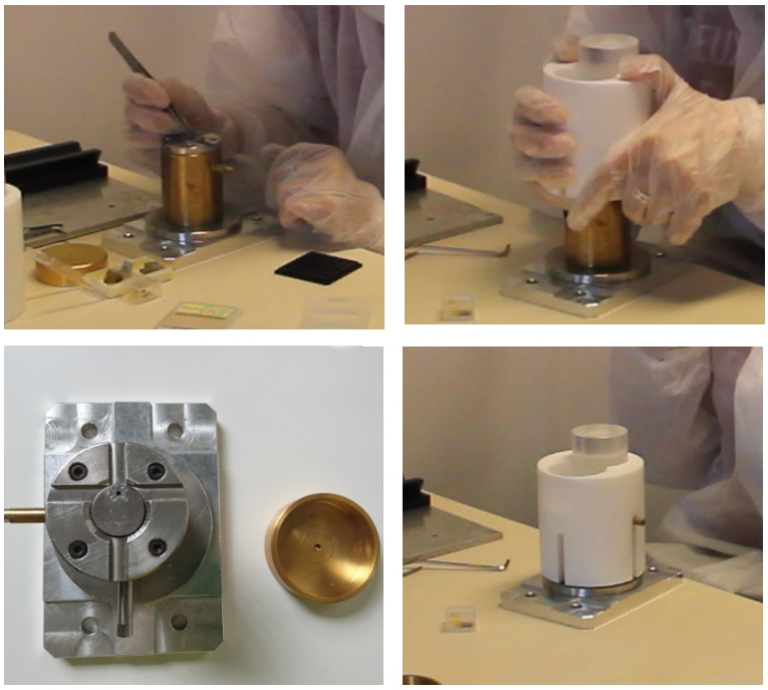

FIGURE 5.10: The tool for gluing (left bootom) together with the cap to provide 50 $\mu$m gap. On three other photos is shown the process of gluing: NTD placement (top left) and placing of the crystal (right).

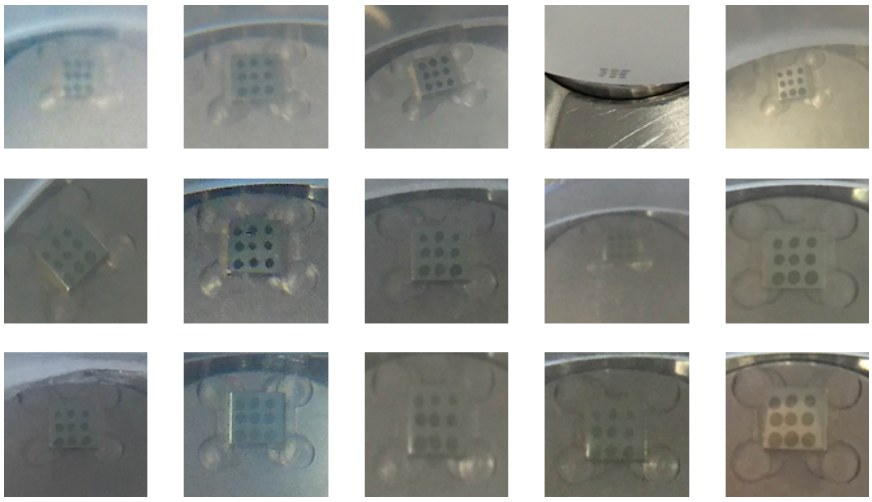

FIGURE 5.11: Glue spots between NTD and crystal, photos of 15 crystals.

connection (see Fig. 5.12). The gluing procedure is hand-operated, the NTD was pressed on the light detector surface with manipulator of bonding machine to control the force.

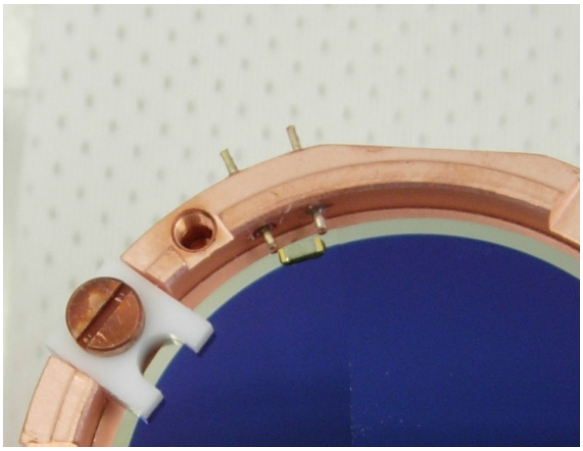

FIGURE 5.12: An NTD, glued on the light detector. The coated part of light detector has blue color, NTD is attached to not coated part.

### 5.1.4 Assembly

After all the elements are cleaned, and the crystal and light detector are coupled to the NTDs, the assembly was performed in the clean room class 10 in LAL. The absorber is fixed inside the cavity with PTFE elements on top and bottom (with 120 degree symmetry). The light detector is held by three PTFE elements (see Fig. 5.13). Four crystals are assembled then in a tower. No reflecting foil is used in this configuration due to the danger of having "bright alphas" (as described in Chapter 4).

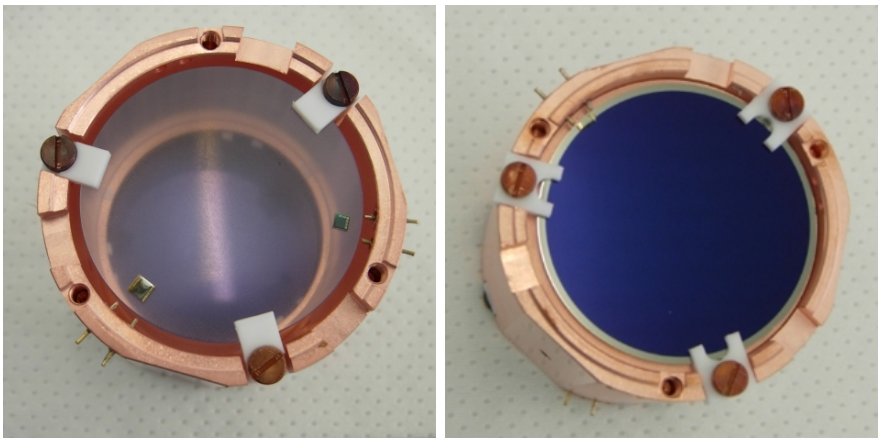

FIGURE 5.13: One assembled detector module with $Li_2{}^{100}MoO_4$ crystal on the left and the Ge light detector with SiO coating on the right.

The copper tubes for electrical contacts were fixed on the holder with the Araldite glue. The bonding of the detectors was performed in

clean room with ball bonding technique with 25 $\mu$m gold wire (see Fig. 5.14).

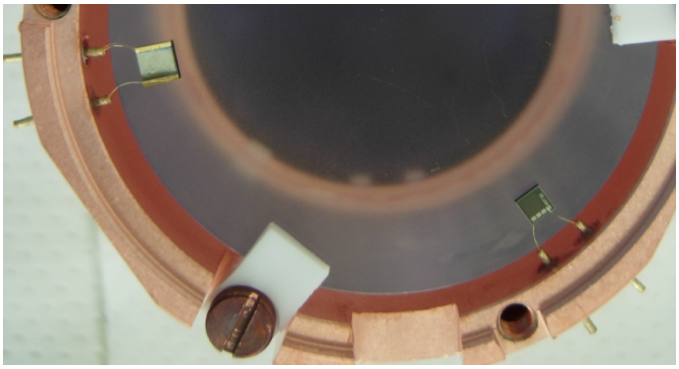

FIGURE 5.14: The NTD sensor and heater with gold bonding on the gold-plated tubes for electrical connection

### 5.1.5 Wiring

Electrical connections were provided by the silk-covered constantan twisted wires. To avoid the use of soldering close to detectors, wires were crimped in the golden tubes on the detector side while soldered on the Kapton, glued on the top of each tower (see Fig. 5.15). The total mass of used soldering was evaluated for future Monte Carlo simulations of the set-up: 1.2±0.1 g on the towers, which gives ≈0.2 Bq of $^{210}$Po activity. On the top of each tower a Kapton with golden contacts

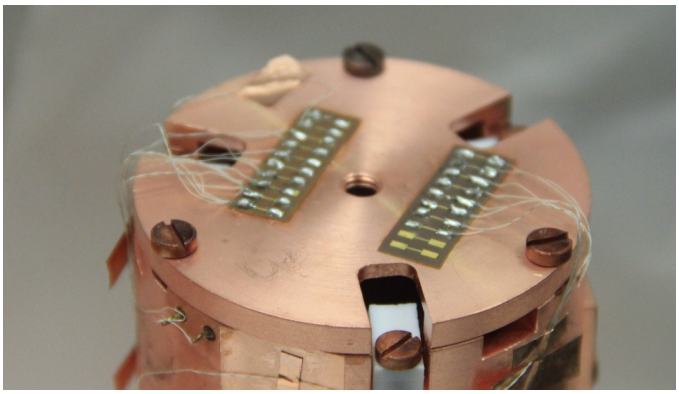

FIGURE 5.15: The wire connection from each detector to the top of the tower.

is glued. On this Kapton are soldered the constantan wires (connection to the detectors) on one side and copper wires, connected to the electronics through the copper plate inside the EDW cryostat on the other side (see Fig. 5.16). Such connection is replacing the press-fit contacts

of EDELWEISS detectors, used in previous runs, as they were found to be contaminated by thorium.

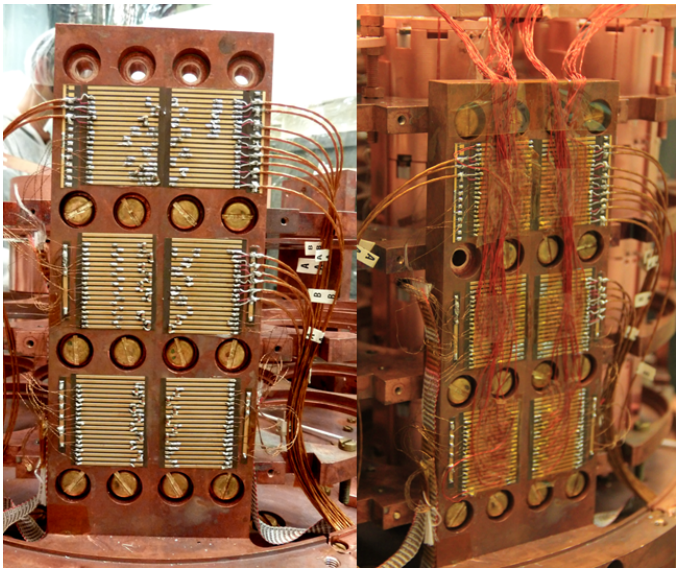

FIGURE 5.16: The Kapton plate for CUPID-Mo channels before the installation of the five towers on the left and after on the right.

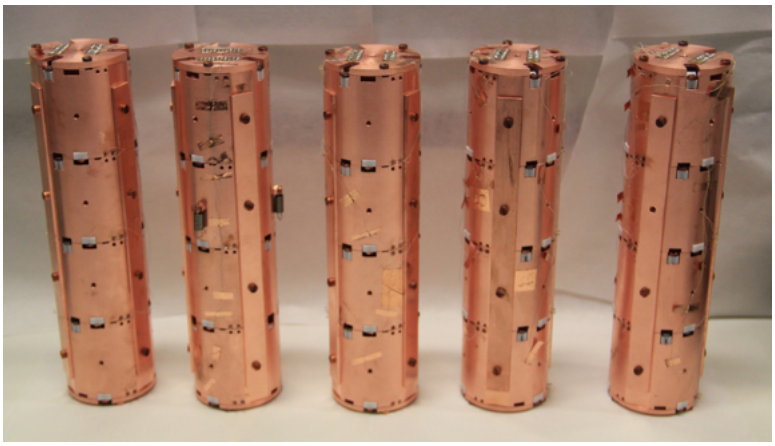

FIGURE 5.17: The 20 crystals, assembled in 5 towers before the installation in the cryostat.

A summary on CUPID-Mo detectors is presented in Tab. 5.3.

### 5.1.6 Installation in the cryostat

In order to suspend th five towers inside the EDELWEISS cryostat, a special "half-galette" piece was produced to hold them. The five towers were installed one by one by sliding the tower through the holes in the galette, and after fixing the suspension (see fig. 5.18). Each tower is

TABLE 5.3: Summary of Cupid-Mo detectors features in the EDELWEISS cryostat.

| Crystal ID | Size, mm | Weight, g | NTD type | LD ID | Tower position |
|---|---|---|---|---|---|
| LMO1 | ∅43.6×40.0 | 185.86 | 34C | LD1 | A10 |
| LMO2 | ∅43.6×44.2 | 203.72 | 34C | LD17 | D11 |
| LMO3 | ∅43.9×45.6 | 212.61 | 34C | GeCo2B | C11 |
| LMO4 | ∅43.9×44.5 | 206.68 | 34C | LD18 | B11 |
| LMO5 | ∅43.8×45 | 211.10 | 41B | LD5 | D3 |
| LMO6 | ∅43.8×45 | 209.19 | 41B | LD6 | C3 |
| LMO7 | ∅43.8×45 | 210.45 | 41B | LD7 | B3 |
| LMO8 | ∅43.8×45 | 209.71 | 41B | LD8 | A3 |
| LMO9 | ∅43.8×45.3 | 209.3 | 41B | LD9 | D4 |
| LMO10 | ∅43.8×45.3 | 208.90 | 41B | LD10 | C4 |
| LMO11 | ∅43.8×45.3 | 208.18 | 41B | LD11 | B4 |
| LMO12 | ∅43.8×45.4 | 209.98 | 41B | LD12 | A4 |
| LMO13 | ∅43.8×45.5 | 210.35 | 41B | LD19 | D12 |
| LMO14 | ∅43.8×44.5 | 205.76 | 41B | LD14 | B10 |
| LMO15 | ∅43.7×45.2 | 209.50 | 41B | LUM11 | A11 |
| LMO16 | ∅43.8×45 | 208.96 | 41B | LD16 | C10 |
| LMO17 | ∅43.8×45.3 | 209.20 | 41B | LD2 | D10 |
| LMO18 | ∅43.8×45.3 | 210.09 | 41B | LD3 | C12 |
| LMO19 | ∅43.8×45.3 | 209.16 | 41B | LD4 | B12 |
| LMO20 | ∅43.8×45.3 | 209.7 | 41B | LD15 | A12 |

suspended on three stainless steel springs with 0.5 mm diameter of wire and load of 10 N.

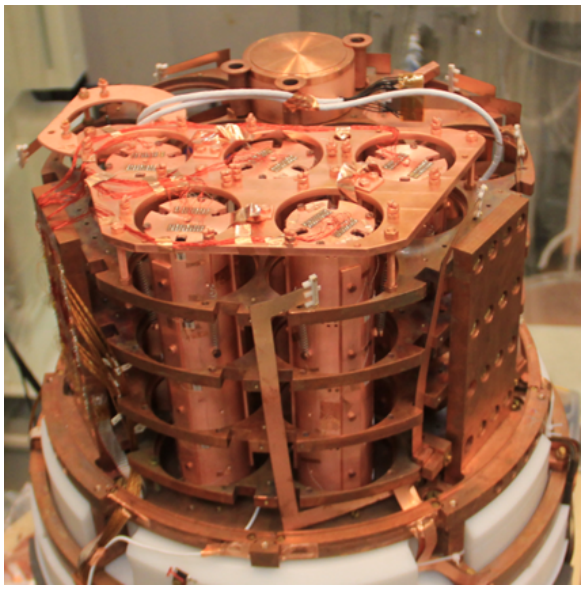

FIGURE 5.18: The five towers, installed in the EDELWEISS cryostat.

## 5.2 CUPID-Mo prospects

The CUPID-Mo experiment have started its first phase with 20×0.21 kg $Li_2{}^{100}MoO_4$ (2.34 kg of $^{100}$Mo) scintillating bolometers in the EDELWEISS set-up. The detectors assembly was performed in fall 2017 and the installation in the cryostat was done in February 2018. Unfortunately, due to several cryogenics problems it was impossible to start the measurement in spring 2018 and the cooling down was postponed to summer 2018. The first measurements have started in July 2018. The first run will aim at 6 months of data-taking with the following goals:

- Confirm the $Li_2{}^{100}MoO_4$ technology viability and stable performance on a larger scale.
- Obtain "zero-background" ($b \leq 10^{-3}$ counts/keV/kg/yr) in the ROI.
- Improve the existing sensitivity to the $^{100}$Mo $0\nu2\beta$ decay.

If the required background level will be achieved after six months of data-taking, we plan to extend the measurement in order to increase the sensitivity.

As $Li_2{}^{100}MoO_4$ scintillating bolometers were chosen as primary technology [108] for CUPID experiment, it was decided to start the development of CUORE-like demonstrator with $Li_2{}^{100}MoO_4$ crystals as second phase of CUPID-Mo experiment. Phase II is a follow-up with additional 26 enriched and 2 natural crystals of cubic shape (45×45×45 mm). Such geometry provides more efficient utilization of space in the cryostat and fits CUORE design with minor changes (addition of light detectors in new towers). Phase II will start from measurement with four $Li_2{}^{100}MoO_4$ scintillating bolometers in LNGS Hall-C cryostat, to test the new tower structure and performance. In case of positive outcome, the full-size demonstrator will be installed in Hall-A cryostat (currently hosting CUPID-0 demonstrator with $Zn^{82}Se$ bolometers, see Chapter 6) in 2019.

The expected sensitivity of CUPID-Mo demonstrators is shown in Fig. 5.19 and reported in Tab. 5.4. The sensitivity estimation is provided for the two possible background indices: $b$=$10^{-2}$ counts/keV/kg/yr or $b$=$10^{-3}$ counts/keV/kg/yr in the ROI (10 keV window centered at $Q_{\beta\beta}$) and 70% efficiency. The efficiency of the pulse shape discrimination is set to be 95%. A python library was used for the calculations, using the nuclear matrix elements, calculated with following models: IBM2, QRPA and EDF [109]. The importance of pulse-shape analysis arises for the ton-scale $^{100}$Mo experiment, as the rate of $2\nu2\beta$ decay for this isotope is one of the highest among $2\beta$-active nuclei [59]. It should be noted that the sensitivity of the demonstrators remains almost the same even in case of one order of magnitude worse background.

In spite of the small scale of the CUPID-Mo experiment, this demonstrator can achieve results comparable with leading big-mass $0\nu2\beta$ decay experiments, providing the best limit on $0\nu2\beta$ decay half-life of

TABLE 5.4: Projected CUPID-Mo performance with the background counting rate $b$=$10^{-2}$counts/keV/kg/year and $b$=$10^{-3}$counts/keV/kg/year in the ROI (10 keV window centered at $Q_{\beta\beta}$).

| | Exposure, kg×yr | $b$=$10^{-2}$counts/keV/kg/year | | $b$=$10^{-3}$counts/keV/kg/year | |
|---|---|---|---|---|---|
| | | $\lim T^{0\nu}_{1/2}$, yr | $\langle m_{\beta\beta}\rangle$, eV | $\lim T^{0\nu}_{1/2}$, yr | $\langle m_{\beta\beta}\rangle$, eV |
| Phase I, LSM 20 cryst×0.21 kg | 1.2 | $1.3\times10^{24}$ | 0.35-0.58 | $1.3\times10^{24}$ | 0.34–0.58 |
| | 2.4 | $2.5\times10^{24}$ | 0.25–0.42 | $2.6\times10^{24}$ | 0.24–0.41 |
| | 12 | $1.0\times10^{25}$ | 0.13–0.21 | $1.3\times10^{25}$ | 0.11–0.19 |
| Phase II, LNGS 26 cryst×0.28 kg | 2 | $2.2\times10^{24}$ | 0.27–0.45 | $2.3\times10^{24}$ | 0.26–0.44 |
| | 4 | $4.1\times10^{24}$ | 0.19–0.33 | $4.6\times10^{24}$ | 0.18–0.31 |
| | 20 | $1.5\times10^{25}$ | 0.1–0.17 | $2.2\times10^{25}$ | 0.08–0.14 |

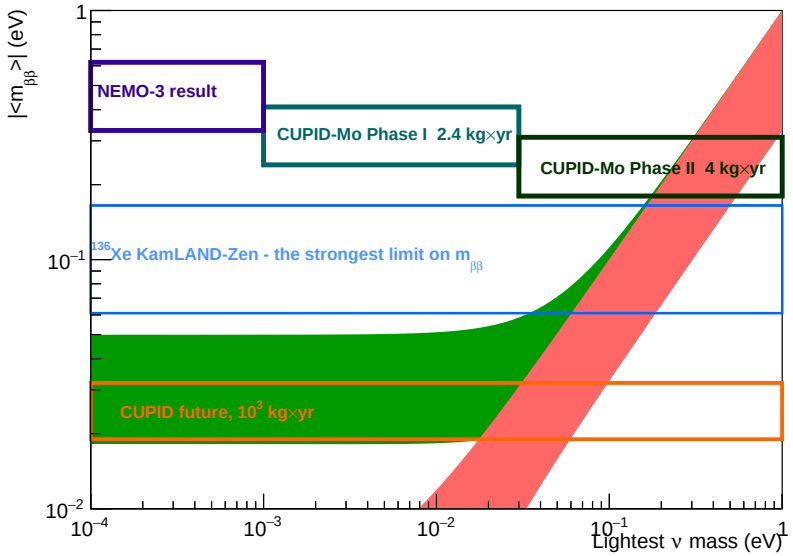


FIGURE 5.19: The effective Majorana mass as function of the lightest neutrino mass. The NEMO-3 limit on $^{100}$Mo and projected sensitivity of CUPID-Mo demonstrators is shown, as well as the strongest current limit on $\langle m_{\beta\beta}\rangle$ from KamLAND-Zen experiment and projected sensitivity of ton-scale CUPID experiment.

$^{100}$Mo. As shown on the Fig. 5.19, in one year of measurement both CUPID-Mo demonstrators would improve the most stringent limit on $T^{0\nu2\beta}_{1/2}$ of $^{100}$Mo.

## 5.3 Conclusions and perspectives

The CUPID-Mo experiment is ongoing with promising perspectives. $^{100}$Mo is considered as one of the most suitable isotopes for the ton-scale cryogenic experiment. The $Li_2{}^{100}MoO_4$ scintillating bolometers

were chosen as the baseline technology for the first stage of the CUPID experiment [108].

With the outcome of CUPID-Mo phase I and phase II, obtained experience will be used for preparation of future ton-scale $0\nu2\beta$ decay cryogenic experiment. The discrimination of $\alpha$ background gives possibility to obtain "zero-background" in the region of interest for ton-scale experiment. The CUPID experiment configuration is under discussion. Using $Li_2{}^{100}MoO_4$ scintillating bolometers, the CUORE cryostat will be able to host ∼300 kg of $^{100}$Mo. The estimated sensitivity to $\langle m_{\beta\beta} \rangle$ for exposure of $10^3$ kg×yr (i. e. after ∼3 years of data-taking) is 20-30 meV, which allows to cover completely the inverted mass hierarchy (see Fig. 5.19). Such cryogenic experiment will be highly competitive with other ton-scale experiments thanks to high energy resolution and powerful background rejection.

# Chapter 6

# CUPID-0 demonstrator: $0\nu2\beta$ decay search with $^{82}$Se

In the framework of CUPID R&Ds, CUPID-0 investigates the $2\beta$-decay of $^{82}$Se, using the scintillating bolometer technique. The Q-value of $^{82}$Se is 2998 keV, which is higher than the end-point of natural $\gamma$-radioactivity background. Such high energy allows obtaining a very low background in the region of interest. The alpha background can be suppressed thanks to particle discrimination by the scintillation light. Due to the low natural abundance (8.73%), the enrichment of material is required to obtain a high sensitivity of the experiment.

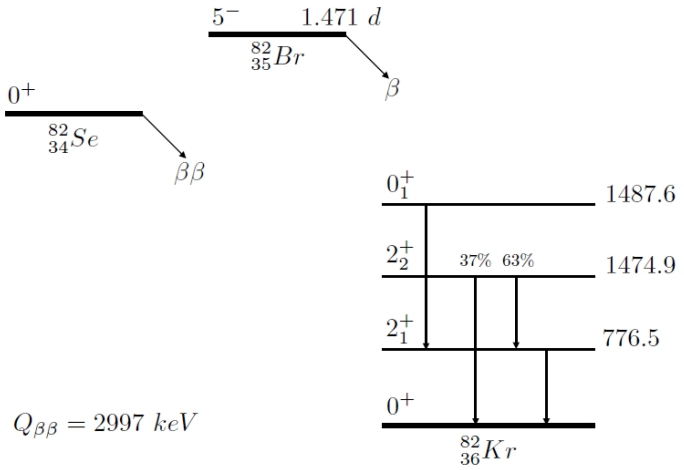


FIGURE 6.1: The double beta decay scheme of $^{82}$Se to the ground and excited states of $^{100}$Kr [110].

CUPID-0 aims to provide a technology that meets CUPID requirements for a ton-scale experiment concerning the background and detector performance. The project was divided into two phases:

- Phase I: a short test run with three Zn$^{82}$Se crystals to test the assembly line, verify performance and radiopurity of the crystals.

- Phase II: long demonstrator measurement with 27 crystals with the goals to obtain "zero-background" in the ROI and improve the sensitivity to $0\nu2\beta$ decay of $^{82}$Se.

The scintillating crystals for the CUPID-0 demonstrator were developed in the framework of the LUCIFER project [111]. The enriched $^{82}$Se was produced by gas centrifugation at URENCO, Stable Isotope Group in Almelo, in the Netherlands [110]. The 15 kg of enriched metal contained >95% of $^{82}$Se. The Zn$^{82}$Se crystals are grown from the melt, in graphite crucibles using the Bridgman technique at the Institute for Scintillation Materials, National Academy of Sciences of Ukraine (ISMA Kharkiv, Ukraine). The main difficulties faced during the crystal growth are connected to the high melting point (1525 °C) and to the control of crystal purity. The irrecoverable losses of the material during crystal growth were reduced down to 2% [112].

In the framework of CUPID-0 I was actively participating in preparation of light detectors with SiO deposition, realized in CSNSM laboratory and detector assembly, which was performed in Gran-Sasso underground laboratory, in the DarkSide clean room (described in details in following sections).

## 6.1 Test with three crystals

The crystals were assembled in a tower with three Zn$^{82}$Se crystals and four light detectors, where each crystal is facing two light detectors: on top and bottom (see Fig. 6.2). The light detectors are Ge thin bolometers with a SiO coating, realised at CSNSM (Orsay, France). Each crystal is wrapped in a 3M VM2002 reflecting foil. Such assembly minimised the amount of material, surrounding the detectors. This minimization is important for external background reduction, even if all used materials are highly radiopure [113].

As sensors, NTDs of two different dimensions have been used: 2.8×3.0×1.0 mm for ZnSe crystals and 2.8×2.0×0.5 mm for light detectors due to the difference in heat capacity for the two types of absorbers.

Detectors have been assembled in a clean room environment aboveground in LNGS laboratory. The bolometric measurement was performed in the dilution refrigerator located in Hall C of LNGS (for cryostat description see Appendix A). The data-taking was performed with stabilization at 20 mK temperature. The Zn$^{82}$Se crystals were permanently irradiated by smeared $\alpha$ sources of $^{147}$Sm (with the $Q$ value of 2.3 MeV) to perform the $\alpha/\gamma(\beta)$ particle discrimination with a short exposure. The obtained data were processed off-line using optimal filter algorithm. The $\gamma$ energy calibration was performed using $^{228}$Th and $^{40}$K sources. The energy resolution in the ROI was estimated using a fit with the following function:

$$FWHM^2(E) = FWHM^2_{baseline} + \alpha E^{\beta} \tag{6.1}$$

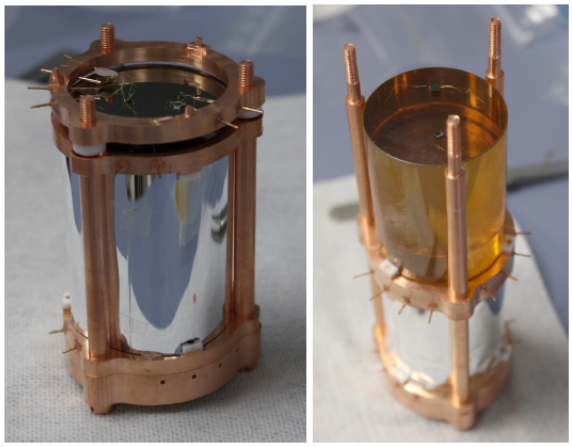

FIGURE 6.2: The tower during assembly: on the left: $Zn^{82}Se$ bolometer, surrounded by a reflecting foil and coupled to two light detectors on top and bottom. Right: the second $Zn^{82}Se$ crystal is placed on top of the light detector during the assembly [113].

where $\alpha$ and $\beta$ are fit coefficients and $FWHM_{baseline}$ is the contribution of the electronics noise. The fit result is shown in Fig. 6.3. Even though the energy resolution is 3 times larger than the expected value for the experiment (10 keV FWHM [114]), the $Zn^{82}Se$ bolometers fulfill the requirements for the CUPID-0 demonstrator, allowing to reach "zero-background" level thanks to particle identification.

The $Zn^{82}Se$ crystals have shown a unique property: the amount of light, emitted by alpha particle interactions is higher than in case of $\gamma/\beta$: $LY_{\alpha}$=9.1–14.1 keV/MeV, $LY_{\gamma/\beta}$=3.3–5.2 keV/MeV. Even if light yield allows to discriminate the different kinds of particles, if part of the light amplitude is lost (due to scattering, reflection, etc.), the $\alpha$ signals can diffuse in the ROI. Due to this fact, the light pulse shape is used for particle rejection: the light pulses of $\gamma/\beta$ events are slower than signals produced by $\alpha$ events of the same energy (see Fig. 6.4). The shape-sensitive parameter is calculated as follows:

$$SP = \frac{1}{A\omega_r}\sqrt{\sum_{i=i_M}^{i_M+\omega_r}(y_i - As_i)^2} \tag{6.2}$$

where $y_i$ is the pulse, $A$ and $i_M$ its amplitude and maximum position, $s_i$ the mean signal pulse scaled to unitary amplitude and aligned to $y_i$, $\omega_r$ the right width at half maximum of $s_i$. The average discrimination power (DP) at $Q_{\beta\beta}$ of $^{82}Se$ for three crystals is $11\sigma$.

As $\alpha$ particles have a very short range, it is possible to obtain an indication of the position of the contamination: bulk or surface. If the $\alpha$-active nuclei is located in the crystal bulk, the energy of the decay is completely absorbed by the bolometer, giving a signal with energy

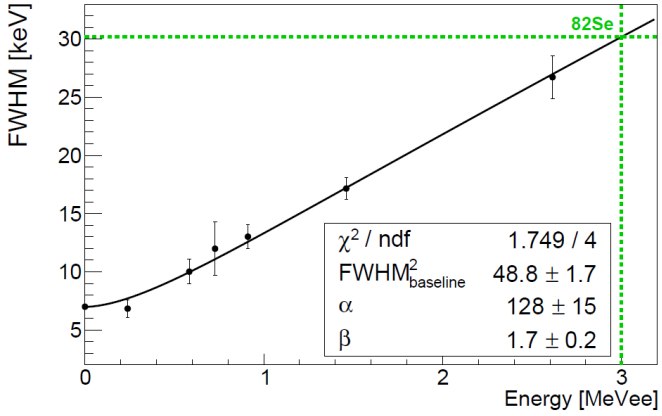


FIGURE 6.3: FWHM energy resolution as a function of the energy ($Zn^{82}Se$-1) for the most intense peaks produced by $^{228}Th$ and $^{40}K$ sources. The green dotted lines indicate the $^{82}Se$ Q-value.

TABLE 6.1: The summary on average crystal contamination of three $Zn^{82}Se$ array.

| Isotope | Array contamination, $\mu$Bq/kg |
|---|---|
| $^{232}Th$ | 7±2 |
| $^{228}Th$ | 26±2 |
| $^{224}Ra$ | 27±3 |
| $^{212}Bi$ | 29±3 |
| $^{238}U$ | 10±2 |
| $^{234}U$+$^{226}Ra$ | 33±4 |
| $^{230}Th$ | 18±3 |
| $^{218}Po$ | 21±2 |
| $^{210}Pb$ | 150±8 |

equal to the Q-value of the decay; in case of surface contamination, only a part of the energy is absorbed by the crystal if $\alpha$ particle evacuates from the bolometer. Values of crystal contaminations were extracted (see Tab. 6.1). In Fig. 6.5 the energy spectrum of the $\alpha$ region is shown. The shape and positions of peaks are indicating that contaminations are mostly diffused in the crystal bulk, but it is also possible that part of impurities is implanted deep in the crystal surface. The only isotope with clear indication of surface location is $^{210}Po$: as it has rather short half-life (138 days), it was likely produced by $^{210}Pb$. As one can see in Fig. 6.5, there are two structures at ≈5.3 MeV ($\alpha$) and ≈5.4 MeV ($\alpha$+nuclear recoils). According to Monte-Carlo simulations, the presence of the first peak can be only explained by the contamination of crystal surface or the materials, close to the detector. It was decided to treat the crystals with the same polishing procedure developed by the CUORE experiment [115] for the CUPID-0 crystals to obtain a surface

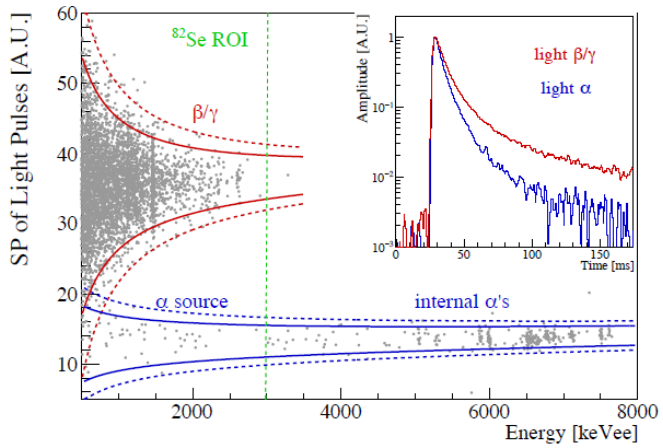


FIGURE 6.4: Shape parameter of a light detector as a function of the energy released in $Zn^{82}Se$-1 (530 h). The red and blue lines indicate the $2\sigma$ (continuous) and $3\sigma$ (dotted) $\gamma/\beta$ and $\alpha$ bands respectively. Inset: time development of light pulses produced by $\gamma/\beta$ (blue) and $\alpha$ (red) particles with energy of about 2.6 MeV.

background reduction.

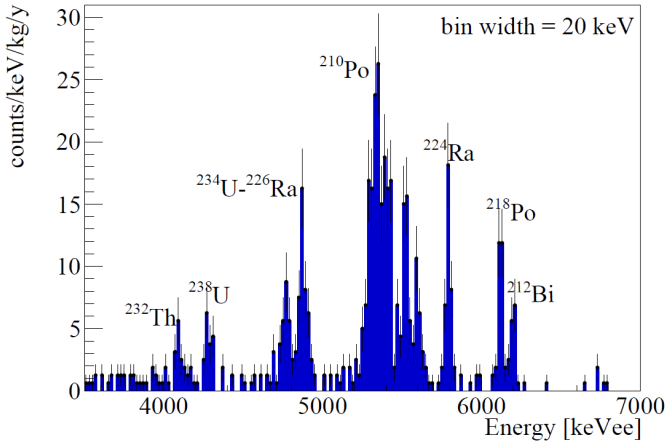


FIGURE 6.5: $\alpha$ spectrum of the $Zn^{82}Se$ array collected in 530 h.

The tested $Zn^{82}Se$ detectors have demonstrated the reproducibility, uniform performance for the enriched crystals and excellent particle discrimination capability. The obtained results are meeting the CUPID-0 demonstrator requirements and allow to proceed to the next phase of the experiment.

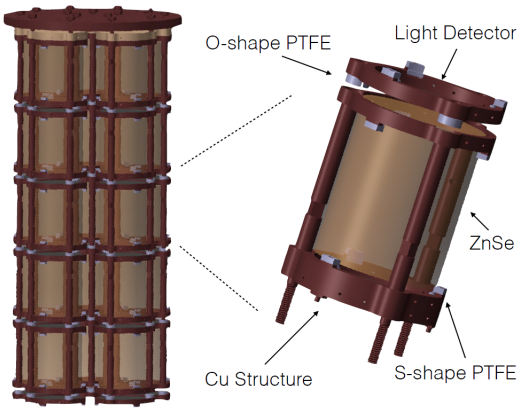


FIGURE 6.6: Rendering of CUPID-0 detector and its single module.

## 6.2 The CUPID-0 demonstrator

One of the primary goal for CUPID-0 demonstrator is to achieve the "zero-background" condition with a background index of $10^{-3}$ counts/keV/kg/yr, which is one order of magnitude lower than the one, obtained in the CUORE experiment. The CUPID-0 demonstrator consists of five towers with 24 enriched crystals (95% of $^{82}$Se) and 2 natural of ZnSe. In the towers each crystal is facing two light detectors. The range of crystals masses is 150–500 g. As the height of ZnSe crystals varies (due to difficulties during the crystal growth), the crystals are arranged in six towers so that each tower is about 30 cm tall (5 towers contain 5 crystals and one contains 6 crystals). The detector design is shown in Fig. 6.6. This structure allows to use a minimal amount of materials, including only ultrapure NOSV copper, PTFE spacers and reflecting foil (VIKUITI-3M).

The total amount of copper used in the detector structure is only 22% of the total detectors mass, one of the lowest ratios in bolometric experiments. All the detector materials were selected after radiopurity screening and for each item a cleaning procedure was established.

### Light detectors

The 40 Ge light detectors were prepared at CSNSM. The germanium wafers were purchased at UMICORE Electro-Optic Material (Geel, Belgium). Each light detector is a double side polished wafer of diameter 44.5 mm and an average thickness of 170 $\mu$m, with an impurity concentration $< 2\times10^{10}$ atoms/cm$^3$. The wafer surface was treated with a mixture of nitric ($HNO_3$ 70%), acetic ($CH_3COOH$ 100%) and hydrofluoride (HF 40%) acids in proportion 5:3:3. The average thickness of the etched layer was $\approx$10 $\mu$m for each wafer. After the chemical etching

the surface was also treated with an Ar ion bombardment. These procedures remove any possible residual oxides and improve the surface quality for the coating process. The SiO coating was deposited on one side of the germanium disk to improve the light collection. It serves as the anti-reflective layer. The average thickness of such layer was 70-80 nm.

### Sensors and gluing procedure

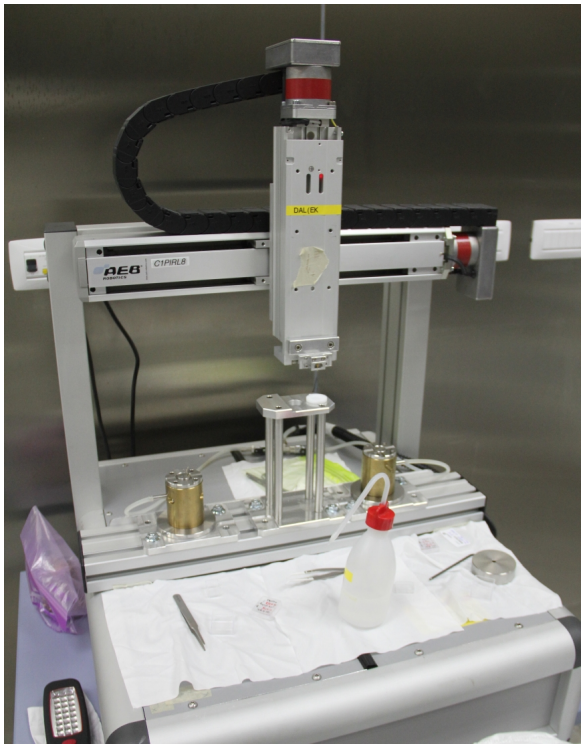

FIGURE 6.7: The semi-automatic system for sensors coupling with high precision of positioning. The two cylinders are used for NTDs fixation and crystals positioning.

The assembly and gluing were performed in a radon-free clean room, belonging to the DarkSide experiment [116]. The clean room environment provides low radioactive conditions and a very stable and safe environment in terms of humidity and temperature. The Rn contamination inside the clean room is below 5 mBq/m$^3$. Such conditions are essential for the preparation of sensitive experiment.

The CUPID-0 sensors (NTD thermistors) were produced out of high purity Ge wafers by irradiation at the MIT Nuclear Reactor Laboratory, Boston (MA, USA). The typical NTD parameters of this batch are $T_0$=4.2 K and $R_0$=1.5 Ohm. NTDs with the size of 2.8×3.0×1.0 mm were used for ZnSe crystals and 2.8×2.0×0.5 mm for light detectors. Before the gluing, NTDs are equipped with gold wires of 25 $\mu$m diameter with the help of a dedicated ball-bonding machine.

Both mechanical and thermal coupling of sensors to the absorbers are delicate since they can significantly affect the bolometer performance. Several investigations [71] have established the optimal geometry of the glue interface between sensor and crystal, and operational conditions. The glue, used for NTD coupling, is the radiopure Araldite used also in CUORE and CUPID-Mo. The glue should be deposited with a 3×3 matrix of dots with 0.7 mm diameter each for the ZnSe crystals, and with 3×2 matrix for the light detectors. The distance between crystal surface and the sensor one is established to be 50 $\mu$m.

For a better reproducibility of the sensor coupling, a semi-automatic system was used during the gluing of CUPID-0 detectors. The robot which was manipulating the matrix with spring-loaded tips is shown in Fig. 6.7. The glue spots deposited on the NTD are shown in Fig. 6.8.

The introduction of the Cartesian robot (moving in x-z plane) reduces possible inhomogeneities, which can be caused by manual work and gives the advantage of precise timing, which is essential considering the short time window of Araldite glue life-time.

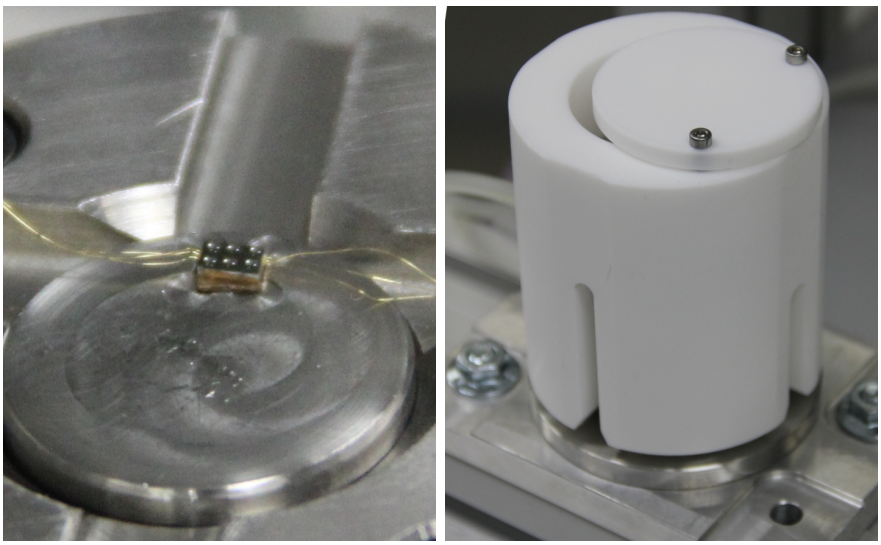

FIGURE 6.8: Left: the glue spots, deposited on the NTD sensor before coupling to the light detector. Right: the PTFE holder with the Ge wafer inside, installed on the base with NTD sensor.

The gluing procedure is divided into three phases:

- Firstly, the spring-loaded tip matrix is connected to the Cartesian robot manipulator according to the kind of NTD to be glued (nine tips or six tips matrix). Then the NTD sensor is positioned on the metallic device on the robot working space. The NTD is kept in place by vacuum. The gap of 50 $\mu$m is created before the glue deposition by a dedicated tool. The ZnSe crystal or the light detector has to be prepared in advance in a special PTFE holder

FIGURE 6.9: The light detector with the coupled NTD sensor. Between the two surfaces one can see the array of separated glue spots.

that will be inserted on the device with the NTD on it after the glue deposition phase (see Fig. 6.8).

- The glue deposition is started with the mixing of the two epoxy components of Araldite glue. This procedure is performed using a dispensing gun with a disposable static mixer. A dedicated PTFE container is filled with the mixed glue and placed on the Cartesian robot. The depth of the PTFE container (0.7 mm) allows to control the glue amount on the tips. The robot arm dips the spring-loaded tip matrix in the glue container and then moves it to the sensor to deploy the glue dots on the surface.

- The last phase is the crystal fixation. The crystal or the light detector is fixed in the PTFE holder and then it is lowered on the NTD. The gap of 50 $\mu$m between the crystal and NTD surfaces is provided by the dedicated mechanical fixation. The NTD is kept by vacuum during gluing and drying process. 1.5 hour is needed for drying. After this time the crystal can be moved. All listed precautions are preventing the glue from merging and keeping the glue spots. The result of light detector gluing is shown in Fig. 6.9.

  All the bolometers are also equipped with a silicon resistances for the injection of a known amount of energy and allowing the stabilization of detector response [98]. The Si resistors are glued by hand, with one glue spot and no spacers, as the glue conductance is not important for the heat injection.

### Assembly and installation

A custom set of tools was prepared for the assembly of CUPID-0 detectors. The tools were produced by an ENVI-SIONTEC ULTRA 3SP 3D printer using a highly radiopure plastic resin. These tools are including a mounting plate and a handling system.

The detector supports consists of copper structure and PTFE spacers. The copper structure includes: 70 frames, 78 columns and one

large plate for the tower coupling to the cryostat. All the copper pieces were made from electrolytic tough pitch copper (NOSV). The copper components were cleaned before the assembly by Legnaro National Laboratories (LNL). The cleaning protocol includes 61 sub-process with following main steps: tumbling, electropolishing, chemical etching and magnetron plasma etching.

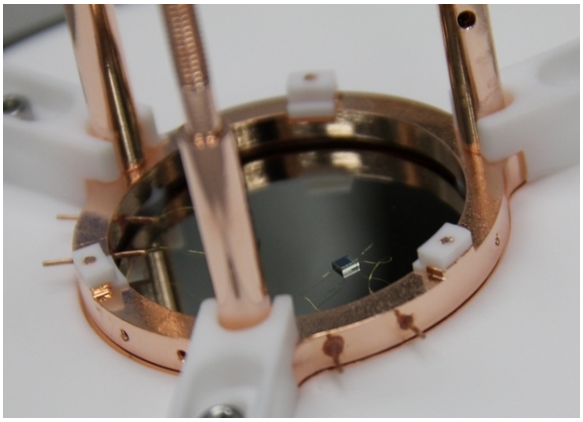

FIGURE 6.10: The light detector during the tower assembly: the frame is fixed with PTFE pieces for the stability of future tower.

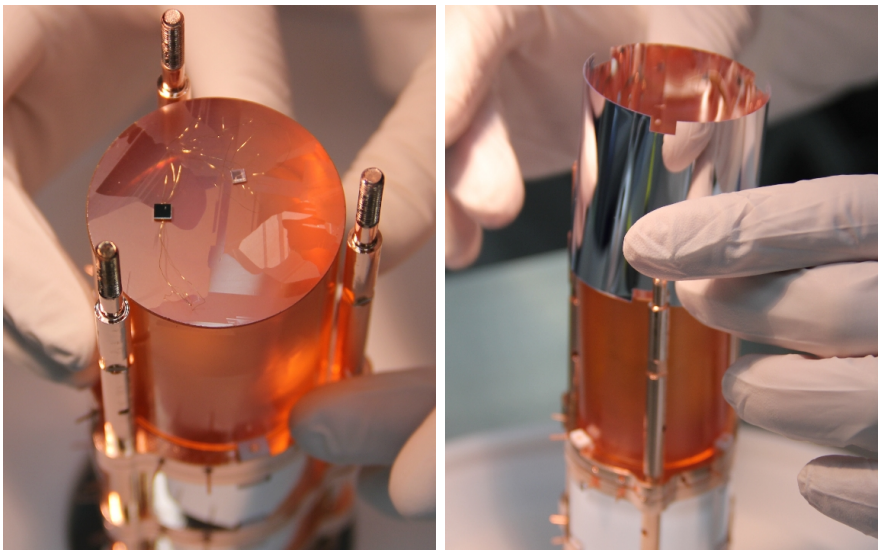

FIGURE 6.11: Left: The $Zn^{82}Se$ crystal with NTD sensor and silicon heater on the top during the tower assembly: crystal is being installed on the frame. Right: positioning of the reflecting foil around the crystal.

All 31 LD were mounted individually in the copper frames (see Fig. 6.10). For each bolometer the gold bonded wires of NTD sensors and heaters were crimped inside copper pins, fixed on each frame. Each

tower assembly was started with fixation of the copper frame with the LD. Then, PTFE pieces were fixed on the frame for crystal handling, and copper columns for the next module installation. Then the crystal is slided on its position (see Fig. 6.11). Next step is the positioning of the reflecting foil. This foil was cut and glued with Araldite glue to the right size in advance. A copper frame is installed next for electrical contacts of the crystal, and on the top the frame with LD is positioned. Each tower contains 5 of such floors. In between the operations with

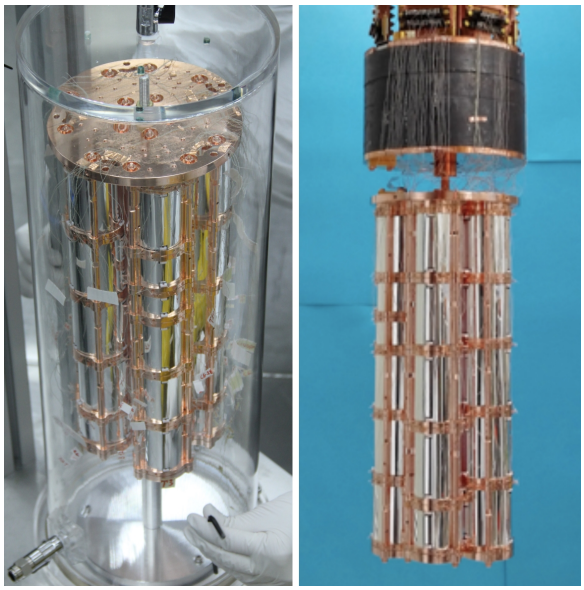

FIGURE 6.12: The five towers, stored under nitrogen flow (left), and the demonstrator, installed in the cryostat before closing (right),just below the 10 cm thick Roman Pb shielding.

the crystals, and after the full assembly the detectors were hosted in a nitrogen-flushed container. After the assembly of five separate towers was finished, the wire connection was performed: the twisted pairs of thin silk-covered wires were crimped in the outside part of the copper pins for each channel. Finally, the five towers were connected to a copper plate (see Fig. 6.12), and attached to the cryogenic system in the Hall-A in LNGS (see Appendix A for the details on the cryostat).

### First results

The data-taking has started in June 2017 after two months of detector commissioning and debugging. While measurements are still ongoing, datasets, collected between June and December 2017 were analyzed. 83 % of the time were dedicated to background measurements, 10% for $\gamma$ energy calibration, 1.6% for neutron calibrations and 5.4% were spent on helium refills and various tests. The background measurements were divided into four datasets. Each dataset started and ended

with Th calibration. The trigger threshold depends on the channel and varies between 10 and 110 keV. The heaters produce signals every 400 seconds, and heater pulses are automatically marked by the acquisition software. Using the $^{232}$Th data sets, the calibration and energy reso-

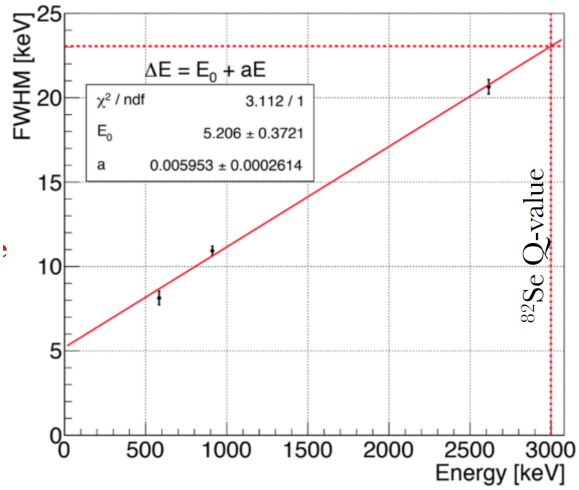


FIGURE 6.13: The FWHM versus energy, averaged for all detectors and extrapolated for the $Q_{\beta\beta}$.

lution evaluation was performed. The fit and extrapolation of FWHM at the $Q_{\beta\beta}$ are presented in Fig. 6.13. The resolution at the $Q_{\beta\beta}$ was calculated separately for each dataset and exposure weighed for the combined result: FWHM $Q_{\beta\beta}$=23.0±0.6 keV (0.77%). The intrinsic limitation on FWHM, caused by the noise fluctuations, is 5 keV on average.

The collected background spectrum has passed the careful selection of appropriate signals. The non-physical events (i. e. not particle) are rejected by pulse shape analysis on the heat channels (Zn$^{82}$Se). At this initial phase the counting rate in analysis window (2800-3200 keV) is $\approx 10^{-2}$ counts/keV/kg/yr and is dominated by $\alpha$ background and $\gamma$s from $^{208}$Tl decays. The $\alpha$ background is rejected using pulse shape analysis of the light signals (see Fig. 6.14).

Using the delayed veto approach, the events from Bi-Po decays are also rejected: for each $^{212}$Bi candidate (energy range 2-6.5 MeV to include surface contamination, $\alpha$ events by the pulse-shape) the crystal, where decay has occurred, was disabled for 9.15 minutes (3 half-lives of $^{208}$Tl). More details on data analysis can be found in [117]. The different phases of background rejection are shown in Fig. 6.15. The obtained background index is $3.6^{+1.9}_{-1.4}\times10^{-3}$ counts/keV/kg/yr. This is an unprecedented background level, observed in a bolometric experiment. This result is obtained thanks to the excellent $\alpha$-rejection achieved by the scintillating calorimeter technique [64].

The obtained limit on $0\nu2\beta$ half-life of $^{82}$Se is $T^{0\nu}_{1/2} = 2.4 \times 10^{24}$ yr with an exposure of $^{82}$Se of 1.83 kg×yr, which corresponds to $\langle m_{\beta\beta}\rangle <$

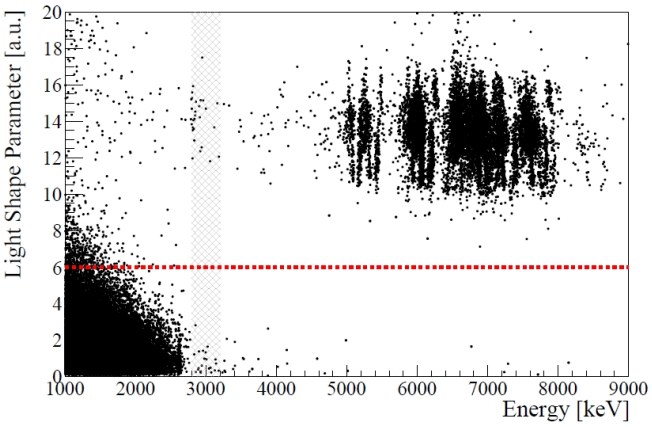


FIGURE 6.14: Single-hit events in the Light Shape Parameter-Energy plane. The $\alpha$ events are concentrated in the right upper region; $\gamma/\beta$ events populate the left lower corner. The red dotted line indicates the acceptance threshold. The shaded vertical band represents the analysis window used for the background evaluation at $Q_{\beta\beta}$.

$376-770$ meV. It is the strongest current limit on $^{82}$Se, and it is almost one order of magnitude better than the previous limit $T^{0\nu}_{1/2} = 3.6\times10^{23}$, obtained by NEMO-3 experiment with exposure of 3.5 kg×yr [62].

## 6.3 Conclusions and perspectives

The bolometric approach for $0\nu2\beta$ decay searches is demonstrating very promising results with different isotopes. The scintillating bolometers technology was successfully applied for searches with $^{82}$Se. The obtained level of background is demonstrating the possible improvement of sensitivity for the ton-scale bolometric experiment. A detailed investigation of the background components will be performed in close future.

The data-taking is ongoing with the aim to reach 10 kg×yr for ZnSe. With this exposure the already obtained sensitivity will be improved. As the cryostat is able to host up to 136 channels (while 57 are used), a second phase of the CUPID R&D program is under discussion. With the outstanding background level, second phase with another isotope of interest can provide promising results.

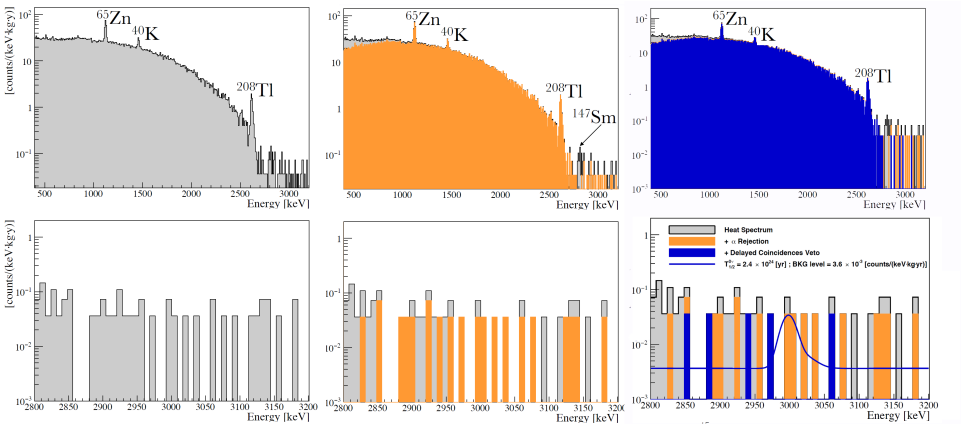


FIGURE 6.15: The total energy spectrum (top) and spectrum in the analysis window (bottom). The grey histogram is the spectrum obtained with the selection on Zn$^{82}$Se thermal pulses (left). The filled orange histogram includes the $\alpha$ rejection through the LD pulse shape (center). The filled blue histogram is the final spectrum after the delayed-coincidences veto is applied (right). The blue line is the fitted spectrum together with a hypothetical signal corresponding to the 90% C.I. limit of $T^{0\nu}_{1/2} = 2.4 \times 10^{24}$ yr.

# Chapter 7

# R&D tests with bolometers

During my PhD thesis, I have contributed to some R&D activities related to the bolometric searches for neutrino physics. They included characterization of temperature sensors and tests of new crystal compounds as bolometers. Such activities are important for the development of a viable big-scale experiment, as they give possibilities to develop the technology, study better sensor properties or provide new bolometric detectors for various applications.

In the following section two particular R&D tests are described, performed in CSNSM laboratory (Orsay, France).

## 7.1 LUMINEU NTD characterization

In the framework of the LUMINEU project, a new activity related to NTD (Neutron Transmutation Doped termistors, described in Chapter 3) sensor production was started. This kind of sensor is commonly used in bolometric experiments, such as CUORE, EDELWEISS and CUPID-0. The main advantages of Ge NTD are their reproducibility (crucial point for large-scale experiments), possibility to operate the detectors over a large range of temperatures and ease of manipulations during the detector assembly (for NTD operation principle see Chapter 3). In the past several batches of NTDs have been produced at the Lawrence Berkley National Laboratory (LBNL) [118]. They have fulfilled the requirements of both past and present experiments with a big amount of channels (for example Cuoricino and now CUORE with 988 heat channels, read by one NTD sensor each channel). An alternative production of NTDs for LUMINEU and CUPID-Mo in view of CUPID was strongly motivated given the high number of samples.

In this context a production line has started in CEA. Ten high-purity Ge wafers (⌀7.6×0.05 cm) were irradiated by a neutron flux from the reactor Orphee at Saclay. The total neutron flux was measured with the AlCo wires, used as dosimeters. The irradiation was performed in several steps, to avoid overdoping the wafer over the desired value. The total neutron flux for the wafers was in range $3.44\text{-}3.56\times10^{18}\text{n}\times\text{cm}^2$ [119]. After the wafer irradiation, the process of sensor production implying cutting and gold electrodes deposition was performed, but not completely successfully [120]. A small number of individual sensors was produced out of different wafers for performance tests.

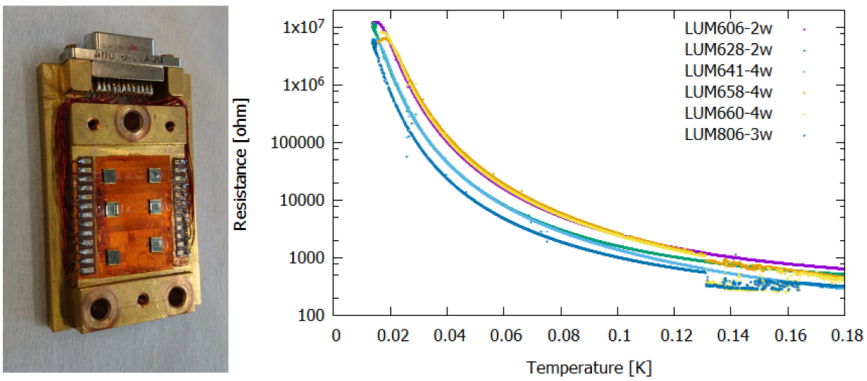


FIGURE 7.1: The holder for sensors test with 6 NTDs, attached using vacuum grease (left), and the R(T) characterization (right).

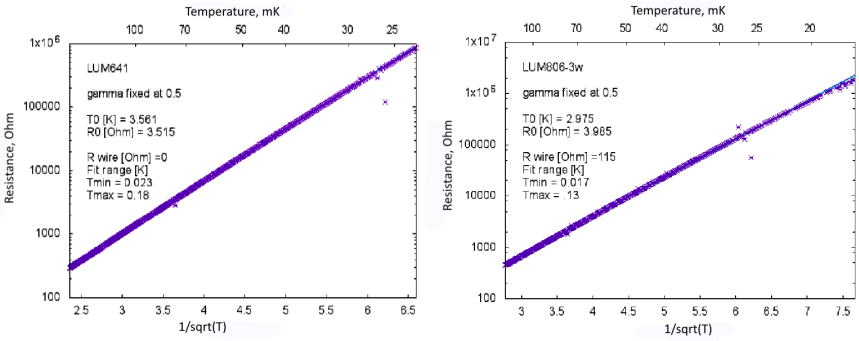


FIGURE 7.2: The linearazed R-T dependence with fit $R = R_0(\frac{T_0}{T})^{1/2}$.Left plot is LUM641, right is LUM806.

During my thesis I have contributed to the characterisation of some samples. 6 NTD sensors have been characterized in the pulse-tube cryostat (Ulysse) in terms of R(T) curves using the TRMC2 system [121]. This system allows measuring the resistance and temperature simultaneously, with a possibility to set constant current/voltage to read the sensors. Also the speed of cooling/heating up can be established. The assembly and resulting plots are shown in Fig. 7.1. For each NTD the data was linearized and fitted with the Efros and Shklovskii law [85] (see Fig. 7.2). The summary of the NTD main characteristics is shown in Tab. 7.1.

Usually the macrobolometers operated at LSM have an NTD resistance around 1 MOhm at 20 mK. As one can see from the table, three samples had too high resistance, while the other three had the parameters, suitable for bolometric measurements.

Considering the results of this characterization, two NTDs were selected to perform sensitivity studies and to compare with the previously used sensors: LUM641 and LUM806. LUM641 fit well the requirements of acquisition systems with DC electronics (CUPID-0, Ulysse), while

TABLE 7.1: Summary on NTD characterization. Number in the NTD ID corresponds to the number of wafer.

| NTD | Total neutron flux, $10^{18}\times n\times cm^{-2}$ | $T_0$, K | $R_0$, Ohm | R at 20 mK, MOhm | R at 15 mK, MOhm |
|---|---|---|---|---|---|
| LUM658 | 3.44 | 4.430 | 3.480 | 10 | 101 |
| LUM660 | 3.53 | 4.309 | 3.522 | 8.3 | 81 |
| LUM606 | 3.48 | 4.233 | 3.446 | 7.1 | 69 |
| LUM628 | 3.54 | 3.616 | 3.470 | 2.3 | 18 |
| LUM641 | 3.55 | 3.561 | 3.515 | 2.2 | 17 |
| LUM806 | 3.56 | 2.975 | 3.985 | 0.79 | 5.2 |

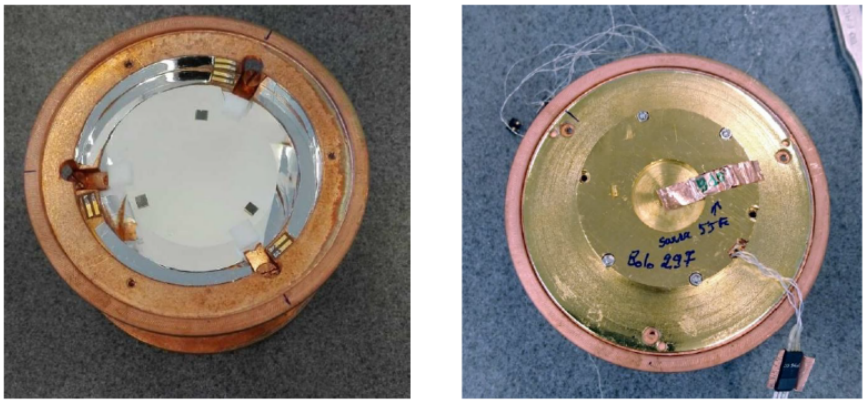

FIGURE 7.3: The $Li_2MoO_4$ crystal with three NTDs on its top surface, fixed with PTFE spacers in a copper holder (left) and closed detector with a light detector on the top (right).

LUM806 is an appropriate sensor for AC acquisition (EDELWEISS set-up) due to low resistance.

### 7.1.1 Bolometric test

For the bolometric test a natural $Li_2MoO_4$ crystal (⌀ 4×4 cm) already measured in the same conditions (aboveground, Ulysse cryostat) was chosen [122]. Three NTD sensors were coupled to the crystal surface with Araldite glue (see Fig. 7.3). As a reference we used an NTD from LBNL batch ("Beeman" NTD, $T_0$=3.8 K, $R_0$=1.1). The NTDs were glued with six spots of Araldite and 50 $\mu$m gap between the two surfaces. The crystal was coupled to a Ge light detector for alpha discrimination. The assembly is shown in Fig. 7.3.

As a first step, the R(T) characterization of the NTDs was performed to compare with reference "Beeman" NTD and to check the

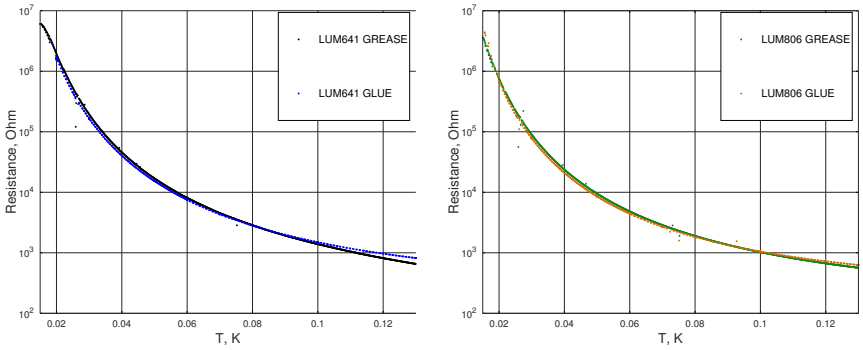


FIGURE 7.4: Comparison of R(T) characteristics with two different couplings of NTDs to the absorber.

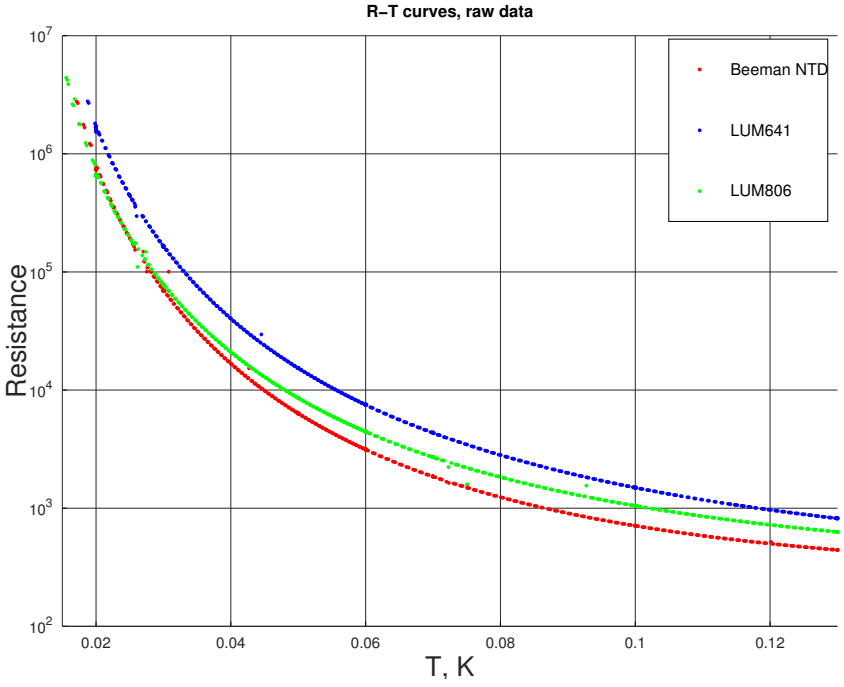


FIGURE 7.5: The R(T) characterization of three NTDs during the measurements with $Li_2MoO_4$ crystal.

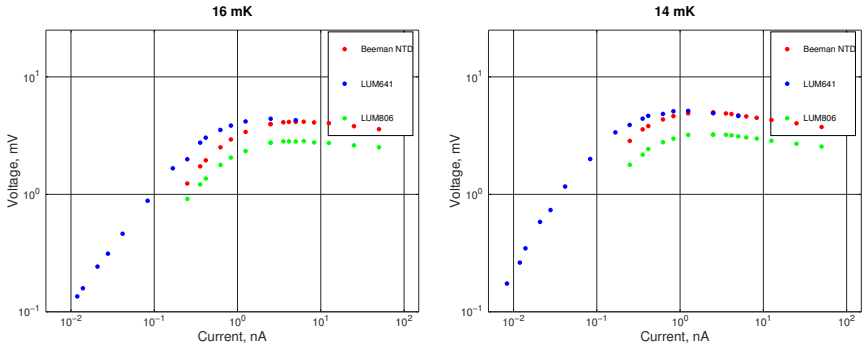


FIGURE 7.6: IV characteristic of the NTDs.

TABLE 7.2: Time characteristics of the average pulses from three NTD sensors.

| NTD | Size, mm | Mass, mg | Rise time, ms | Decay time, ms |
|---|---|---|---|---|
| "Beeman" | 3×3×1 | 50 | 22 | 87 |
| LUM641 | 3.5×3×0.5 | 30 | 20 | 94 |
| LUM806 | 3.5×3×0.5 | 30 | 26 | 124 |

dependence on thermal coupling[1]. The resulting plots are shown in Fig. 7.4 and Fig. 7.5. As the NTD reading with TRMC2 saturates at temperatures lower than 20 mK due to the high resistance, an additional interest was to check the behavior of NTDs at lower temperatures. That is why the operating temperature of the cryostat was fixed at two points: 14 mK and 16 mK. The static behavior of the sensors was obtained at these two temperatures (see Fig. 7.6). Changing the bias on the NTD, the voltage changes on it in the absence of signals. At high bias, the V-I relation deviates from the ohmic behavior due to electrothermal feedback, as the Joule heating dominates and actually decouples the electronic system: the curve bends at a so-called inversion point. All three NTDs have similar behavior, with the optimal working point at 0.832 nA.

The data was recorded in stream mode, with 10 kHz sampling frequency. Characteristic times of the signals read by the NTDs were compared (see Tab. 7.2 and Fig. 7.7). The rise and decay time for each sensor differ for several ms and show the typical length for this kind of absorber.

Unfortunately, we could not achieve the same noise conditions as we had in the previous measurement with the same crystal. Thanks to the direct comparison of NTD sensitivities and resolutions (see Tab. 7.3), we can conclude that LUM641 is demonstrating very similar performance to our reference NTD, while LUM806 has two times lower sensitivity.

[1]We remind the reader that for characterization test, NTDs were coupled through vacuum grease

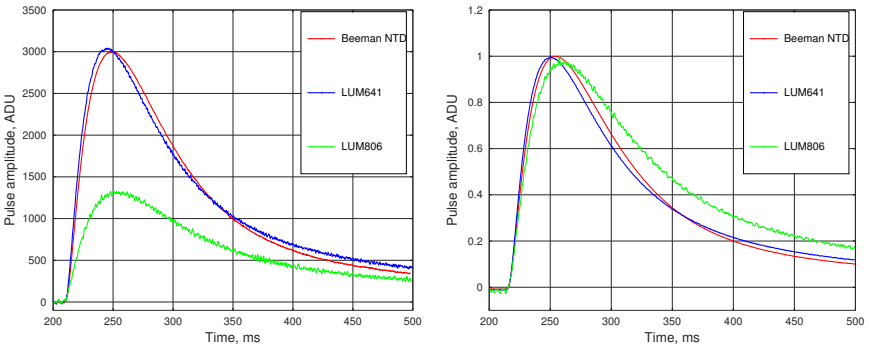


FIGURE 7.7: The signals, obtained with three NTDs from the same event (left), and normalized average pulse for three NTDs on the right.

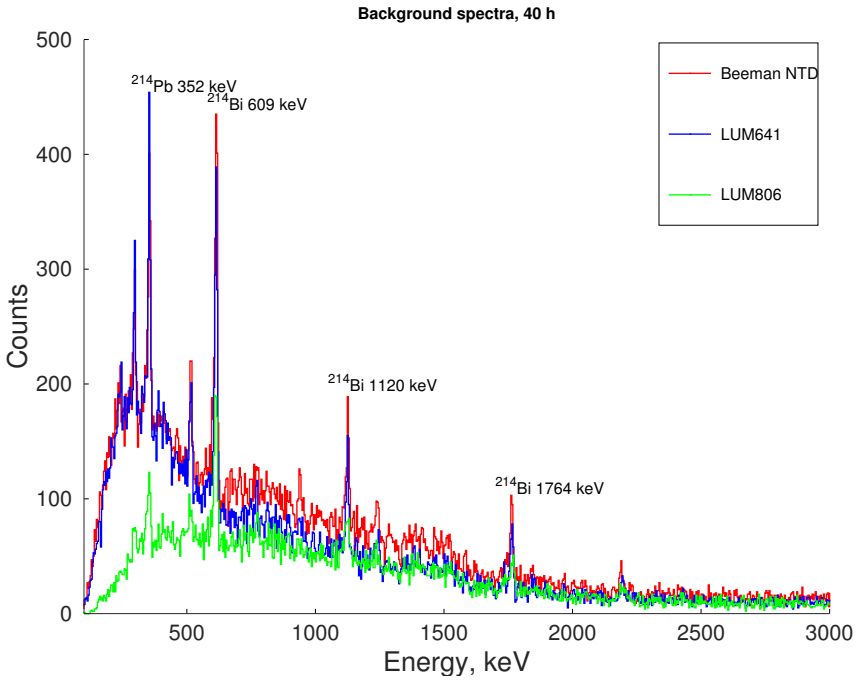


FIGURE 7.8: Background spectra obtained for three NTDs in a simultaneous measurement. As the sensitivity of LUM806 is two times lower, it is affected more by noise conditions at low energies, and significant part of events is rejected by the cut on pulse-shape correlation.

In future the reproducibility concerning resistance and performance of NTDs from the same wafer will be tested. In case of a positive outcome, the new NTDs can be used for future measurements in the CUPID-Mo framework. The wafers with good doping level will be cut and the gold contacts deposition will be performed. The wafers with insufficient doses can be re-irradiated to increase the doping level and

TABLE 7.3: Summary of NTD performance during the bolometric measurement.

| NTD | Sensitivity, nV/keV | Baseline FWHM, keV | $^{214}$Bi, 609.3 FWHM, keV | $^{214}$Bi, 1764.5 FWHM, keV |
|---|---|---|---|---|
| "Beeman" | 68.8 | 6.4(1) | 10.6(7) | 12.2(1) |
| LUM641 | 68.8 | 6.0(1) | 10.1(7) | 10(1) |
| LUM806 | 30.2 | 12.4(2) | 12(2) | 13(3) |

to reduce the resistance.

### 7.1.2 Summary

NTD Ge thermistors are well-studied sensors [82] , they are easy to operate and they fit well the requirements for $0\nu2\beta$ decay bolometric experiments in terms of radiopurity and performance.

Mass production of NTD sensors is required for building a large-scale bolometric experiment with big arrays of detectors. The first tests on NTDs, produced in the LUMINEU framework, are giving promising results: the performance of tested samples is similar to the performance of "reference" NTDs, which are used in searches for $0\nu2\beta$ decay [118]. Even if confirmation of samples uniformity is required, already tested sensors can be used in bolometric detectors for future measurements.

## 7.2 The BASKET project: $Li_2WO_4$ bolometers

As it was mentioned before (see Chapter 1), the cross-sections of neutrino interactions are extremely small. Experiments studying neutrino properties require high accuracy measurements. Recently the coherent elastic neutrino-nucleus scattering (CENNS) was observed for the first time by the COHERENT collaboration [23]. This reaction was predicted after the weak neutral currents discovery [123]. CENNS investigation will allow to perform tests on Standard Model with high precision. Measurements of the Weak angle, $\sin^2\theta_W$ and of the nuclear structure can be performed with the study of CENNS. This process can also be used for nuclear reactors monitoring. Precise studies of CENNS are required for background understanding for Dark matter experiments. Regarding the neutrino flux from reactors, new interactions can be studied within theories of CENNS:

- Anomalously large neutrino magnetic moments: if neutrinos have Dirac nature, they should have very small magnetic moment,

but in the framework of New Physics theories it can become detectable, providing a contribution to the nuclear recoil spectrum at low energies.

- Non-Standard Interactions (NSI) of neutrinos can affect the total CENNS rate, predicted by the Standard Model.
- Couplings to new massive scalar and vector mediators can affect the CENNS recoil spectrum.
- Active-to-sterile neutrino oscillations can be studied with the CENNS measurements, but a high precision of measurements is required and specific distance to the reactor.

There are several cryogenic experiments (planned or ongoing), that are aiming at exploring the low-energy region of the CENNS spectrum [124].

BASKET (Bolometers At Sub KeV Energy Thresholds) is an R&D project developed at CEA (Commissariat Energie Atomique) aiming at the investigation of CENNS with $Li_2WO_4$ bolometers. In addition to the high energy resolution, common for all bolometric detectors, $Li_2WO_4$ crystals can provide efficient neutron tagging thanks to their natural content of $^6$Li (7.59%). Particle discrimination for background rejection can be performed both using light detectors (scintillation light for $\alpha/\gamma(\beta)$ discrimination), or by pulse-shape analysis of the signals. During this new R&D, several types of sensors will be tested: MMC [84], NTD, TES [83] to obtain the best sensitivity in the low energy region and low threshold. I will report the results from the first test on a $Li_2WO_4$ crystal with NTD sensor, coupled to a Neganov-Luke light detector.

### 7.2.1 Description of the assembly

The characterization of the first BASKET detector was performed at the CSNSM laboratory (Orsay, France). $Li_2Mo_{0.05}W_{0.95}O_4$ crystal was grown by Czochralski method with Mo doping. Luminescence measurements at 300 K and 10 K [125] were performed. The crystal used for the test has an elliptic shape with a mass of 11 g (see Fig.7.9). As temperature sensor, a neutron transmutation doped (NTD) germanium thermistor was used. A silicon heater was glued with the purpose of baseline stabilization. The sensors were coupled to the crystal using Araldite glue. The bonding, providing thermal and electrical link was performed with two gold wires for the NTD and two aluminum wires for the heater. The scintillating bolometer was also coupled to a Neganov-Luke germanium photodetector. Such detector consists of a thin germanium slab (44 mm diameter) with aluminum concentric circles (grids) deposited on the surface, giving the opportunity to amplify the light signal [89]. A smeared $^{210}$Po alpha source was placed close to the crystal on the copper holder at $\approx$ 1 cm distance from the lateral

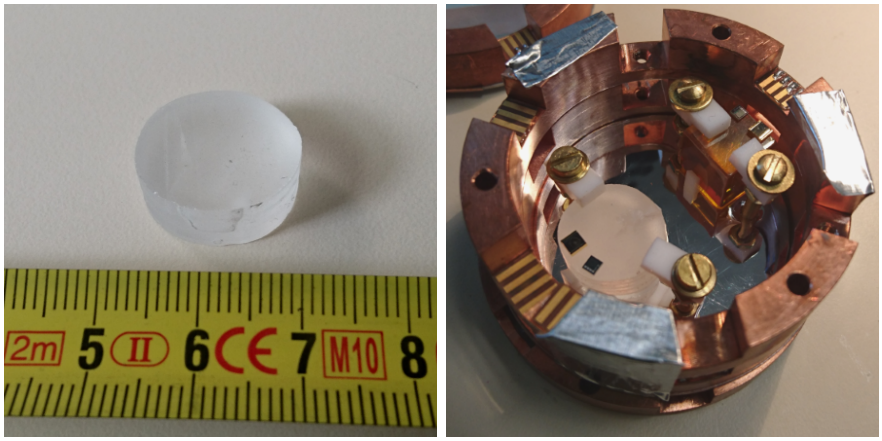

FIGURE 7.9: The $Li_2WO_4$ crystal sample ⌀12.5×5mm, used for the bolometric test before assembly (left) and the $Li_2WO_4$ with NTD and heater glued on top, fixed in the copper holder with Teflon spacers along with another crystal (right).

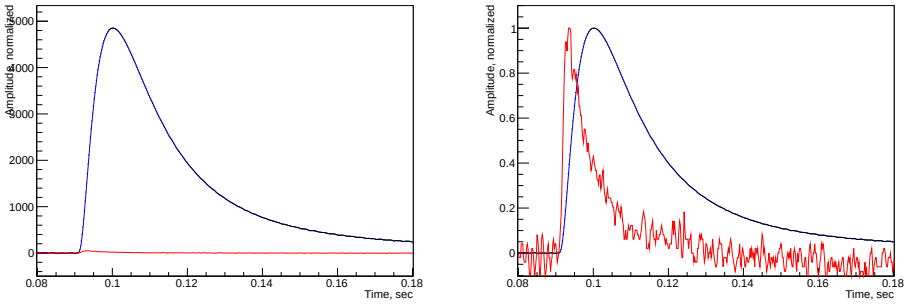


FIGURE 7.10: Example of two types of signal in coincidence: heat signal in blue and light is in red. On the left pulse amplitude is in ADU, on the right is normalized.

crystal surface. The measurement was performed in the dry pulse-tube cryostat "Ulysse", located aboveground in the CSNSM laboratory (see Appendix A). The shielding is provided by a low-activity lead shield with 10 cm maximum thickness. The data was acquired in the stream mode, with 5 kHz sampling rate and ±5 V dynamic range.

### 7.2.2 Pulse characteristics

The typical pulse duration is ≈ 50 msec. In Fig. 7.10 the typical heat-light signal in coincidence is shown, in scale and normalized. In Tab. 7.4 the characteristic times of the pulses at the different temperatures are shown. As NTDs are slow sensors, these properties are important for pile-ups rejection and pulse-shape discrimination. The typical signal duration from bolometric crystals of similar mass is in the range of 0.3-0.1 seconds with NTD sensors. The $Li_2WO_4$ crystal

bolometer demonstrates a relatively fast response, which depends on the heat capacity. Fast signals allow to obtain a smaller amount of the pile-ups, but require high sampling rate to improve conditions for the pulse-shape analysis.

TABLE 7.4: Characteristic times of $Li_2WO_4$ signals at different temperatures.

| | 15 mK | 17 mK | 20 mK |
|---|---|---|---|
| Rise time, ms | 5.8 | 4.0 | 3.4 |
| Decay time, ms | 18.8 | 17.8 | 19 |
| Mean time, ms | 41 | 42.6 | 47 |

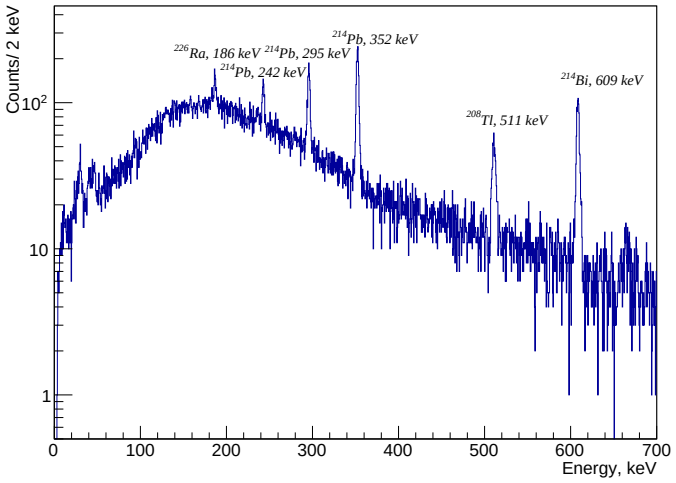


FIGURE 7.11: Background energy spectrum accumulated over 100 h with 11 g $Li_2WO_4$ scintillating bolometer at 20 mK.

### 7.2.3 Energy resolution

The background measurement was collected during ≈100 hours at 20 mK. The background energy spectrum is shown in Fig. 7.11. The energy resolution of several gamma peaks coming from environmental radioactive isotopes of $^{214}$Pb and $^{214}$Bi is presented in Tab. 7.5. Noise conditions were favorable, but there is possibility for improvement. For instance, the resolution of $^{214}$Bi peak at 609 keV is FWHM=3.7 keV, equal to 0.6% which can be improved in low-noise conditions.

### 7.2.4 Particle discrimination

The light collection without gain on Luke detector grids does not allow us to discriminate completely $\alpha$ particles from $\gamma/\beta$ due to the low

TABLE 7.5: The resolutions of several gamma lines of background spectrum

| Gamma line, keV | FWHM, keV |
|---|---|
| 0 | 1.1(1) |
| 186 | 2.5(2) |
| 242 | 2.4(1) |
| 295 | 3.1(1) |
| 352 | 3.2(1) |
| 511 | 4.1(2) |
| 609 | 3.7(1) |

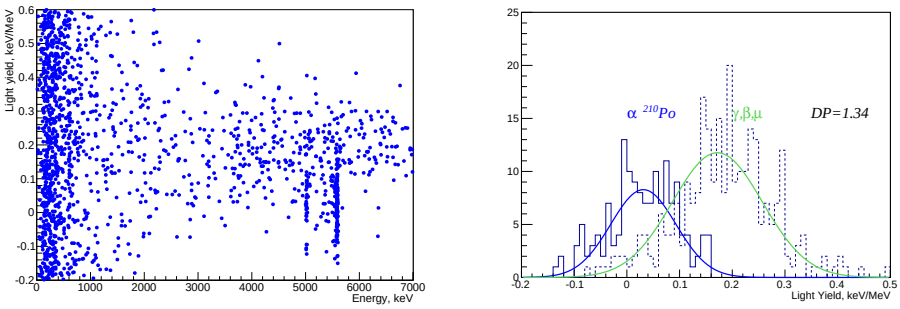


FIGURE 7.12: On the left:the scatter plot with 0 V bias applied on Neganov-Luke light detector. On the right:the LY histogram between two particle types with 0 V bias on the grids, the $\alpha$ light amplitude(solid histogram) is slightly lower, than for $\gamma/\beta$(dashed histogram), discrimination power is $1.34\sigma$.

light yield of this crystal. The scintillation light yield of $Li_2WO_4$ is 0.2 keV/MeV,which is low compatibly to other types of scintillating crystals as $Li_2MoO_4$ $ZnMoO_4$(0.7-1.5 keV/MeV). The DP (discrimination power) is $1.3\sigma$ at 0 V bias on Neganov-Luke light detector grids, but with minimal gain of 25 V the DP becomes $5.4\sigma$ allowing a full alpha background rejection, which is important possibility to tag neutron events (neutron capture on $^6$Li). The DP value can also be increased applying higher gain on the Neganov-Luke light detector. In Fig. 7.12 and Fig. 7.13 the comparison of DP for Luke detector with grids biased at 0 V and at 25 V is shown.

The pulse-shape analysis was performed, using a simple PSD parameter: first, the mean pulse collection and optimal filter transformation were executed. Second, a linear fit of the [X,Y] data was performed, where X are points of the mean pulse and Y are points of the filtered pulse in the given interval. Obtained DP=$3.97\sigma$ by the pulse-shape parameter, which allows to reject more than 99% of $\alpha$ particles from the $\gamma/\beta$ region. Scatter plot and histograms are shown in Fig. 7.14. The discrimination can be improved with lower noise conditions.

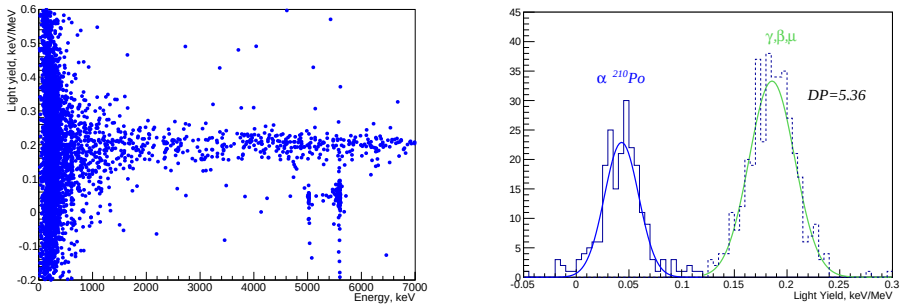


FIGURE 7.13: On the left:the scatter plot with 25 V bias applied on Neganov-Luke light detector. On the right:the discrimination between two particle types with 25 V bias on the grids, the $\alpha$(solid histogram) light amplitude(solid histogram) now can be separated from $\gamma/\beta$(dashed histogram), thanks to an increased sensitivity of the light read-out.

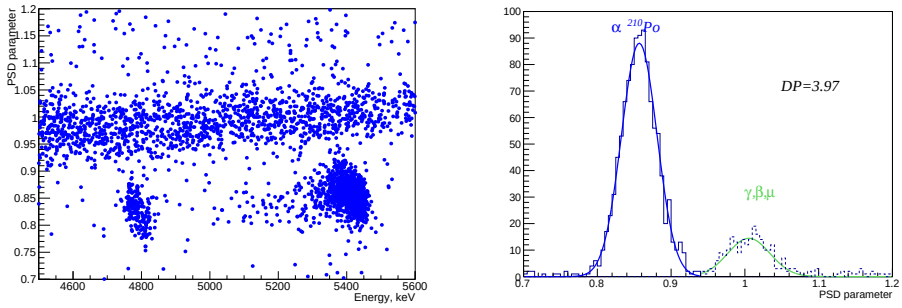


FIGURE 7.14: On the left:scatter plot of pulse-shape parameter. On the right: the pulse-shape parameter discrimination of $\alpha$(solid histogram) particles from $\gamma/\beta$(dashed histogram).

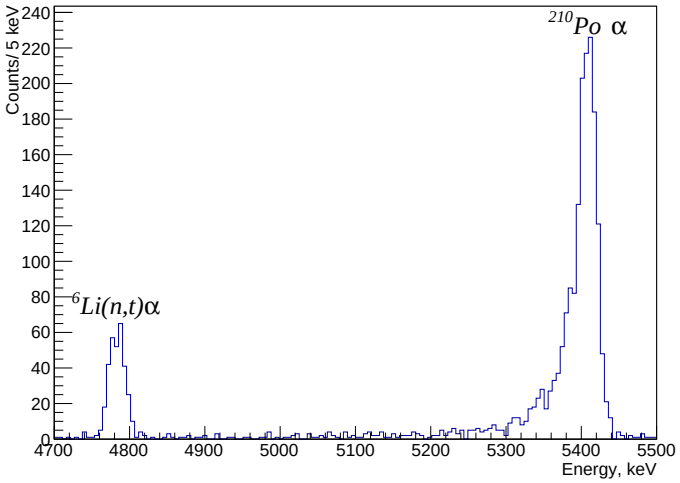


FIGURE 7.15: Alpha spectrum after discrimination.

### 7.2.5 Alpha region

As the $^{210}Po$ source was used, and the crystal was operated for a short time in a not low-background environment, the accurate study of the crystal internal radiopurity could not be performed with sufficient precision. By the way no lines of $^{232}$Th or $^{238}$U were observed in the spectrum.

Due to thermal quenching, which is typical for crystals of this type, in $\gamma$ energy scale the alpha peaks are shifted by 2% with respect to energy of the reaction (4874 keV for $^{6}$Li(n,t)$\alpha$ and 5407 keV for $^{210}$Po $\alpha$ decay). After separation, an energy calibration was performed. The energy resolutions are 24 keV FWHM on neutron peak and 28 keV on $^{210}$Po peak.

### 7.2.6 Energy threshold

The energy threshold was evaluated with the following method: using the heater, a known amount of low amplitude pulses was injected. The voltage on the heater was tuned to cover energy region from 1 to 6 keV. For data analysis and triggering, the optimum filter method was used [93]. With the known amount of injected pulses, the energy threshold was evaluated: efficiency is the ratio of triggered pulses to the total amount (in %). In the Fig.7.16 the resulting plot is shown. The fit is done by the function $p_{trg}(E) = 0.5 \times (1 + erf[(E - E_{th})/(\sqrt{2}\sigma_{th})])$, where erf is the Gaussian error function. The fit is resulting in the energy threshold at $E_{th} = 3.03 \pm 0.04$ keV and the $\sigma_{th} = 0.42 \pm 0.07$ keV, while the average baseline noise resolution is $\sigma_{bsl} = 0.47 \pm 0.04$ keV, which means that the energy resolution is affected by the baseline noise. The $E_{th}$ value corresponds to 6.4 $\sigma_{bsl}$. Operation in low-noise

and low-background conditions can allow to obtain threshold at 4-5 $\sigma_{bsl}$.

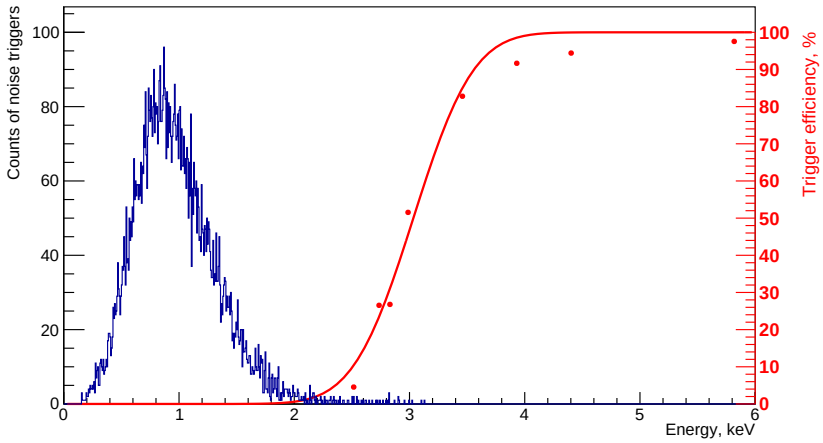


FIGURE 7.16: Determination of the trigger threshold. The data is fitted by an error function, and the energy threshold is 3 keV for 50 % efficiency. The reconstructed energy of pure noise samples after fi ltering is shown in a histogram (blue, left y-axis).

### 7.2.7 Summary

Coherent neutrino scattering is a process of particular interest for neutrino physics since the recent discovery. Precise investigation of this process with different sources of neutrinos is required. In the framework of the BASKET project the first test of a $Li_2WO_4$ crystal was performed. This detector is showing good performance, high energy resolution with an NTD sensor. The approaches for improvement of the threshold are under discussion.

Having the many-years experience of crystal growth and purification of Li-containing crystals [95], the first samples of $Li_2WO_4$ crystals with high purity were produced in NIIC. In the nearest future more tests will follow, in particular, as the scaling of the crystal mass directly affects the threshold, detectors with the smaller crystal sizes (2×2×2 mm and 10×10×10 mm) will be measured. Tests with MMC and NbSi TES sensors to choose the most suitable type will be performed.

# Appendix A

# Cryostats

The searches for $0\nu2\beta$ decay with bolometers require dedicated cooling set-ups, able to operate with large masses of detectors. The use of dilution refrigerators (DR) can provide cooling down of the samples and maintaining stable conditions at T $\approx$ 10-20 mK. Such set-ups are complicated systems, which require a good knowledge of cryogenics and vacuum handling systems. Constant supervision is needed for the maintenance of stable conditions for data-taking.

## A.1 Working principle

The operational temperature of bolometers is around 10-20 mK. With such low temperatures, the cooling system has to be completely shielded from the heat flow from the room-temperature stage. The inner parts of cryostat are maintained in vacuum and several copper screens are implemented to shield the sample from the black-body radiation. Each screen is thermalized at an appropriate temperature according to the cooling stages. Cooling down of the experimental volume is performed in several complex steps.

The first stage is a pre-cooling transition from the room temperature to the temperature of liquid helium: 4.2 K. This temperature is required to prevent heat inflow from outside and to cool the mixture of $^3$He and $^4$He (which is used for cooling down to base temperature and described further) before the flux enters the inner part of the cryostat.

There are two main types of cryostats, depending on the way to perform the pre-cooling: in "wet" cryostats the cryo-liquids are used to cool down to 4.2 K. In such set-ups the dilution refrigerator is placed inside a LHe bath. In some cases, at first the cryostat is cooled down with the liquid nitrogen bath to 77 K to decrease the helium consumption. An advantage of "wet" cryostats is the smaller noise on the detectors, but frequent helium refills are required. Usually during the refill data-taking cannot be performed due to unstable temperature conditions.

In another kind of dilution refrigerators, the pre-cooling is performed with a pulse tube. As there are no consumable cryogenic liquids required, this type is called "dry" cryostats. The pre-cooling is performed with four steps cycle. At first the helium gas is compressed in the pulse tube. As this gas has higher temperature and pressure, than on average, it flows to the warm end of the pulse tube and exchange

heat. Then the gas is expanded adiabatically in the pulse tube. This low-pressure cold gas is forced towards the cold end inside the cryostat and it picks up the heat there. The flow stops when the pressure in the tube is recovered to average. This cycle repeats, insulating the cold and hot temperature exchanges at two ends. Such cryostats can operate in stable conditions without interruptions for a long time, but they have high requirements for energy supply. The vibrations, induced by the pulse tube operation, can affect the operation of detectors in terms of noise. Another important advantage of pulse tube cryostats is the cost: for "dry" cryostat only electricity is required, while for "wet" cryostat a big amount of liquid helium is needed, and it is quite expensive. Maintenance of such cryostat needs constant attention to evaporation rate, and schedule of He refills.

To go below the LHe temperature (temperature of helium condensation at atmospheric pressure, 4.2 K) a mixture of two isotopes of helium is used ($^3$He and $^4$He) which provides the cooling power.

The cooling down to sub-Kelvin temperatures is based on the specific properties of this mixture. If the total $^3$He concentration is larger than 6.5%, and the mixture is cooled below the tri-critical point at 870 mK, the mixture separates into two phases. The lighter "concentrated phase" is rich in $^3$He, and the heavier "diluted phase" is rich in $^4$He (see Fig. A.1). The concentration of $^3$He in each phase depends on temperature. Since the enthalpy of $^3$He in the two phases is different, the "evaporation" of $^3$He from the concentrated phase to the diluted one may provide highly efficient cooling. $^4$He, composing the bulk of the diluted phase, is inert and non-interacting, and it may be neglected. The

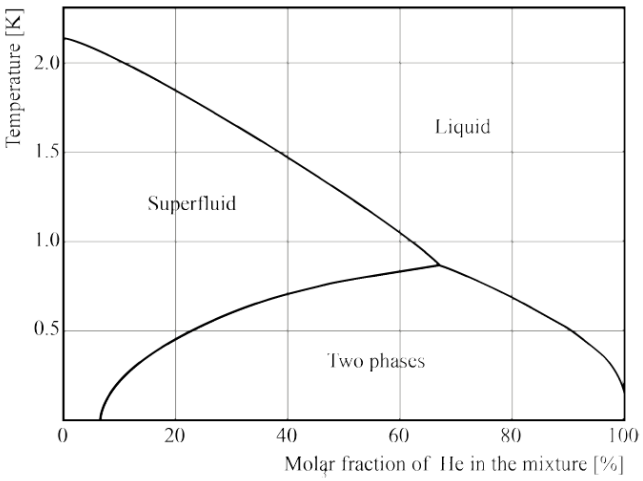


FIGURE A.1: The phase diagram of the $^3$He-$^4$He mixture and the critical point

above mentioned "evaporation" of $^3$He from the concentrated phase to the dilute phase cools the mixing chamber. Thanks to the different quantum properties of the two isotopes, this process works even at the

lowest temperatures because the equilibrium concentration of $^3$He in the diluted phase is finite, even at zero temperature. To reach the critical point, the mixture, which is injected starting from room temperature, is thermalized at the first cooling stage, then it passes through an impedance flux, providing a free adiabatic expansion in vacuum and cooling down the mixture through the Joule-Thomson effect. Sometimes a small bath of pumped LHe is present inside the IVC and is used to thermalize the mixture at T 1.2 K (so-called 1K pot). Neither the Joule-Thomson effect nor the 1K pot cools the mixture sufficiently to form the boundary phase. A separation phase occurs when temperatures fall below the tri-critical point. This cooling is provided by the still; the incoming mixture is cooled by the still before it enters to the mixing chamber and heat exchangers.

During the operations, $^3$He must be extracted from the diluted phase (to prevent saturation) and re-supplied to the concentrated phase. $^3$He is pumped away from the surface of the liquid in the still, where at 0.6 K 3He preferentially evaporates. The $^3$He exiting from the mixing chambers is used to cool down the incoming mixture with heat exchangers between the inlet and outlet lines. The dilution refrigera-

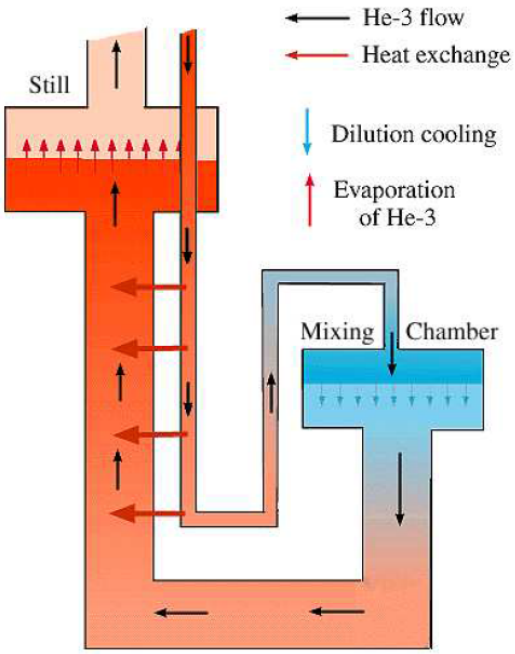


FIGURE A.2: The scheme of He mixture circulation during the cryostat operation.

tors design consists of a two-part external gas handling system. One part (the circulation system) is dedicated to the circulation and handling of the mixture, and the other (the auxiliary system) to auxiliary pumping operations. In general, every time the refrigerator is cooled

down, a hermetic vacuum seal at cryogenic temperatures needs to be made, and a low temperature vacuum feed-through must be used for the experimental wiring. Finally, samples are mechanically and thermally attached to the mixing chamber, as it is the coldest point inside the cryostat.

## A.2 Ulysse

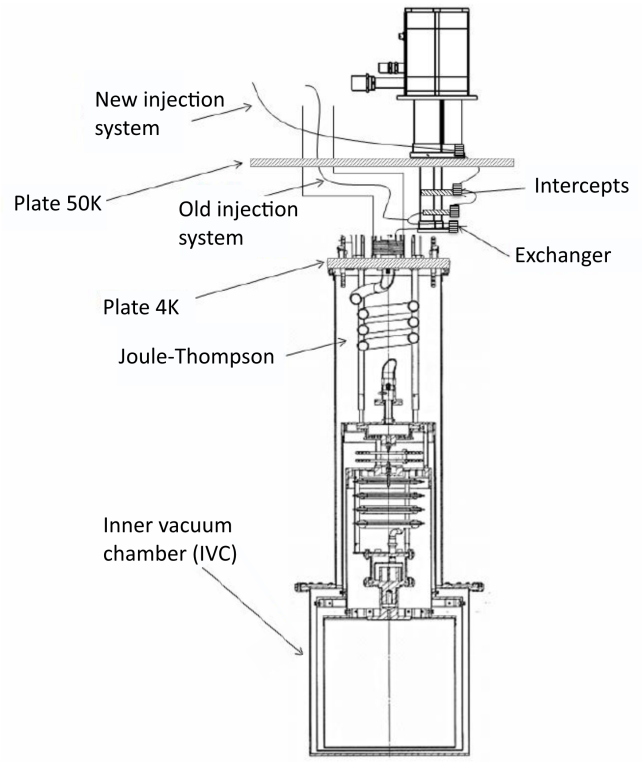


FIGURE A.3: Schematic drawing of the pulse tube cryostat "Ulysse".

This Dilution Refrigerator located at the CSNSM is a classical dilution unit with sintered silver heat exchangers and a large pumping system (40 $m^3$/h rotary pump and 400 l/s turbopump in He) [126]. It can achieve reasonably high $^3$He flow rates, thus providing the cooling power needed by massive detectors. The pre-cooling is performed with a pulse-tube refrigerator, consisting of the commercial unit PT-405 manufactured by Cryomech [127]. This model can achieve a cooling power of 25 W at 55 K at its first stage, and 0.3 W at 3.5 K at its second stage. As the pulse-tube provides periodical vibrations during the running and macro-bolometers are particularly sensitive detectors, their operation requires particular attention to vibrations reduction. At the mixing chamber stage, a mechanical decoupling system is placed to reduce the vibration transmission to the detector. It is based on four

stainless steel springs which provide a cut-off frequency of 3 Hz with a 2 kg load. Modules of copper disks can be placed in order to tune the weight of the detector assembly. The vacuum chambers of the cryostat are installed on the special pneumatic decoupling system, which also allows to reduce vibrations and improve the temperature stability [128]. The original PT-DR1 design [129] was slightly changed by reducing the number of the sintered silver heat exchangers from four to two, without affecting the base temperature. In order to benefit from the cooling power available at the level of the regenerator, two copper heat exchangers were installed on the stainless steel tube connecting the two main stages of the pulse-tube cryocooler, aiming at improving the effectiveness of the mixture condensation process. The result of this modification was spectacular: the mixture condensation time was reduced from 20 to only 3 h. An interesting feature of the PT-DR1 is that it is well optimized from the thermodynamical point of view. This allows to stop the $^3$He compressor, a major source of vibrations, during the normal operation, keeping a low injection pressure (of the order of 0.5 bar at a circulation rate of 130 $\mu$mol/s). The experimental volume

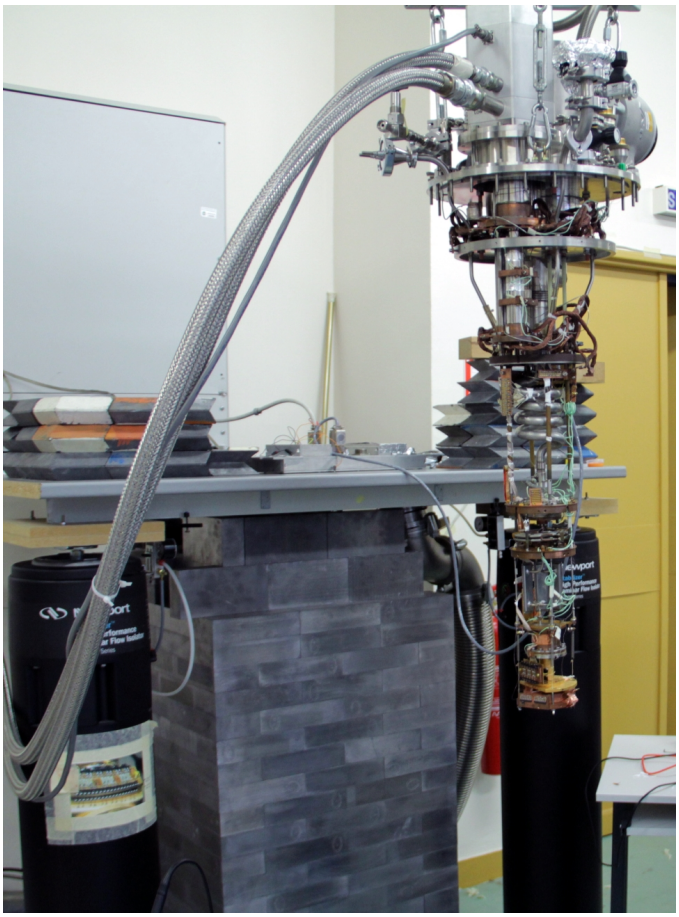

FIGURE A.4: Photo of the opened pulse tube cryostat "Ulysse" in front of the damping system and the outer vacuum chamber, shielded with lead bricks.

available in the cryostat for the bolometers corresponds to a cylindrical space with a diameter of 30 cm and a height of 20 cm. This allows to host easily several bolometers for the measurements. The cryostat can host 18 channels, 12 are on two jaeger connectors and 6 are on fisher. As the signals from scintillating bolometers, equipped with NTD, are relatively slow, an issue of high rate of signal pileup arises due to the environmental radioactivity. In order to reduce the rate, a shield of low-activity lead (less than 30 Bq/kg in $^{210}$Pb content) was built around the cryostat, with a minimum thickness of 10 cm.

The temperature at the floating plate can be stabilized to a fixed value by use of a PID controller, which delivers power to a heater in order to compensate the temperature fluctuations. For calibrations a thoriated tungsten wire is used, and characteristic $\gamma$ energies from environmental radioactivity.

## A.3 EDELWEISS experimental set-up

The EDELWEISS-III (Experience pour DEtecter Les Wimps En Site Souterrain) cryostat is located in the Laboratiore Souterrain de Modane (LSM), France. The laboratory is located under the Frejus mountain and it is one of the deepest underground laboratories: the rock overburden is 1700 m (4800 m water equivalent), and the muon flux is reduced up to 5 muons/m$^2$/day [130]. The cryostat was designed and produced

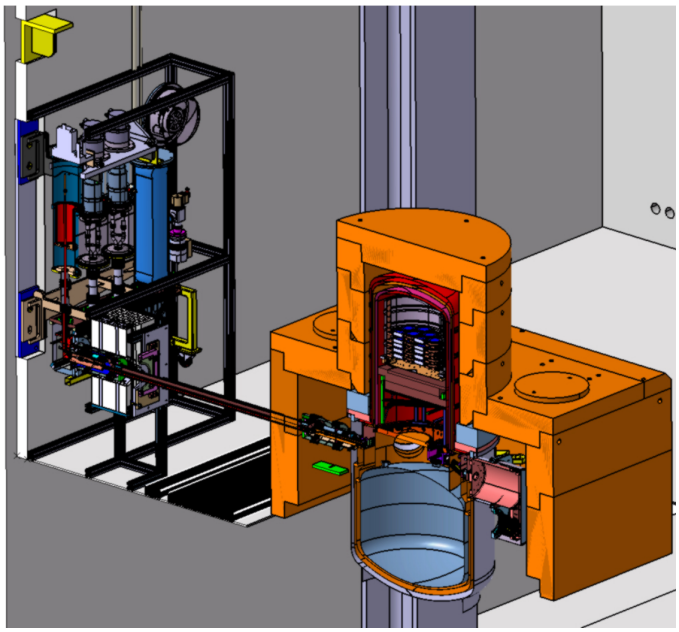

FIGURE A.5: Cross-section of the EDELWEISS-III reversed cryostat and the three thermal machines. Only a part of the lead shield is shown (orange) and the He dewar is the blue structure at the bottom [97]

.

by the Institut Neel, Grenoble. It is a custom dilution refrigerator with a reversed geometry: in most cases the structure is hanging down and the detectors are attached to the lowest part of the cryostat. Here the experimental volume is placed above the mixing chamber, 1 K pot and all cryogenic line. Fig. A.5 shows the cross-section of the cryostat structure. The pumps and compressors are placed outside the shields and equipped with mechanical decoupling elements. The experimental chamber is placed on a pneumatic damping system, which allows to reject the low-frequency noise (<1 Hz). The damping level can be adjusted remotely.

The detector chamber consists of four copper plates to hold the bolometers. 48 bolometers of proper size can be measured at the same time. During the measurements, the experimental volume is protected by 5 copper shields, each is thermalized at a certain temperature: room T, 100 K, 50 K, 1 K and 10 mK.

The EDELWEISS set-up is "wet" cryostat, requiring the use of liquid helium. The consumption of cryoliquid is minimized by the use of a cold vapor reliquefaction system, based on a Gifford Mac-Mahon machine. The approximate time, needed to reach the base temperature (20 mK) is approximately two weeks, while the helium refill is required once per week.

For passive shielding, lead (20 cm thickness) and polyethylene (50 cm thickness) shields are installed. The most inner shield part consists of from 2 cm thickness Roman lead with an activity of $^{210}$Pb<120 mBq/kg. An active muon veto is surrounding the whole cryostat for an effective muon rejection. The veto is represented by 46 individual plastic scintillator modules with the total surface of 100 m$^2$.

Another important part of background reduction is the control of $^{222}$Rn presence. It is controlled in the whole laboratory by the ventilation system with 10-15 Bq/m$^3$. In addition in the EDELWEISS clean room there is the possibility to flush deradonised air (30 mBq/kg) in the area of experimental volume (when the cryostat is open for operations with the detectors). The EDELWEISS set-up passed several upgrades during its operation over 10 years.

## A.4 Hall-C cryostat

The Hall-C cryostat is located in the Laboratori Nazionali del Gran Sasso (LNGS), Italy. It is an OXFORD TL200 cryostat with copper dewar and was commissioned in the early 90's. The Gran Sasso underground laboratory consists of three experimental Halls, named A, B and C. They are about 80 m distant from each other and, in principle, could feature slightly different rock coverage. The test cryostat is located in the hall C. The dilution refrigerator consists of a wet cryostat equipped with a high power dilution unit with an experimental space capable to host a CUORE mini-tower of 12 bolometers of 5x5x5 cm$^3$ each. A

reliquiefier system based on GM machines and a Joule-Tompson circuit provides a cold head directly in the main helium bath, stabilizing the liquid He level during the normal operation. The setup is shielded with two layers of lead shield with a minimal thickness of 10 cm each. The outer layer is made of common low radioactivity lead, while the inner layer is made of copper. The refrigerator thermal screens made by electrolytic copper provide an additional shield with a minimum thickness of 2 cm. An external 10 cm layer of borated polyethylene was installed to reduce the background due to environmental neutrons. The experimental space is shielded against the intrinsic radioactive contamination of the cryostat materials by a thick layer of 10 cm of Roman lead ($^{210}$Pb activity <4 mBq/kg), located inside the cryostat immediately below the MC. The refrigerator is surrounded by a Plexiglas antiradon box flushed with clean $N_2$ and is also enclosed in a Faraday cage to protect the electronics from the influence of external electromagnetic fields. Calibrations are performed using two wires of thoriated tungsten inserted inside the external lead shield in immediate contact with the outer vacuum chamber (OVC) of the dilution refrigerator. Data are acquired with a CUORE-like DC electronics. For some channels a cold pre-amplifier at 4 K is provided.

## A.5 CUPID-0 cryostat

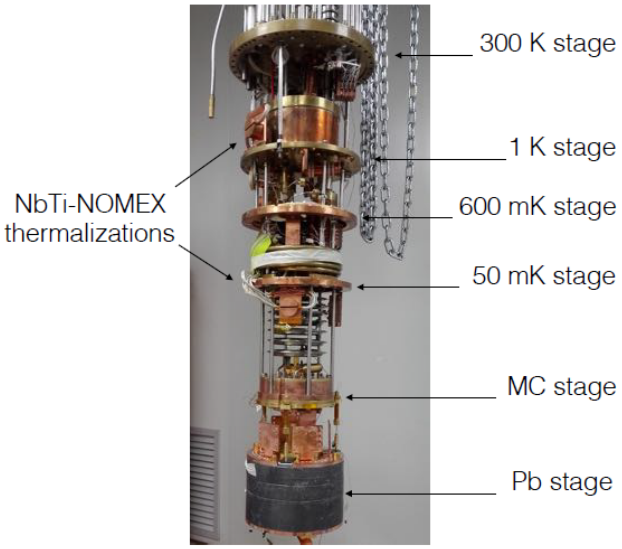


FIGURE A.6: Opened CUPID-0 cryostat.

The cryostat, located in Hall A in LNGS and currently used for CUPID-0 demonstrator, was commissioned in 1988 and it is an Oxford TL1000 with copper He dewar. This set-up was also used to host Cuoricino [71] and CUORE-0 [72] detectors. This is a "wet" cryostat

and periodical LHe refills are required. The dilution unit has 1 mW cooling power at 100 mK.

The cryostat has a thick Roman lead shield just below the mixing chamber. The detectors are coupled to the cryostat with a spring for vibrations reduction. Several upgrades were performed on the set-up during the exploitation. One of them is the increase of read-out channels: starting with 52 channels, now it is possible to measure 136 channels simultaneously. A mechanical decoupling system was installed for vibrations reduction. The inner copper shield surface was etched with citric acid before the measurements of the CUPID-0 demonstrator (described in Chapter 6) to reduce possible contamination inside the cryostat.

# Bibliography


[1] E. Fermi, "Tentativo di una teoria dei raggi $\beta$", *La Ricerca Scientifica*, vol. 2, 1933. DOI: 10.1007/BF02959820.

[2] E. Majorana, "Teoria simmetrica dell'elettrone e del positrone", *Il Nuovo Cimento (1924-1942)*, vol. 14, no. 4, p. 171, 1937. DOI: 10.1007/BF02961314.

[3] H. Bethe and R. Peierls, "The Neutrino", *Nature*, vol. 133:532, 1934. DOI: 10.1038/133532a0.

[4] B. Pontecorvo, "Report pd-205", *Chalk River Laboratory*, 1946.

[5] F. Reines and C. L. Cowan, "The Neutrino", *Nature*, vol. 178, no. 1, pp. 446–449, 1956. DOI: 10.1038/178446a0.

[6] L. D. Landau, "On the conservation laws for weak interactions", *Nucl. Phys*, vol. 3, 1957. DOI: 10.1016/0029-5582(57)90061-5.

[7] T. D. Lee and C. N. Yang, "Parity nonconservation and a two-component theory of the neutrino", *Phys. Rev.*, vol. 105, 1957. DOI: 10.1103/PhysRev.105.1671.

[8] A. Salam, "On parity conservation and neutrino mass", *Il Nuovo Cimento*, vol. 5, 1957. DOI: 10.1007/BF0281284.

[9] B. Pontecorvo, "Mesonium and antimesonium", *J. Exp. Theor. Phys*, vol. 6, 1957.

[10] M. Goldhaber, L. Grodzins, and A. W. Sunyar, "Helicity of Neutrinos", *Phys. Rev.*, vol. 109, pp. 1015–1017, 1958. DOI: 10.1103/PhysRev.109.1015.

[11] G. Danby et al., "Observation of High-Energy Neutrino Reactions and the Existence of Two Kinds of Neutrinos", *Phys. Rev. Lett.*, vol. 9, pp. 36–44, 1962. DOI: 10.1103/PhysRevLett.9.36.

[12] R. Davis, D. S. Harmer, and K. C. Hoffman, "Search for Neutrinos from the Sun", *Phys. Rev. Lett.*, vol. 20, pp. 1205–1209, 1968. DOI: 10.1103/PhysRevLett.20.1205.

[13] F. Hasert et. al, "Observation of neutrino-like interactions without muon or electron in the Gargamelle neutrino experiment", *Nucl. Phys. B*, vol. 73, no. 1, pp. 1 –22, 1974. DOI: 10.1016/0550-3213(74)90038-8.

[14] K. S. Hirata et al., "Experimental study of the atmospheric neutrino flux", *Phys. Lett. B*, vol. 205, pp. 416–420, 1988.

[15] P. Anselmannet. al., "Solar neutrinos observed by GALLEX at Gran Sasso.", *Phys. Lett.*, vol. B285, pp. 376–389, 1992.

[16] J. N. Abdurashitov et. al., "Results from SAGE the Russian-American gallium solar neutrino experiment", *Phys. Lett. B*, vol. 328, no. 1, pp. 234 –248, 1994. DOI: 10.1016/0370-2693(94)90454-5.

[17] Y. Fukuda et al., "Measurements of the Solar Neutrino Flux from Super-Kamiokande's First 300 Days", *Phys. Rev. Lett.*, vol. 81, pp. 1158–1162, 1998. DOI: 10.1103/PhysRevLett.81.1158.

[18] K. Kodama et. al, "Observation of tau neutrino interactions", *Phys. Lett.*, vol. B504, pp. 218–224, 2001. DOI: 10.1016/S0370-2693(01)00307-0.

[19] Q. R. Ahmad et. al., "Direct Evidence for Neutrino Flavor Transformation from Neutral-Current Interactions in the Sudbury Neutrino Observatory", *Phys. Rev. Lett.*, vol. 89, p. 011 301, 2002. DOI: 10.1103/PhysRevLett.89.011301.

[20] M. H. Ahn et. al., "Measurement of neutrino oscillation by the K2K experiment", *Phys. Rev. D*, vol. 74, p. 072 003, 2006. DOI: 10.1103/PhysRevD.74.072003.

[21] K. Eguchi et. al, "First results from kamLAND: Evidence for Reactor Antineutrino Disappearance", *Phys. Rev. Lett.*, vol. 90, p. 021 802, 2003. DOI: 10.1103/PhysRevLett.90.021802.

[22] F. P An et. al, "Observation of Electron-Antineutrino Disappearance at Daya Bay", *Phys. Rev. Lett.*, vol. 108, p. 171 803, 2012. DOI: 10.1103/PhysRevLett.108.171803.

[23] D. Akimov et. al, "Observation of coherent elastic neutrino-nucleus scattering", *Science*, vol. 357, no. 6356, pp. 1123–1126, 2017. DOI: 10.1126/science.aao0990.

[24] *Wikipedia*. [Online]. Available: https://en.wikipedia.org/wiki/Standard_Model.

[25] P. F. de Salas, D. V. Forero, C. A. Ternes, M. Tortola, and J. W. F. Valle, "Status of neutrino oscillations 2017", 2017. arXiv: 1708.01186 [hep-ph].

[26] G. Bellini et al., "Final results of Borexino Phase-I on low-energy solar neutrino spectroscopy", *Phys. Rev. D*, vol. 89, p. 112 007, 2014. DOI: 10.1103/PhysRevD.89.112007.

[27] B. Aharmim et. al., "Combined analysis of all three phases of solar neutrino data from the Sudbury Neutrino Observatory", *Phys. Rev. C*, vol. 88, p. 025 501, 2013. DOI: 10.1103/PhysRevC.88.025501.

[28] M. G. Aartsen et. al., "Measurement of Atmospheric Neutrino Oscillations at 6-56 Gev with IceCube DeepCore", *Phys. Rev. Lett.*, vol. 120, p. 071 801, 2018. DOI: 10.1103/PhysRevLett.120.071801.

[29] K. Abe et. al, "Atmospheric neutrino oscillation analysis with external constraints in Super-Kamiokande I-IV", *Phys. Rev. D*, vol. 97, p. 072 001, 2018. DOI: 10.1103/PhysRevD.97.072001.

[30] S. F. King, "Neutrino mass and mixing in the seesaw playground", *Nucl. Phys. B*, vol. 908, pp. 456 –466, 2016. DOI: 10.1016/j.nuclphysb.2015.12.015.

[31] S. Dell'Oro, S. Marcocci, and F. Vissani, "New expectations and uncertainties on neutrinoless double beta decay", *Phys. Rev. D*, vol. 90, p. 033 005, 2014. DOI: 10.1103/PhysRevD.90.033005.

[32] G. Benato, "Effective Majorana mass and neutrinoless double beta decay", *Eur. Phys. J C*, vol. 75, no. 11, 2015. DOI: 10.1140/epjc/s10052-015-3802-1.

[33] M. A. Acero et. al., "New constraints on oscillation parameters from $\nu_e$ appearance and $\nu_\mu$ disappearance in the NOvA experiment", *Phys. Rev. D*, vol. 98, p. 032 012, 2018. DOI: 10.1103/PhysRevD.98.032012.

[34] M. Ghosh, S. Goswami, and S. K. Raut, "Implications of $\delta$CP = -90$^o$ towards determining hierarchy and octant at T2K and T2K-II", *Mod. Phys. Lett. A*, vol. 32, no. 06, p. 1 750 034, 2017. DOI: 10.1142/S0217732317500341.

[35] M. Agostini, G. Benato, and J. A. Detwiler, "Discovery probability of next-generation neutrinoless double-$\beta$ decay experiments", *Phys. Rev. D*, vol. 96, p. 053 001, 2017. DOI: 10.1103/PhysRevD.96.053001.

[36] F. Simpson, R. Jimenez, C. Pena-Garay, and L. Verde, "Strong bayesian evidence for the normal neutrino hierarchy", *J. Cosmol. Astropart. Phys.*, vol. 2017, no. 06, p. 029, 2017.

[37] D. Borah and M. K. Das, "Neutrino masses and leptogenesis in type I and type II seesaw models", *Phys. Rev. D*, vol. 90, p. 015 006, 2014. DOI: 10.1103/PhysRevD.90.015006.

[38] C. Kraus et al., "Final results from phase II of the Mainz neutrino mass searching tritium $\beta$ decay", *Eur. Phys. J C*, vol. 40, no. 4, pp. 447–468, 2005. DOI: 10.1140/epjc/s2005-02139-7.

[39] V. M. Lobashev et al., "Direct search for neutrino mass and anomaly in the tritium beta-spectrum: Status of Troitsk neutrino mass experiment", *Nucl. Phys. B - Proc. Sup.*, vol. 91, no. 1, pp. 280 –286, 2001. DOI: 10.1016/S0920-5632(00)00952-X.

[40] L. Bornschein et. al, "Status of the Karlsruhe Tritium Neutrino Mass Experiment KATRIN", *Fusion Science and Technology*, vol. 71, no. 4, pp. 485–490, 2017. DOI: 10.1080/15361055.2017.1291241.

[41] M Sisti et al., "New limits from the milano neutrino mass experiment with thermal microcalorimeters", *Nucl. Instrum. Methods Phys. Res A*, vol. 520, no. 1, pp. 125 –131, 2004. DOI: 10.1016/j.nima.2003.11.273.

[42] V. A. Zheltonozhsky, A. M. Savrasov, N. V. Strilchuk, and V. I. Tretyak, "Precise measurement of energy of the first excited state of $^{115}$Sn ($e_{exc}$ = 497.3 kev)", *EPL (Europhysics Letters)*, vol. 121, no. 1, p. 12 001, 2018. [Online]. Available: http://stacks.iop.org/0295-5075/121/i=1/a=12001.

[43] E. Andreotti, M. Hult, R. Gonzalez de Orduna, G. Marissens, J. S. E. Wieslander, and M. Misiaszek, "Half-life of the $\beta$ decay $^{115}In(9/2^+) \rightarrow^{115} Sn(3/2^+)$", *Phys. Rev. C*, vol. 84, p. 044 605, 4 2011. DOI: 10.1103/PhysRevC.84.044605.

[44] B. Alpert et. al., "HOLMES: The electron capture decay of $^{163}$Ho to measure the electron neutrino mass with sub-eV sensitivity", *Eur. Phys. J C*, vol. 75, no. 3, p. 112, 2015. DOI: 10.1140/epjc/s10052-015-3329-5.

[45] P. A. R. Ade et. al., "Planck 2015 results - XIII. Cosmological parameters", *A&A*, vol. 594, 2016. DOI: 10.1051/0004-6361/201525830.

[46] A. J. Cuesta, V. Niro, and L. Verde, "Neutrino mass limits: Robust information from the power spectrum of galaxy surveys", *Physics of the Dark Universe*, vol. 13, pp. 77 –86, 2016. DOI: 10.1016/j.dark.2016.04.005.

[47] M. Goeppert-Mayer, "Double beta-disintegration", *Phys. Rev.*, vol. 48, no. 1, pp. 512–516, 1935. DOI: 10.1103/PhysRev.48.512.

[48] Z. G. Berezhiani, A. Y. Smirnov, and J. W. F. Valle, "Observable majoron emission in neutrinoless double beta decay", *Phys. Lett. B*, vol. 291, no. 1, pp. 99 –105, 1992. DOI: 10.1016/0370-2693(92)90126-O.

[49] W. H. Furry, "On Transition Probabilities in Double Beta Desintegration", *Phys. Rev.*, vol. 56, pp. 1184–1193, 1939. DOI: 10.1103/PhysRev.56.1184.

[50] J. J. Gomez-Cadenas and J. Martin-Albo Simon, "Theory and phenomenology of neutrinoless double beta decay", p. 004, Jul. 2015. arXiv: 1502.00581v2.

[51] C. Patrignani and P. D. Group, "Review of Particle Physics", *Chin. Phys. C*, vol. 40, no. 10, p. 100 001, 2016.

[52] J. Suhonen and O. Civitarese, "Probing the quenching of $g_A$ by single and double beta decays", *Phys. Lett. B*, vol. 725, no. 1, pp. 153 –157, 2013. DOI: 10.1016/j.physletb.2013.06.042.

[53] J. Engel and J. Menendez, "Status and future of nuclear matrix elements for neutrinoless double-beta decay: A review", *Reports on Progress in Physics*, vol. 80, no. 4, p. 046 301, 2017.

[54] M. Mihai, T. Pahomi, and S. Stoica, "Values of the phase space factors involved in double beta decay", vol. 67, pp. 872–889, Sep. 2015.

[55] J. M. Yao, L. S. Song, K. Hagino, P. Ring, and J. Meng, "Systematic study of nuclear matrix elements in neutrinoless double-$\beta$ decay with a beyond-mean-field covariant density functional theory", *Phys. Rev. C*, vol. 91, p. 024 316, 2015. DOI: 10.1103/PhysRevC.91.024316.

[56] G. J. Feldman and R. D. Cousins, "Unified approach to the classical statistical analysis of small signals", *Phys. Rev. D*, vol. 57, pp. 3873–3889, 1998. DOI: 10.1103/PhysRevD.57.3873.

[57] D.-M. Mei and A. Hime, "Muon-induced background study for underground laboratories", *Phys. Rev. D*, vol. 73, p. 053 004, 2006. DOI: 10.1103/PhysRevD.73.053004.

[58] S. Cebrian, "Cosmogenic activation of materials", *Int. J. Mod. Phys. A*, vol. 32, no. 30, p. 1 743 006, 2017. DOI: 10.1142/S0217751X17430060.

[59] D. M. Chernyak, F. A. Danevich, A. Giuliani, E. Olivieri, M. Tenconi, and V. I. Tretyak, "Random coincidence of $2\nu2\beta$ decay events as a background source in bolometric $0\nu2\beta$ decay experiments", *Eur. Phys. J. C*, vol. 72, no. 4, 2012. DOI: 10.1140/epjc/s10052-012-1989-y.

[60] M. Hirsch, "Phenomenology of neutrinoless double beta decay", *Nucl. Phys. B - Proc. Sup.*, vol. 221, pp. 119 –124, 2011. DOI: 10.1016/j.nuclphysbps.2011.03.105.

[61] J. J. Gomez-Cadenas et al., "Sense and sensitivity of double beta decay experiments", *J. Cosmol. Astropart. Phys*, vol. 2011, no. 06, p. 007, 2011. DOI: 10.1088/1475-7516/2011/06/007.

[62] A. S. Barabash and V. B. Brudanin, "Investigation of double-beta decay with the NEMO-3 detector", *Physics of Atomic Nuclei*, vol. 74, no. 2, pp. 312–317, 2011. DOI: 10.1134/S1063778811020062.

[63] M. Agostini et. al., "GERDA results and the future perspectives for the neutrinoless double beta decay search using $^{76}$Ge", *Int. J. Mod. Phys. A*, vol. 33, no. 09, p. 1 843 004, 2018. DOI: 10.1142/S0217751X18430042.

[64] O. Azzolini et. al, "First Result on the Neutrinoless Double Beta Decay of $^{82}$se with CUPID-0", 2018. arXiv: 1802.07791 [nucl-ex].

[65] F. A. Danevich et al., "Search for double beta decay of $^{116}$Cd with enriched $^{116}$ $CdWo_4$ crystal scintillators (Aurora experiment)", *J. Phys. Conf. Ser.*, vol. 718, no. 6, p. 062 009, 2016.

[66] C. Alduino et. al, "First results from CUORE: A search for lepton number violation via $0\nu\beta\beta$ decay of $^{130}Te$", *Phys. Rev. Lett.*, vol. 120, p. 132 501, 2018. DOI: 10.1103/PhysRevLett.120.132501.

[67] A. Gando et al., "Search for Majorana Neutrinos Near the Inverted Mass Hierarchy Region with KamLAND-Zen", *Phys. Rev. Lett.*, vol. 117, p. 082 503, 2016. DOI: 10.1103/PhysRevLett.117.082503.

[68] S. Elliott et al., "Initial results from the Majorana Demonstrator", *J. Phys. Conf. Ser*, vol. 888, no. 1, p. 012 035, 2017.

[69] V. Guiseppe, *New Results from the MAJORANA DEMONSTRATOR Experiment*, 2018. DOI: 10.5281/zenodo.1286900.

[70] J. B. Albert et al., "Search for Neutrinoless Double-Beta Decay with the Upgraded EXO-200 detector", *Phys. Rev. Lett.*, vol. 120, p. 072 701, 2018. DOI: 10.1103/PhysRevLett.120.072701.

[71] E Andreotti et. al., "$^{130}$Te neutrinoless double-beta decay with CUORICINO", *Astropart. Phys.*, vol. 34, no. 11, pp. 822 –831, 2011. DOI: 10.1016/j.astropartphys.2011.02.002.

[72] K. Alfonso et. al., "Search for Neutrinoless Double-Beta Decay of $^{130}$Te with CUORE-0", *Phys. Rev. Lett.*, vol. 115, p. 102 502, 2015. DOI: 10.1103/PhysRevLett.115.102502.

[73] S. Andringa and S. Collaboration, "SNO+ status and plans for double beta decay search and other neutrino studies", *J. Phys. Conf. Ser.*, vol. 665, no. 1, p. 012 080, 2016.

[74] G. Orebi Gann, *SNO+*, 2018. DOI: 10.5281/zenodo.1286908.

[75] R. Arnold et. al, "Search for neutrinoless double-beta decay of $^{100}Mo$ with the NEMO-3 detector", *Phys. Rev. D*, vol. 89, p. 111 101, 2014. DOI: 10.1103/PhysRevD.89.111101.

[76] G. Wang et al., "CUPID: CUORE (Cryogenic Underground Observatory for Rare Events) Upgrade with Particle IDentification", 2015. arXiv: 1504.03599 [physics.ins-det].

[77] G. Wang *et al.*, "R&D towards CUPID (CUORE Upgrade with Particle IDentification)", 2015. arXiv: 1504.03612 [physics.ins-det].

[78] A. Giuliani, F. A. Danevich, and V. I. Tretyak, "A multi-isotope $0\nu2\beta$ bolometric experiment", *Eur. Phys. J. C*, vol. 78, no. 3, p. 272, 2018. DOI: 10.1140/epjc/s10052-018-5750-z.

[79] N. Abgrall et. al, "The large enriched germanium experiment for neutrinoless double beta decay (LEGEND)", *AIP Conference Proceedings*, vol. 1894, no. 1, p. 020 027, 2017. DOI: 10.1063/1.5007652.

[80] J. B. Albert et. al., "Sensitivity and discovery potential of nEXO to Neutrinoless Double Beta Decay", 2017. arXiv: 1710.05075 [nucl-ex].

[81] C. Patrick and F. Xie, "Status of the superNEMO $0\nu\beta\beta$ experiment", in *Proceedings, Prospects in Neutrino Physics (NuPhys2016):London, UK, December 12-14, 2016*, 2017. arXiv: 1704.06670 [physics.ins-det].

[82] N. Wang, F. C. Wellstood, B. Sadoulet, E. E. Haller, and J. Beeman, "Electrical and thermal properties of neutron-transmutation-doped Ge at 20 mK", *Phys. Rev. B*, vol. 41, pp. 3761–3768, 1990. DOI: 10.1103/PhysRevB.41.3761.

[83] A Aliane et. al., "Design and fabrication process of silicon microcalorimeters on simple SOI technology for X-ray spectral imaging", *Nucl. Instrum. Methods Phys. Res. A*, vol. 594, no. 2, pp. 210 –214, 2008. DOI: https://doi.org/10.1016/j.nima.2008.06.029.

[84] D. Gray et. al, "The first tests of a large-area light detector equipped with metallic magnetic calorimeters for scintillating bolometers for the lumineu neutrinoless double beta decay search", *J. Low Temp. Phys.*, vol. 184, no. 3, pp. 904–909, 2016. DOI: 10.1007/s10909-016-1535-7.

[85] B. I. Shklovskii and A. L. Efros, *Electronic properties of doped semiconductors*. Springer Science & Business Media, 2013, vol. 45.

[86] J. Beeman et al., "A next-generation neutrinoless double beta decay experiment based on $ZnMoO_4$ scintillating bolometers", *Phys. Lett. B*, vol. 710, no. 2, pp. 318 –323, 2012. DOI: https://doi.org/10.1016/j.physletb.2012.03.009.

[87] J. B. Birks, "Scintillations from Organic Crystals: Specific Fluorescence and Relative Response to Different Radiations", *Proc. Phys. Soc. A*, vol. 64, no. 10, p. 874, 1951.

[88] V. I. Tretyak, "Semi-empirical calculation of quenching factors for ions in scintillators", *Astropart. Phys.*, vol. 33, no. 1, pp. 40 –53, 2010. DOI: 10.1016/j.astropartphys.2009.11.002.

[89] L. Bergé et al., "Complete event-by-event $\alpha/\gamma(\beta)$ separation in a full-size $TeO_2$ CUORE bolometer by neganov-luke-magnified light detection", *Phys. Rev. C*, vol. 97, p. 032 501, 2018. DOI: 10.1103/PhysRevC.97.032501.

[90] M. Mancuso, "Development and optimization of scintillating bolometers and innovative light detectors for a pilot underground experiment on neutrinoless double beta decay", Theses, Université Paris-Saclay, 2016.

[91] A Alessandrello et al., "A programmable front-end system for arrays of bolometers", *Nucl. Instrum. Methods Phys. Res. A*, vol. 444, no. 1, pp. 111 –114, 2000. DOI: 10.1016/S0168-9002(99)01340-6.

[92] D. McCammon, "Thermal equilibrium calorimeters – an introduction", in *Cryogenic Particle Detection*. Berlin, Heidelberg: Springer Berlin Heidelberg, 2005, pp. 1–34. DOI: 10.1007/10933596_1.

[93] E. Gatti and P. F. Manfredi, "Processing the signals from solid-state detectors in elementary-particle physics", *La Rivista del Nuovo Cimento*, vol. 9, no. 1, pp. 1–146, 1986. DOI: 10.1007/BF02822156.

[94] R Arnold et. al, "Measurement of double beta decay of $^{100}$Mo to excited states in the NEMO-3 experiment", *Nuclear Physics A*, vol. 781, Jan. 2007.

[95] L. Bergé et al., "Purification of molybdenum, growth and characterization of medium volume $ZnMoO_4$ crystals for the LUMINEU program", *JINST*, vol. 9, 2014. DOI: 10.1088/1748-0221/9/06/P06004.

[96] S. Pirro et al., "Vibrational and thermal noise reduction for cryogenic detectors", *Nucl. Instr. Meth. Phys. Res. A*, vol. 444, no. 1, pp. 331 –335, 2000. DOI: 10.1016/S0168-9002(99)01376-5.

[97] E. Armengaud et al., "Development of $^{100}$Mo-containing scintillating bolometers for a high-sensitivity neutrinoless double-beta decay search", *Eur. Phys. J C*, vol. 178, no. 1, pp. 446–449, 2017.

[98] A Alessandrello et. al., "Methods for response stabilization in bolometers for rare decays", *Nucl. Instrum. Methods Phys. Res. A*, vol. 412, no. 2, pp. 454 –464, 1998. DOI: 10.1016/S0168-9002(98)00458-6.

[99] M. Pedretti, "The single module for Cuoricino and CUORE detectors: Tests, construction and modelling", PhD Thesis, Università degli Studi dell'Insubria, 2004.

[100] [Online]. Available: http://www.huntsman.com/advanced_materials/a/Home.

[101] C. Alduino et. al, "CUORE-0 detector: Design, construction and operation", *J. Instrum.*, vol. 11, no. 07, P07009, 2011. DOI: 10.1088/1748-0221/11/07/P07009.

[102] E. Armengaud et al., "Performance of the EDELWEISS-III experiment for direct dark matter searches", *JINST*, vol. 1, 2017. DOI: 10:1706.01070.

[103] V. Kobychev, "Simulation of absolute efficiency of LMO and ZMO in edelweiss with K40 source", Presentation at Edelweiss Collaboration Meeting, Lyon 10-12 April 2017.

[104] A. S. Barabash et. al., "First test of an enriched $^{116}CdWO_4$ scintillating bolometer for neutrinoless double-beta-decay searches", *Eur. Phys. J. C*, vol. 76, no. 9, p. 487, 2016. DOI: 10.1140/epjc/s10052-016-4331-2.

[105] f. Poda D. V., "$^{100}$Mo-enriched $Li_2MoO_4$ scintillating bolometers for $0\nu2\beta$ decay search: From LUMINEU to CUPID-0/Mo projects", *AIP Conf. Proc.*, vol. 1894, p. 020 017, 2017. DOI: 10.1063/1.5007642.

[106] *Goodfellow*. [Online]. Available: www.goodfellow.com.

[107] C. Zhang, D. M. Mei, V. Kudryavtsev, and S. Fiorucci, "Cosmogenic activation of materials used in rare event search experiments", *Astropart. Phys.*, vol. 84, pp. 62 –69, 2016. DOI: 10.1016/j.astropartphys.2016.08.008.

[108] J. Ouellet, *Latest Results from the CUORE Experiment*, 2018. DOI: 10.5281/zenodo.1286904. [Online]. Available: https://doi.org/10.5281/zenodo.1286904.

[109] M.-A. Justo and J. Gomez Cadenas, *Python library for the calculation of the sensitivity of a neutrinoless double beta decay experiment*. [Online]. Available: https://github.com/jmalbos/pybbsens.

[110] J. W. Beeman et. al, "Double-beta decay investigation with highly pure enriched $^{82}$Se for the LUCIFER experiment", *Eur. Phys. J C*, vol. 75, no. 12, p. 591, 2015. DOI: 10.1140/epjc/s10052-015-3822-x.

[111] *Lucifer project*. [Online]. Available: https://web.infn.it/lucifer/.

[112] I. Dafinei et al., "Production of $^{82}$Se enriched Zinc Selenide (ZnSe) crystals for the study of neutrinoless double beta decay", *J. Cryst. Growth*, vol. 475, pp. 158 –170, 2017. DOI: 10.1016/j.jcrysgro.2017.06.013.

[113] D. R. Artusa et. al., "First array of enriched $Zn^{82}Se$ bolometers to search for double beta decay", *Eur. Phys. J C*, vol. 76, no. 7, p. 364, 2016. DOI: 10.1140/epjc/s10052-016-4223-5.

[114] J. W. Beeman et. al, "Current Status and Future Perspectives of the LUCIFER experiment", *Adv. High Energy Phys.*, vol. 2013, no. 237973, p. 15, 2013. DOI: 10.1155/2013/237973.

[115] C. Arnaboldi et. al., "Production of high purity $TeO_2$ single crystals for the study of neutrinoless double beta decay", *J. Cryst. Growth*, vol. 312, no. 20, pp. 2999 –3000, 2010. DOI: https://doi.org/10.1016/j.jcrysgro.2010.06.034.

[116] G. Zuzel et al., "The Darkside Experiment: Present Status and Future", *J. Phys. Conf. Ser*, vol. 798, p. 012 109, 2017. DOI: 10.1088/1742-6596/798/1/012109.

[117] O. Azzolini et. al, "Analysis of cryogenic calorimeters with light and heat read-out for double beta decay searches", 2018. arXiv: 1806.02826 [nucl-ex].

[118] E. Haller, K. Itoh, and J. Beeman, "Neutron Transmutation Doped (NTD) germanium thermistors for sub-mm bolometer applications", vol. 388, Jan. 1997.

[119] X.-F. Navick et al., "NTD-Ge Production in the LUMINEU Experiment Using Cryogenic Detectors for Rare Event Searches and Other Applications", *J. Low Temp. Phys.*, 2018. DOI: 10.1007/s10909-018-2005-1.

[120] X.-F. Navick et al., "Development of NTD-Ge Cryogenic Sensors in LUMINEU", *J. Low Temp. Phys.*, vol. 184, no. 1, pp. 292–298, 2016. DOI: 10.1007/s10909-016-1572-2.

[121] *Trmc2*. [Online]. Available: http://www.neel.cnrs.fr/spip.php?article149&lang=en.

[122] T. B. Bekker et al., "Aboveground test of an advanced $Li_2MoO_4$ scintillating bolometer to search for neutrinoless double beta decay of $^{100}$Mo", *Astropart. Phys.*, vol. 72, pp. 38 –45, 2016. DOI: 10.1016/j.astropartphys.2015.06.002.

[123] D. Z. Freedman, "Coherent effects of a weak neutral current", *Phys. Rev. D*, vol. 9, pp. 1389–1392, 1974. DOI: 10.1103/PhysRevD.9.1389.

[124] J. Billard, J. Johnston, and B. J. Kavanagh, "Prospects for exploring New Physics in Coherent Elastic Neutrino-Nucleus Scattering", 2018. arXiv: 1805.01798.

[125] O. Barinova et al., "Solid solution $Li_2MoO_4$ – $Li_2WO_4$ crystal growth and characterization", *J. Cryst. Growth*, vol. 468, pp. 365 –368, 2017. DOI: 10.1016/j.jcrysgro.2016.10.009.

[126] M. Mancuso et al., "An Aboveground Pulse-Tube-Based Bolometric Test Facility for the Validation of the LUMINEU $ZnMoO_4$ Crystals", *J. Low Temp. Phys.*, vol. 176, no. 3, pp. 571–577, 2014. DOI: 10.1007/s10909-013-1044-x.

[127] *Cryomech*. [Online]. Available: http://www.cryomech.com/.

[128] *Newport*. [Online]. Available: https://www.newport.com.

[129] T. Prouvé, H. Godfrin, C. Gianese, S. Triqueneaux, and A. Ravex, "Pulse-Tube Dilution Refrigeration Below 10 mK", vol. 148, pp. 909–914, Sep. 2007.

[130] B. Schmidt et al., "Muon-induced background in the EDELWEISS dark matter search", *Astropart. Phys.*, vol. 44, pp. 28 – 39, 2013. DOI: https://doi.org/10.1016/j.astropartphys.2013.01.014.